



Title	Study of 5f Electronic States in Uranium Systems with CaBe <sub>2</sub> Ge <sub>2</sub> -Type Crystal Structure Lacking Local-Inversion Symmetry
Author(s)	今, 布咲子
Citation	北海道大学. 博士(理学) 甲第15739号
Issue Date	2024-03-25
DOI	10.14943/doctoral.k15739
Doc URL	<a href="http://hdl.handle.net/2115/92272">http://hdl.handle.net/2115/92272</a>
Type	theses (doctoral)
File Information	Fusako_Kon.pdf



[Instructions for use](#)

博士学位論文

Study of 5f Electronic States in Uranium Systems  
with  $\text{CaBe}_2\text{Ge}_2$ -Type Crystal Structure Lacking Local-Inversion Symmetry

(局所空間反転対称性の破れた  $\text{CaBe}_2\text{Ge}_2$  型構造を有する  
U 化合物における 5f 電子状態の研究)

今 布咲子

北海道大学大学院理学院  
物性物理学専攻

2024 年 3 月

HOKKAIDO UNIVERSITY

GRADUATED SCHOOL OF SCIENCE

DEPARTMENT OF CONDENSED-MATTER PHYSICS

---

Study of 5f Electronic States  
in Uranium Systems  
with  $\text{CaBe}_2\text{Ge}_2$ -Type Crystal Structure  
Lacking Local-Inversion Symmetry

---

*Author:*  
Fusako Kon

*Supervisor:*  
Dr. Hiroshi Amitsuka  
*Co-supervisors:*  
Dr. Tatsuya Yanagisawa  
Dr. Hiroyuki Yoshida  
Dr. Satoru Hayami

March, 2024



# Acknowledgement

This doctoral dissertation has been supported by many people. Firstly, I express my gratitude to Prof. Tatsuya Yanagisawa, Prof. Hiroyuki Yoshida, Assoc. Prof. Satoru Hayami, and Prof. Hiroshi Amitsuka (Hokkaido University), for helpful discussions and suggestions during the examination of this thesis.

The resonant X-ray scattering experiments in this study is largely owed to the cooperation of Assoc. Prof. Hironori Nakao (IMSS, KEK) and Dr. Chihiro Tabata (MSRC, JAEA). In the study of neutron scattering experiments, I received the generous supports from Assoc. Prof. Nakajima and Dr. Saito (ISSP, the University of Tokyo), from the experiments to the analyses. The crystal growth was supported by Prof. Dai Aoki and Dr. Yusei Shimizu (IMR, Tohoku University). Furthermore, the discussions with Assoc. Prof. Satoru Hayami, Prof. Hiroaki Kusunose, and Prof. Hisatomo Harima, provided the theoretical considerations for this study. I would like to sincerely thank them for their extensive support.

Over the six years in this laboratory, I have learned a great deal and accumulated numerous valuable experiences. Prof. Tatsuya Yanagisawa and Dr. Hiroyuki Hidaka provided crucial comments and encouragement through regular discussions. The every day moments with the lab. members are cherished memories, and their vibrant activities inspired me and motivated my own research. I'd like to express my gratitude to all the members, including the graduate students, who shared moments with me in this laboratory.

While there were moments of challenge in my research, I am particularly thankful to Prof. Hiroshi Amitsuka for consistently providing patient guidance and encouragement in every situation. I not only gained knowledge in physics but I also learned the fascination of experimental research. I express my heartfelt thanks to him for providing me with numerous valuable experiences despite my many shortcomings and immaturity as a researcher.

Finally, I extend profound gratitude to my family and friends who have always supported and encouraged me throughout this research life.

# Abstract

## **【Background and Objectives】**

Many studies on U intermetallic systems driven by the unique properties of 5f electrons, have yielded a variety of fascinating research topics. Despite its extensive history, however, a comprehensive understanding of 5f electrons remains elusive. A significant part of the challenge stems from the unique nature of the 5f electron wavefunction, which spatially lies between the more localized 4f and the more extended 3d electron wavefunctions. Reflecting this feature, 5f electrons are considered to be more strongly affected by their environment than 4f electrons through hybridization effects. As a result, 5f electrons exhibit a duality of both itinerancy and localization, leading to the emergence of various types of correlations between magnetism and superconductivity, which are not typically observed in 3d or 4f electron systems. Furthermore, the moderate localization in environments where spatial inversion symmetry is broken may induce local parity mixing, potentially activating odd-parity multipoles on a single ion site that have not yet been observed, possibly contributing to the exotic phenomena seen in U-based systems. However, microscopic information to comprehensively discuss such hybridization effects for each specific material remains scarce. This study aims to meticulously investigate the effects of the U-site environment, particularly focusing on the absence of local space inversion symmetry, on the hybridization of 5f electrons.

## **【Contents】**

In this study, we focus on  $\text{UPt}_2\text{Si}_2$  and  $\text{UIr}_2\text{Si}_2$  with  $\text{CaBe}_2\text{Ge}_2$  type structure to explore 5f electronic states in environments lacking the local inversion symmetry. This thesis consists of the following contents.

---

### **Resonant X-ray Scattering Experiments on $\text{UPt}_2\text{Si}_2$ (Chapter 5)**

On  $\text{UPt}_2\text{Si}_2$ , where charge density wave (CDW) is formed by 5d electrons of Pt, resonant X-ray scattering (RXS) experiments at the  $M_4$  absorption edge of U were performed to investigate the effect of environmental changes at the U site, which caused by the CDW ordering, on the 5f electronic state. We found the modulation of 5f electronic states by the CDW and analyzed their symmetries.

### **Neutron Scattering Experiments on $\text{UPt}_2\text{Si}_2$ (Chapter 6)**

To obtain quantitative information on the modulation of the 5f electronic state by the CDW, we performed polarized and unpolarized neutron diffraction experiments. The structure of the magnetic modulation was determined, including its absolute value of the amplitude.

### **Low Temperature Physical Properties in $\text{UIr}_2\text{Si}_2$ (Chapter 8)**

magnetic field ( $H$ ) versus temperature ( $T$ ) phase diagram has been constructed from the results of detailed magnetization and specific heat measurements under magnetic field for an antiferromagnet  $\text{UIr}_2\text{Si}_2$ , in which a strong hybridization between the conduction electrons and the 5f electrons is suggested.

Chapter 1 describes the background of this study and the development and current status of research on hybridization effects between conduction electrons and f electrons (1.1) and on multipole degrees of freedom (1.2), and contains the introduction on the interest in the 5f electronic states under the condition lacking of local inversion symmetry (1.3). Chapter 2 introduces the family of  $UT_2X_2$  compounds, including  $UPt_2Si_2$  and  $UIr_2Si_2$ . Chapter 3 summarizes the objectives of this study, and Chapter 4 describes the experimental method of these studies.

Chapter 7 and 9 provide the discussions based on the results obtained for each material. Chapter 10 presents the conclusions and perspectives of this study.

---

## **【Conclusions】**

The new insights gained from the research presented in this dissertation can be summarized as follows:

### **$UPt_2Si_2$**

- We found, from the RXS experiments, the orbital modulation of U 5f electrons induced by the CDW, manifesting as a density wave of electric quadrupoles. This orbital modulation exhibits an antiphase pattern between the U sublattices, possibly reflecting the polar environment on the U site inverted between the sublattices.
- We also found from polarized and unpolarized neutron scattering experiments, the magnetic modulation in U 5f electrons, where the magnetic moments in the antiferromagnetic (AFM) ordered state are canted away from the  $c$  axis. Our quantitative analysis on the magnetic modulation have revealed that the canting angle is approximately  $20^\circ$  at maximum, suggesting a significant coupling between the 5f electrons of U and the 5d electrons of Pt.

These results offer insights into the effects of the U-site environment on the 5f electronic state from two perspectives: inter-site d-f hybridization and intra-site 5f-6d or 7s hybridization. The estimated value of the canting angle of the 5f magnetic moment suggests a strong coupling between the U 5f electrons and the Pt 5d electrons, i.e., an inter-site d-f hybridization effect. This scenario predicts the occurrence of an antiphase orbital modulation between the U sublattices, which is supportively observed in the RXS experiments. Simultaneously, this implies that the 5f electrons reflect the absence of local inversion symmetry at the U site. That is exactly the situation where intra-site parity hybridization can occur. Such a parity mixed state is specified by an odd-parity multipole on a single ion site, which cannot be observed in the standard RXS experiments.

Our quantitative and symmetry analysis of the 5f electronic states offers valuable insights for a further microscopic understanding of hybridization effects in 5f electron systems. Future perspectives include crystallographic analysis to identify the

environment of the U site in more detail and further RXS experiments for the direct observations of the Pt 5d electrons and U 6d electrons.

### **UIr<sub>2</sub>Si<sub>2</sub>**

- We obtained the  $H$ - $T$  phase diagram that exhibits a characteristic feature with a phase boundary having  $dH_c(T)/dT > 0$  as  $T \rightarrow 0$  and possessing a triple critical point. In particular, the existence of the triple critical point is a common feature with a related material UIr<sub>2</sub>Ge<sub>2</sub>, indicating a low-dimensional spin network that reflects the layered structure in both systems.
- Our measurements of specific heat and magnetization suggest that the 5f-electronic states in UIr<sub>2</sub>Si<sub>2</sub> may form heavy-fermion states at two distinct energy scales as the temperature decreases. One arises in the high-temperature paramagnetic region, yielding an electronic specific heat coefficient  $\gamma = 110$  mJ/K<sup>2</sup>mol extrapolated from above the Néel temperature ( $T_N$ ) to  $T = 0$ . The other state emerges in the low-temperature AFM state, with an enhanced  $\gamma$  value of 270 mJ/K<sup>2</sup>mol. This transition is also evident from the drastic changes in the Curie-Weiss temperature, as well as the significant enhancement of the magnetic susceptibility at low temperatures.

The properties of UIr<sub>2</sub>Si<sub>2</sub> revealed in this study are primarily influenced by the low-dimensionality features of the crystal structure rather than the local breaking of spatial inversion symmetry. The large  $\gamma$  value and the small AFM ordered magnetic moment observed at low temperature indicate the itinerant nature of the 5f-electronic state. In contrast, the magnetic responses such as the  $H$ - $T$  phase diagram and magnetization process can be qualitatively explained based on a localized spin model. This material is expected to play an important role in studying how the 5f electron state is understood under strong hybridization effects.



# Contents

<b>1</b>	<b>Introduction</b>	<b>8</b>
1.1	Strongly Correlated System: intermetallic f-electron systems . . . . .	8
1.1.1	c-f hybridization effect . . . . .	8
1.1.2	c-f hybridization effect in U intermetallic systems . . . . .	9
1.2	Multipole Degrees of Freedom . . . . .	11
1.2.1	Conventional multipoles . . . . .	11
1.2.2	Augmented multipoles . . . . .	11
1.3	interest in 5f electronic states under lacking of local inversion symmetry	15
<b>2</b>	<b>Introduction to <math>UT_2X_2</math></b>	<b>16</b>
2.1	Crystal structures: $ThCr_2Si_2/CaBe_2Ge_2$ -type structures . . . . .	18
2.2	Various ground states in $UT_2X_2$ . . . . .	20
2.3	Physical Properties of $UPt_2Si_2$ . . . . .	22
2.4	Physical Properties of $UIr_2Si_2$ . . . . .	29
<b>3</b>	<b>Purpose of Study</b>	<b>31</b>
<b>4</b>	<b>Experimental Methods</b>	<b>32</b>
4.1	Sample preparation . . . . .	32
4.2	Resonant X-ray Scattering Experiment . . . . .	34
4.2.1	Principle of resonant X-ray scattering experiment . . . . .	34
4.2.2	Types of resonance processes . . . . .	38
4.2.3	Detection of multipoles by resonant x-ray scattering . . . . .	39
4.3	Neutron Scattering Experiment . . . . .	43
4.3.1	Unpolarized neutron diffraction measurement . . . . .	43
4.3.2	Polarized neutron diffraction measurement . . . . .	46
4.4	Magnetization and Specific heat measurements . . . . .	48
<b>5</b>	<b>Resonant X-ray Scattering Experiments on <math>UPt_2Si_2</math></b>	<b>49</b>
5.1	Experimental Procedure . . . . .	49
5.2	Results . . . . .	50
5.2.1	$Q = 0$ magnetic reflections . . . . .	50
5.2.2	Search for superlattice reflections . . . . .	52
5.2.3	$q_{CDW}$ reflections . . . . .	54

5.2.4	$2\mathbf{q}_{\text{CDW}}$ and $3\mathbf{q}_{\text{CDW}}$ reflections . . . . .	57
5.2.5	$\boldsymbol{\tau} + \mathbf{q}_{\text{CDW}}$ reflections . . . . .	60
5.2.6	Short summary of results in RXS experiments . . . . .	66
<b>6</b>	<b>Neutron Scattering Experiments on <math>\text{UPt}_2\text{Si}_2</math></b>	<b>68</b>
6.1	Experimental Procedure . . . . .	68
6.2	Experimental Results . . . . .	71
6.2.1	$\mathbf{Q} = 0$ magnetic reflections . . . . .	71
6.2.2	$\mathbf{q}_{\text{CDW}}$ reflections . . . . .	75
6.3	Short summary of results in neutron scattering experiments . . . . .	83
<b>7</b>	<b>Discussion – <math>\text{UPt}_2\text{Si}_2</math></b>	<b>84</b>
7.1	Diffraction patterns and modulation types . . . . .	84
7.2	Origin of modulation in 5f electronic states by CDW . . . . .	88
7.3	Atomic displacements . . . . .	91
7.4	Higher harmonics components in the magnetic modulation . . . . .	91
<b>8</b>	<b>Low Temperature Physical Properties in <math>\text{UIr}_2\text{Si}_2</math></b>	<b>93</b>
8.1	Magnetization measurements . . . . .	93
8.2	Specific heat measurement . . . . .	98
<b>9</b>	<b>Discussion – <math>\text{UIr}_2\text{Si}_2</math></b>	<b>103</b>
9.1	Tri-critical point on the AFM phase boundary . . . . .	103
9.2	5f electronic states in $\text{UIr}_2\text{Si}_2$ . . . . .	104
<b>10</b>	<b>Concluding remarks</b>	<b>107</b>

# Chapter 1

## Introduction

### 1.1 Strongly Correlated System: intermetallic f-electron systems

In f-electron intermetallic compounds, the hybridization effect between conduction electrons and localized f-electrons, called c-f hybridization, is one of the most important effects affecting their physical properties. This section provides the brief summary of the development and current status of the studies on the c-f hybridization effect.

#### 1.1.1 c-f hybridization effect

In metallic compounds containing lanthanide and actinide elements, there exists a group of materials in which the effective mass of electrons can reach  $10^2$  to  $10^3$  times at low temperatures. These materials are referred to as “heavy fermion (HF) systems”. Among them, Ce compounds are representative HF materials which have been actively studied for many years as a research field of rich physical phenomena. The overall framework of the properties of f electron systems with c-f hybridization effects is explained by the “Doniach phase diagram” (Fig. 1.1), which is derived from the competition between the Ruderman–Kittel–Kasuya–Yosida (RKKY) interaction and the Kondo effect [1]. The energy scales of the Kondo effect and the RKKY interaction ( $k_B T_K$  and  $k_B T_{\text{RKKY}}$ , respectively) are attributed to (i) the exchange coupling constant  $J_{\text{cf}}$  between the conduction electron and the localized electron and (ii) the density of states at the Fermi energy,  $D(\varepsilon_F)$ , but their functional forms are different (Eq. (1.1)). Reflecting this difference, the ground state of the system changes with variations in the magnitude of  $J_{\text{cf}}$ . While the 4f electron behaves as a localized electron with large magnetic moment of several  $\mu_B$  at high temperatures, the magnetic moment is screened by the antiferromagnetically coupled spins of the conduction electrons at low temperatures through the Kondo effect. At further low temperatures, the formation of a Kondo lattice, a periodic arrangement of Kondo singlet states, leads to a coherent state throughout the crystal with a narrow band near the Fermi energy (HF states). In the region with small  $J_{\text{cf}}$ , the 4f magnetic moments are dominantly

coupled by the RKKY interaction mediated by the conduction electrons, and the system shows the magnetic ordering. In the vicinity of the quantum critical point (QCP), where the RKKY interaction and the Kondo effect are competing, various physical phenomena such as quantum phase transitions, non-Fermi liquid states, and non-BCS superconductivity have been discovered. In the region with larger  $J_{cf}$ , on the other hand, valence fluctuation phenomena are pronounced.

$$\begin{aligned} k_B T_K &\propto D(\varepsilon_F)^{-1} \exp(-1/D(\varepsilon_F)J_{cf}) \\ k_B T_{\text{RKKY}} &\propto J_{cf}^2 D(\varepsilon_F) \end{aligned} \quad (1.1)$$

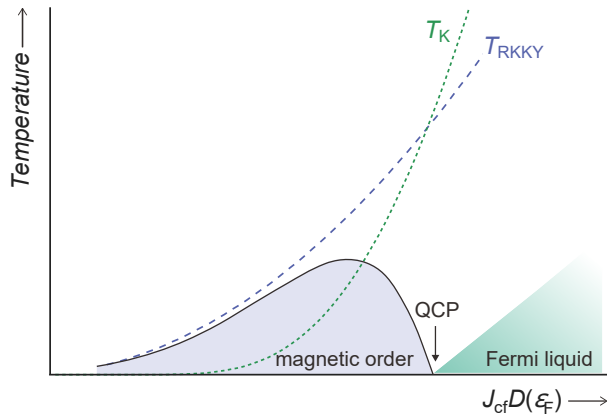


Figure 1.1: The Doniach phase diagram.

The key parameter,  $J_{cf}$ , originates from the hybridization effect between conduction electrons and f electrons, i.e., c-f hybridization on the basis of Anderson Hamiltonian, and their relationship is given as follows;

$$J_{cf} \propto \frac{V_{cf}^2}{\varepsilon_F - E_f} \quad (1.2)$$

Here,  $V_{cf}$  is the hybridization matrix element for the c-f hybridization and  $E_f$  is the energy level of the f orbital. This means that the c-f hybridization plays more fundamental role in the physical properties of the HF systems.

### 1.1.2 c-f hybridization effect in U intermetallic systems

The above discussion primarily assumes the relatively simple electronic structure of  $\text{Ce}^{3+}(4f^1)$ . In this context, the f-electrons are assumed to be well-localized, and the c-f hybridization effect is treated perturbatively. In the U systems, however, there are some fundamental issues to consider when discussing the c-f hybridization effect.

First one is the spatial extent of the wave functions. As shown in Fig. 1.2, the wave function of the 4f electron has a peak closer to the nucleus than that of the 5p electrons of the Xe closed shell. Therefore, the localized electron model can be a good

starting point of approximation for the 4f electrons. Similarly, the wave function of 5f electron also has a peak inside the Rn closed shell, but it extends further outside the closed shell compared to the 4f electrons, for which a localized electron state is a good approximation. This suggests that the 5f electrons are more strongly influenced by the surrounding environment than the 4f electrons. Nevertheless, the spatial extent of the 5f electrons is not as large as that of the 3d electrons, where the electron band model is a good approximation. This intermediate nature of the spatial extent of the wave function, between 3d and 4f electrons, makes it difficult to establish an appropriate model to describe the behavior of 5f electrons in metals..

In addition, we have to consider many-body effects within the 5f orbital. The electron configuration of U ion in a solid is typically considered to be  $U^{3+}$  ( $5f^3$ ) or  $U^{4+}$  ( $5f^2$ ), with multiple electronic occupying the 5f orbital. Consequently, direct Coulomb interactions and exchange interactions (Hund's rule coupling) occur between the electrons within the 5f orbital, making it a complex issue. to determine the resulting electron configuration. It becomes a complex issue to determine the resulting electronic configuration.

An example of studies addressing the issue of 5f electronic states is the theory of "itinerant-localized duality" (Yotsuhashi-Miyake-Kusunose theory) [2]. This theory was proposed focusing on the coexistence of the antiferromagnetic (AFM) ordering and the superconductivity discovered in  $UPd_2Al_3$ . This system shows the AFM ordering below 14.4 K and the superconductivity below 1.9 K in the AFM ordered state [3, 4]. The unique point is that the 5f electrons of U carry both the itinerant component, which exhibits superconductivity, and the localized component, contributing to anisotropic magnetism. According to the itinerant-localized duality mode [2], this feature is explained as a consequence of the three 5f electrons being composed of an itinerant component ( $5f^1$ ) and a localized component ( $5f^2$ ) with different amplitudes of c-f hybridizations. Although there are theoretical considerations regarding the behavior of 5f electrons in such specific systems, the properties of 5f electrons in U compounds are diverse, as shown in the later section 1.3, and a comprehensive understanding has not yet been achieved.

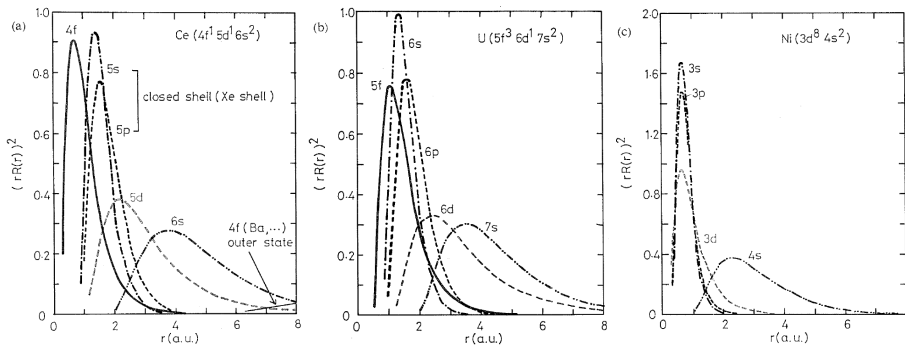


Figure 1.2: Effective radial distribution function of Ce, U and Ni [5].

## 1.2 Multipole Degrees of Freedom

Some f-electron systems exhibit unique ordered states with the anisotropic electric or magnetic order parameters which can be described by “multipoles”. These ordered states have been found not only in insulators with the strong localized character of f electrons, but also in the intermetallic systems with the c-f hybridization as described above. In order to explain these phenomena, it is necessary to understand how the entangled degrees of freedom due to their strong spin-orbit coupling interact with the surrounding environment in crystals.

For f-electron systems, symmetry analysis is a powerful way to deal with their degrees of freedom. According to Neumann’s principle, the symmetry of any physical property in a crystal must be higher than, or at least equal to, its crystallographic point group symmetry. This means that the symmetry of the electronic state provides information about the expected physical properties. Recently, based on this point, electronic states in materials have been classified in terms of symmetry, and a complete set of multipole basis for describing any electronic state in a crystal has been obtained. In this section, we briefly introduce the development and current status of research on such multipole degrees of freedom.

### 1.2.1 Conventional multipoles

Multipoles appear in a series expansion of scalar and vector potentials in classical electromagnetism, and symmetry of electronic states can be expressed using the concept of multipoles. In f-electron systems, many materials have been discovered that exhibit a spontaneous ordering of the multipoles, such as electric quadrupoles and magnetic octupoles. Representative examples are the antiferro-electric-quadrupole ordering in  $\text{CeB}_6$  [6] and the antiferro-magnetic-octupole ordering in  $\text{Ce}_{0.7}\text{La}_{0.3}\text{B}_6$  [7]. These multipoles can be arisen as electronic degrees of freedom for a single orbital on a single ion site. In such cases, their spacial inversion symmetry is restricted to even parity. Recently, there has been a breakthrough to extend this conventional concept of multipoles for the comprehensive expression of electronic states in crystals, as described below.

### 1.2.2 Augmented multipoles

Recently, four types of multipoles have been established that constitute a complete set for representing arbitrary electric states in terms of spatial inversion symmetry and time reversal symmetry. As listed in Fig. 1.3, they cover all the combinations of spatial inversion symmetry and time reversal symmetry ( $\mathcal{P}$ ,  $\mathcal{T}$ ).

A comprehensive description of the electronic state using these extended multipoles can easily predict the possible responses of the system to various external fields, such as electromagnetic field, electric currents, and elastic strain. This is because the various response tensors correspond one-to-one to the symmetries of the system that can be represented by multipoles. Figure 1.4 summarizes the relationship between multipoles

and the expected linear responses. For example, if odd-parity magnetic multipoles uniformly order in the system, magneto-electric effects can be observed. In this case, applying an electric field to the system induces magnetization and the response tensor can be described by the multipoles ordering in the system as in Eq. (1.4).

















type	symbol	spatial inversion	time reversal	monopole	dipole	quadrupole	octupole
E	$Q_{lm}$	$(-1)^l$ polar	+	(+, +) 			
M	$M_{lm}$	$(-1)^{l+1}$ axial	-	(-, -) 			
MT	$T_{lm}$	$(-1)^l$ polar	-	(+, -) 			
ET	$G_{lm}$	$(-1)^{l+1}$ axial	+	(-, +) 			

Figure 1.3: (Color online) Four types of multipoles (E: electric multipole, M: magnetic multipole, MT: magnetic toroidal multipole, ET: electric toroidal multipole) and their symmetries in Ref. [8].  $l$  is the rank of multipoles.

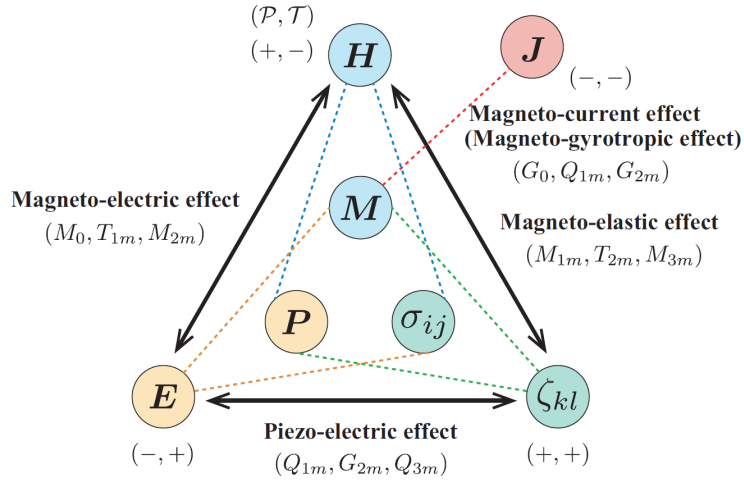


Figure 1.4: Heckmann diagram in Ref. [9].

$$\mathbf{M} = \hat{\alpha}^{(E)} \mathbf{E} \quad (1.3)$$

$$\hat{\alpha}^{(E)} = \begin{pmatrix} M_0 - M_u + M_v & M_{xy} + T_z & M_{zx} - T_y \\ M_{xy} - T_z & M_0 - M_u - M_v & M_{yz} + T_x \\ M_{zx} + T_y & M_{yz} - T_x & M_0 + 2M_u \end{pmatrix} \quad (1.4)$$

In the following, three types of extensions made in the definition of multipoles to realize odd-parity multipoles in real materials will be introduced.

### Cluster-type multipole

When a system exhibits an electronic order, the symmetry of the entire system can be represented by the symmetry of the ordered unit cell rather than focusing on the individual electronic degrees of freedom on a single site. Noting this point, the cluster-type multipoles are defined on over multiple sites [10, 11, 12].

A representative material of clustered multipoles is  $\text{UNi}_4\text{B}$ . This material has a honeycomb network of U. Below 20.4 K, this system shows a vortex-like antiferromagnetic order on the network [13]. The symmetry of the magnetic structure is characterized by the vortex-like spin network, which corresponds to a uniform order of cluster-type magnetic toroidal dipole [10]. In fact, our group has succeeded in examining the magneto-electric effects induced by these magnetic multipoles [14].

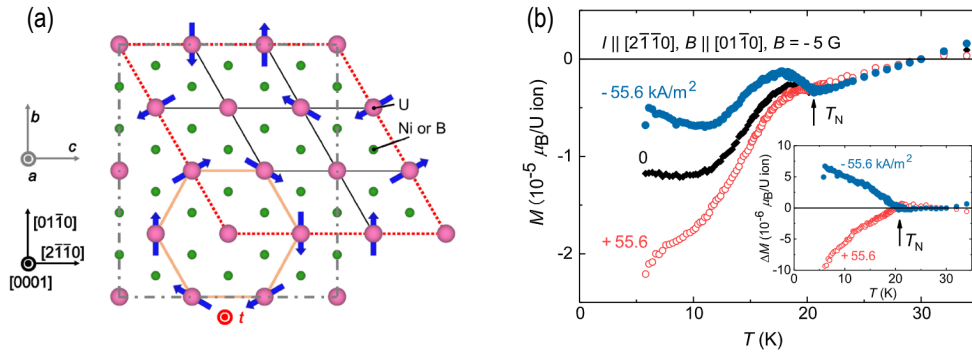


Figure 1.5: (Color online) (a) The magnetic structure of  $\text{UNi}_4\text{B}$  and corresponding the cluster-type magnetic toroidal dipole and (b) the observed magnetization induced by electric currents [14].

### Bond-type multipole

There is another type of multipole defined across multiple sites. It is a bond-type multipole, which is defined to represent the anisotropic modulation of electric hopping [15]. In other words, a bond-type multipole can be regarded as off-site electronic degrees of freedom, while a cluster-type multipole is composed of on-site electronic degrees of freedom.

One of the candidate materials exhibiting the bond-type multipole ordering is the 5d pyrochlore metal  $\text{Cd}_2\text{Re}_2\text{O}_7$ . This system undergoes successive phase transitions at  $\sim 200$  K and 120 K with the structural changes [16], which have been proposed to be associated with electric-toroidal quadrupole orderings [17].



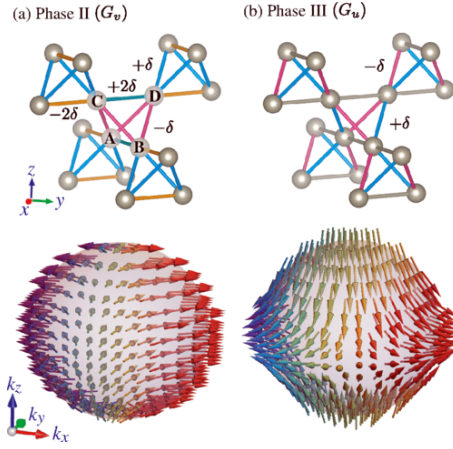


Figure 1.6: (Color online) The bond-type electric toroidal quadrupole order proposed in  $\text{Cd}_2\text{Re}_2\text{O}_7$  [17].

### Hybrid-type multipole

In contrast to the previous two types of extended multipoles, there is another type of multipole which is defined on a single site. This is a hybrid-type multipole, which represents the hybridization between different orbitals in a single ion site [18, 19]. In principle, a parity-mixing hybridization between orbitals such as s-p, p-d, and d-f is allowed on a single site lacking local inversion symmetry in the presence of odd-parity crystalline electronic field (CEF). It means that odd-parity multipoles can be active even at a single site.

In f electron systems, such intra-atomic parity-mixing effects have not been discussed so far. This is because, as explained in Section 1.1, the f electrons are well localized in the inner shell, and the odd-parity CEF is considered to be shielded by the outer shell electrons. However, in the case of the 5f electrons, the spatial spread of their wavefunction suggest that the 5f electrons may contribute to the shielding of the odd-parity CEF. The resulting interorbital (e.g. 5f-6d) hybridization states can be precisely regarded as the odd-parity hybrid-type multipoles. We are focusing on the possibility that this new electronic degree of freedom may play a key role in understanding the physical phenomena mentioned in the next chapter.

### 1.3 interest in 5f electronic states under lacking of local inversion symmetry

In addition to the  $\text{UPd}_2\text{Al}_3$  introduced in Section 1.1.2, several other U compounds have been found that exhibit unique 5f electronic properties. The representative materials are summarized in Fig. 1.7.

In recent years, the coexistence of ferromagnetic ordering and superconductivity has been studied intensively. This phenomenon has been discovered in  $\text{UCoGe}$  [20],  $\text{URhGe}$  [21], and  $\text{UGe}_2$  [22]. As in the case of  $\text{UPd}_2\text{Al}_3$ , the magnetic ordering and superconductivity coexist microscopically, and both are caused by 5f electrons. All of these systems commonly exhibit the field-reentrant (-reinforced) superconductivities with large upper critical fields [23]. Such properties are also found in  $\text{UTe}_2$  [24], which was recently discovered to exhibit the superconductivity with strong magnetic fluctuations. In each of these materials, the local space inversion symmetry at the U site is lacking. Besides, also in HF compounds that exhibit complex superconducting multiple phase diagrams, such as  $\text{UPt}_3$  [25, 26] and  $(\text{U}, \text{Th})\text{Be}_{13}$  [27, 28, 29, 30], the local inversion symmetry at the U sites are lacked. It should be noted that, in  $\text{URu}_2\text{Si}_2$ , which shows an enigmatic “hidden order” (HO) [31, 32, 33, 34], it has been proposed that the HO transition may occur with the breaking of the local inversion symmetry at the U site [35, 36, 37]. Focusing on the common features of the crystal structures in these materials, we expect that the hybrid-type odd-parity multipoles may play an important role for understanding these peculiar phenomena.

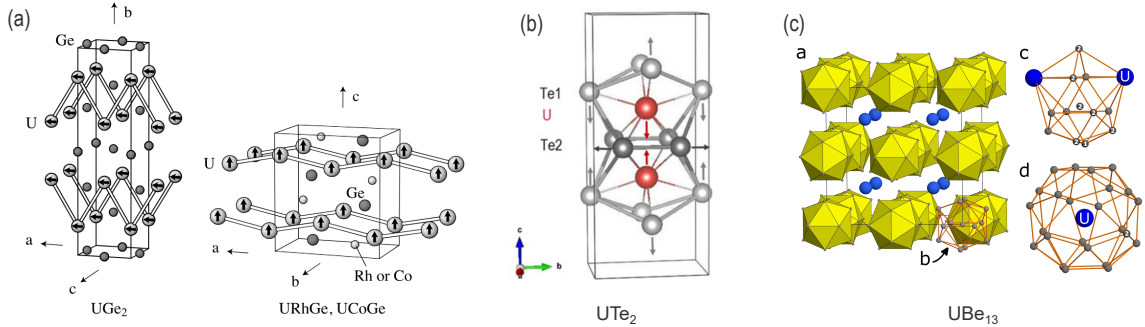


Figure 1.7: The crystal structures of representative exotic U systems: (a)  $\text{UGe}_2$ ,  $\text{URhGe}$  and  $\text{UCoGe}$ [23] (b)  $\text{UTe}_2$  [38], (c)  $\text{UBe}_{13}$  [39].

# Chapter 2

## Introduction to $UT_2X_2$

The family of  $RT_2X_2$  ( $R$ : lanthanide/actinide,  $T$ : transition metal,  $X = \text{Si/Ge}$ ) compounds has a long history as a platform for systematic research of intermetallic f-electron systems. A large number of compounds with various properties have been synthesized and their properties have been investigated extensively. Among these, the group of compounds with  $R = \text{Ce, U}$  has been particularly intensively studied. In this study, to investigate the 5f electronic states in environments lacking the local inversion symmetry and to explore the effects of c-f hybridization, we focused on the group of  $UT_2X_2$  compounds with two different crystal structures as introduced in the following section.

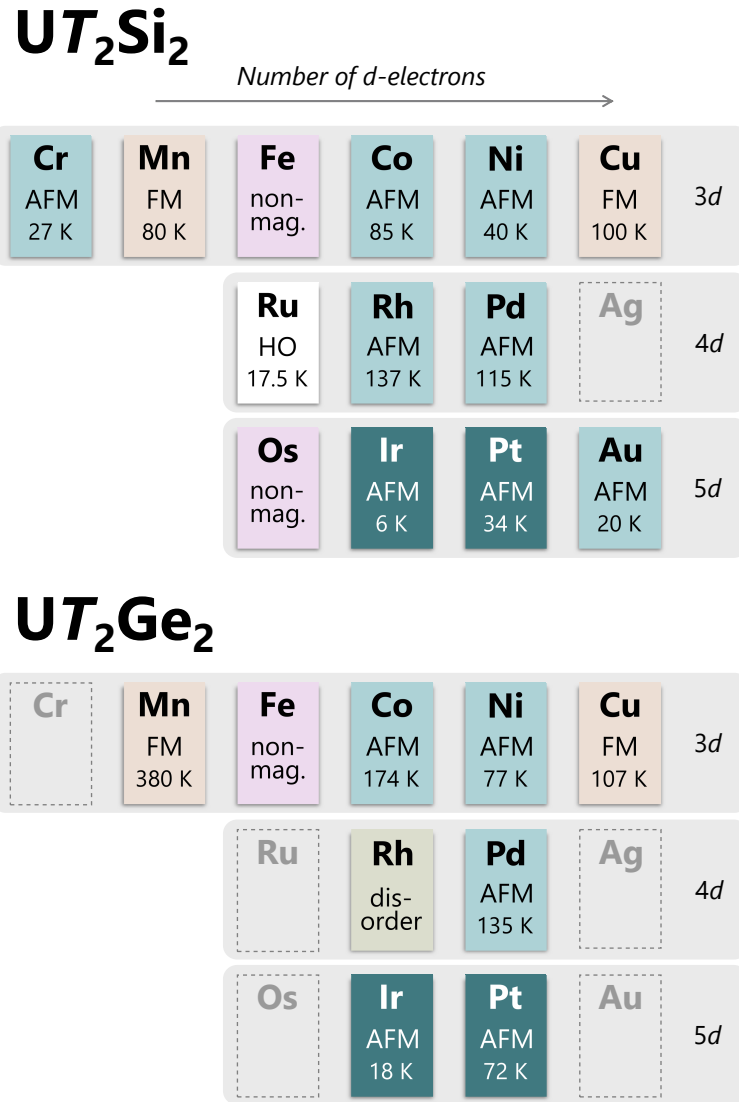


Figure 2.1: (Color online) List of ground states of  $UT_2Si_2$  and  $UT_2Ge_2$  extended on the basis of Dr. Tabata's Ph. D. thesis [40] and the study by Endstra *et al* [41]. Note that  $URu_2Si_2$  is shown with its hidden order (HO) instead of the superconducting state. Materials with  $ThCr_2Si_2$ -type structure are written in black font, while those with the  $CaBe_2Ge_2$ -type structure are written in white one. The dashed lines indicate that they have not been reported.

## 2.1 Crystal structures: $\text{ThCr}_2\text{Si}_2/\text{CaBe}_2\text{Ge}_2$ -type structures

The uranium intermetallics  $UT_2X_2$  form a large family of compounds having a rich variety of novel ground states: unconventional superconductivity, metallic magnetism, heavy fermion or non-Fermi-liquid states, coexistence among them, and so on. In this family, only four compounds ( $T = \text{Ir}/\text{Pt}$ ) have the  $\text{CaBe}_2\text{Ge}_2$ -type structure (space group: No. 129,  $P4/nmm$ ,  $D_{4h}^7$ ) (Fig. 2.2 (a)), while most of them crystallize in the  $\text{ThCrSi}_2$ -type tetragonal structure (space group: No. 139,  $I4/mmm$ ,  $D_{4h}^{17}$ ) (Fig. 2.2 (b)). Both structures are derivatives of the  $\text{BaAl}_4$ -type structure [42]. As shown in Fig. 2.3, they have two-dimensional characteristics, with atomic layers stacked perpendicular to the  $c$ -axis. Comparing these two structures, there is a difference in the stacking patterns. In the  $\text{CaBe}_2\text{Ge}_2$ -type structure, each U layer is sandwiched between a  $T$ - $X$ - $T$  layer (hereafter referred to as Layer 1) and a  $X$ - $T$ - $X$  layer (Layer 2) alternately. In contrast, in the  $\text{ThCr}_2\text{Si}_2$ -type one, each U layer alternates stacking with only Layer 2. The local inversion symmetry on U sites is present in the  $\text{ThCr}_2\text{Si}_2$ -type structure but not in the  $\text{CaBe}_2\text{Ge}_2$ -type structure. Therefore, this series of compounds is a suitable target for studying the effect of odd parity CEF on the 5f electronic states of U ions.

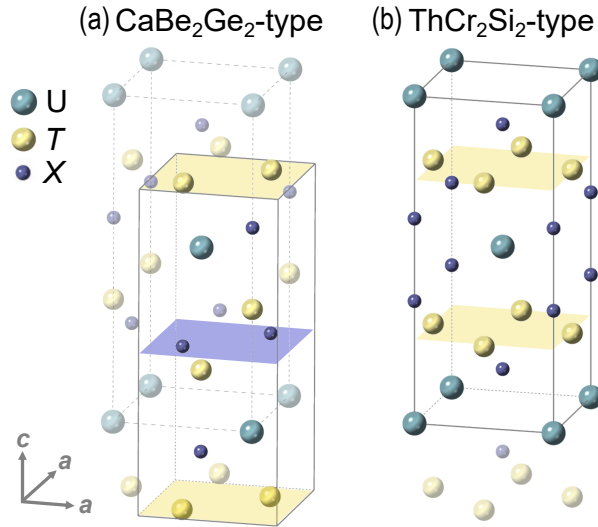


Figure 2.2: (Color online) Crystal structures of  $RT_2X_2$ : (a)  $\text{CaBe}_2\text{Ge}_2$ -type, (b)  $\text{ThCr}_2\text{Si}_2$ -type. The colored shaded areas enhance the visibility of the difference between these structures.

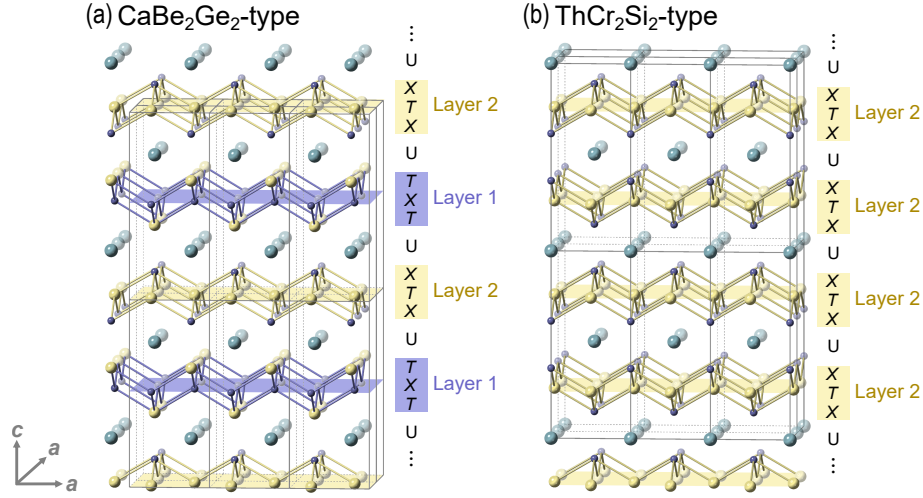


Figure 2.3: (Color online) The stacking patterns of the atomic layers in (a)  $\text{CaBe}_2\text{Ge}_2$ -type and (b)  $\text{ThCr}_2\text{Si}_2$ -type structures. The bold lines represent the unit cell in each structure. The colored shaded areas enhance the visibility of the atomic layers.

CaBe <sub>2</sub> Ge <sub>2</sub> -type structure					
space group: <i>No.</i> 129, $P4/nmm$ (origin choice 2)					
atom	x	y	z	site	symmetry
<i>R</i>	1/4	1/4	$z_R$	2c	$4mm$ ( $C_{4v}$ )
<i>T</i> (1)	1/4	1/4	$z_T$	2c	$4mm$ ( $C_{4v}$ )
<i>T</i> (2)	3/4	1/4	0	2a	$\bar{4}m2$ ( $D_{2d}$ )
<i>X</i> (1)	3/4	1/4	1/2	2b	$\bar{4}m2$ ( $D_{2d}$ )
<i>X</i> (2)	1/4	1/4	$z_X$	2c	$4mm$ ( $C_{4v}$ )
ThCr <sub>2</sub> Si <sub>2</sub> -type structure					
space group: <i>No.</i> 139, $I4/mmm$					
atom	x	y	z	site	symmetry
<i>R</i>	0	0	0	2a	$4/mmm$ ( $D_{4h}$ )
<i>T</i>	0	1/2	1/4	4d	$\bar{4}m2$ ( $D_{2d}$ )
<i>X</i>	0	0	$z_X$	4e	$4mm$ ( $C_{4v}$ )

Table 2.1: Atomic sites in the  $\text{CaBe}_2\text{Ge}_2$ -type structure (upper) and the  $\text{ThCr}_2\text{Si}_2$ -type structure (lower).

## 2.2 Various ground states in $UT_2X_2$

As shown in Fig. 2.1, most of them exhibit AFM ordering as their ground state, with variations in duality ranging from localized characteristics in  $UPd_2Si_2$  to the formation of spin density wave (SDW) reminiscent of itinerant magnetism in  $UCu_2Si_2$ . These systems are broadly understood within the framework of the Doniach model, commonly applicable to 4f systems. In this theory, the competition between RKKY interactions and Kondo effects due to d-f hybridization between  $T$ -ion d electrons and U 5f electrons dictates the variety in ground states. In the “d-f hybridization model” discussed by Endstra *et al.* [41], the relative change in strength of d-f hybridization ( $J_{df}$ ) was evaluated to explain their ordering temperatures on the basis of the Doniach phase diagram. They calculated relative values of  $J_{df}$  by considering the variations in U- $T$  ion distance and d-electron number across different  $T$  elements. As shown in Fig. 2.4, the ordering temperatures of each material appear to be roughly explained by this model. However, the model cannot explain individual physical features, and specific experimental data linking directly correlating d-f hybridization effects to the ground state characteristics of each compound are still scarce.

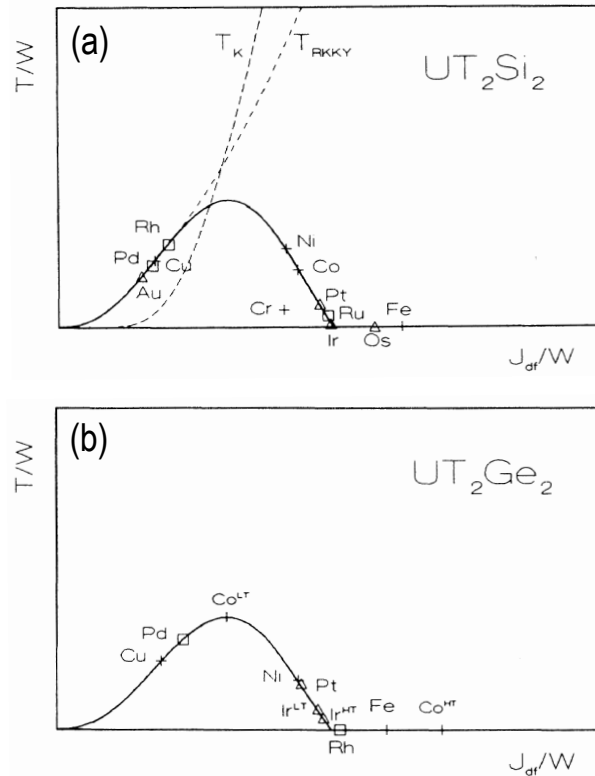


Figure 2.4: The comparison of experimental magnetic (or HO) transition temperatures in  $UT_2Si_2$  and  $UT_2Ge_2$  with the hybridization strength  $J_{df}$  estimated by Endstra *et al.* [41]. The curve denotes the magnetic phase expected based on the Doniach model.

It should be emphasized here that most of these studies have focused on the systems

with the  $\text{ThCr}_2\text{Si}_2$ -type structure. In the materials with  $\text{CaBe}_2\text{Ge}_2$ -type structures, which we are focusing on here, no detailed studies have been conducted except for  $\text{UPt}_2\text{Si}_2$ . This study, as the next step from my master's research work on  $\text{UIr}_2\text{Ge}_2$ , we performed microscopic studies by diffraction experiments on  $\text{UPt}_2\text{Si}_2$  and macroscopic measurements of the low temperature properties of  $\text{UIr}_2\text{Si}_2$ .



## 2.3 Physical Properties of $\text{UPt}_2\text{Si}_2$

### Magnetic properties

This system shows an AFM order below  $34 \pm 1 \text{ K} (\equiv T_N)$  [43, 44, 45]. As shown in Fig. 2.5(a), the magnetic susceptibilities along the  $c$ -axis ( $\chi_c$ ) and the  $a$ -axis ( $\chi_a$ ) show cusp anomalies near the  $T_N$ . While many  $\text{UT}_2\text{X}_2$  compounds exhibit uniaxial magnetic anisotropy with the  $c$  axis as the easy axis, the magnetic susceptibility of  $\text{UPt}_2\text{Si}_2$  is relatively isotropic. Above 200 K,  $\chi_c$  follows the Curie-Weiss law, and the effective moment and the Weiss temperature are estimated to be  $\mu_{\text{eff}} = 3.1\mu_B$  and  $\Theta_p = -60 \text{ K}$ , respectively[45]. The decrease in  $\mu_{\text{eff}}$  from the values for free ions ( $3.62 \mu_B$  for  $\text{U}^{3+}$ ,  $3.58 \mu_B$  for  $\text{U}^{4+}$ ) suggests the presence of CEF effects. In the magnetization process, multiple metamagnetic increases have been observed in the region of 20 T to 40 T. These behaviors suggest the complex magnetic structure in this system.

In the previous neutron scattering experiments, magnetic reflections developing below  $T_N$  have been observed at the forbidden positions for this crystal structure (e.g.,  $(1, 0, 0)$ , for example) as shown in Fig. 2.6 (a) [44, 43, 46]. They proposed the magnetic structure in which the magnetic moments of U 5f electrons are aligned parallel to the  $c$ -axis with a propagation vector of  $\mathbf{Q} = 0$  from their results (Fig. 2.6 (b)). The estimated magnitude of the ordered magnetic moment varies across the references, ranging from approximately  $1.67 \mu_B/\text{U}$  [44] to  $2.5 \mu_B/\text{U}$  [46].

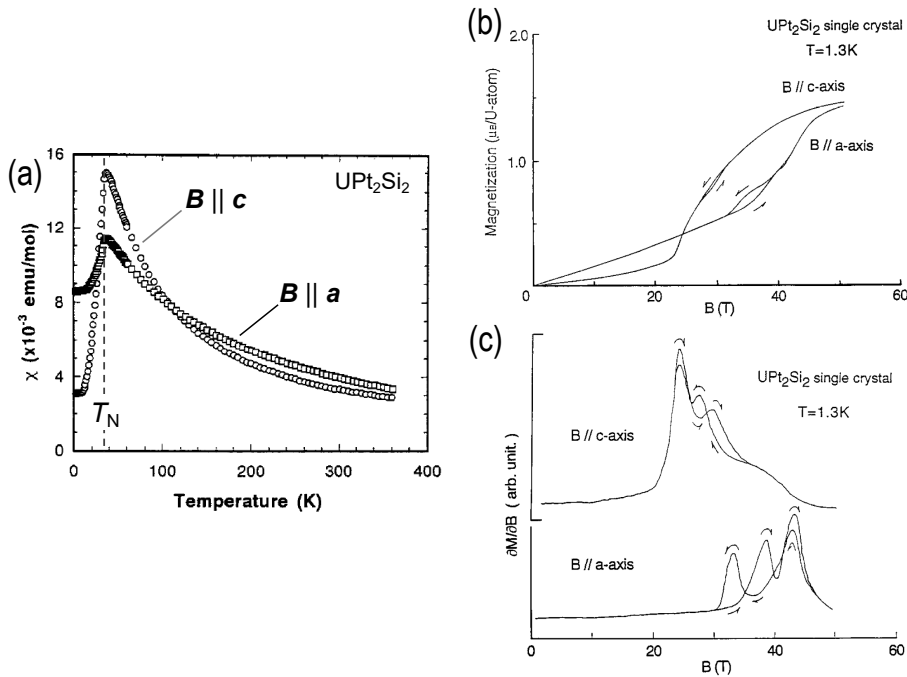


Figure 2.5: Data from magnetization measurements (under magnetic fields  $\parallel c$ - and  $a$ -axes) on the single crystal of  $\text{UPt}_2\text{Si}_2$ [45]: (a) the temperature dependence of the magnetic susceptibility, (b) the magnetization process, and (c) the field dependence of the differential susceptibility derived from the data in (b).

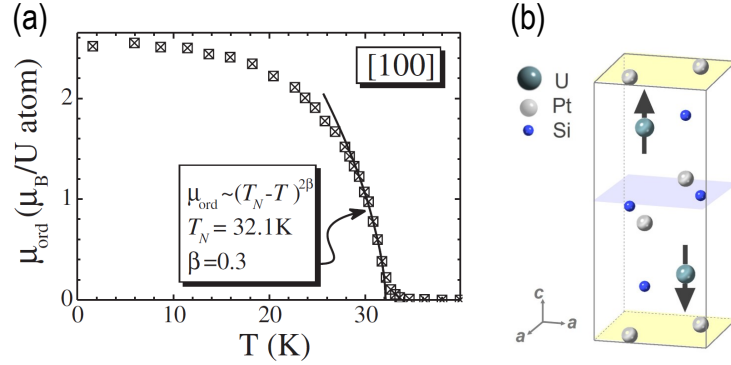


Figure 2.6: (a) The temperature dependence of the neutron-scattering intensity of (1, 0, 0) magnetic reflection [46] and (b) the proposed magnetic structure in the AFM phase.

### Specific heat and electric resistivity

Figure 2.7 displays the temperature dependence measured on the single crystal of  $\text{UPt}_2\text{Si}_2$ . The contribution of 5f electrons in the specific heat,  $C_{5f}$ , is estimated by subtracting the specific heat of  $\text{LaPt}_2\text{Si}_2$  as a phonon contribution. The temperature dependence of  $C_{5f}$  shows a lambda-type anomaly near  $T_N$ , and a broad shoulder on its high-temperature side, suggesting a Schottky anomaly associated with the CEF splitting. The electronic specific heat coefficient is estimated to be about 32 mJ/molK<sup>2</sup>, indicating only a slight increase in effective mass [45].

The temperature dependences of electrical resistivities along the  $c$  axis ( $\rho_c$ ) and the  $a$  axis are shown in Fig. 2.7 (b). In all temperature ranges,  $\rho_c$  is larger than  $\rho_a$ , and such anisotropy is similar to that of  $\text{UIr}_2\text{Si}_2$  [47] and  $\text{UIr}_2\text{Ge}_2$  [86] with the same crystal structure.

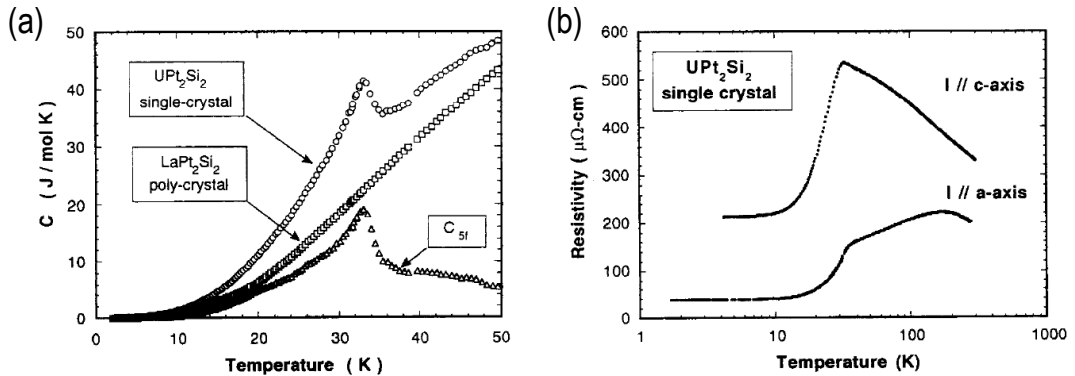


Figure 2.7: (a) Temperature dependences of specific heats in  $\text{UPt}_2\text{Si}_2$  and  $\text{LaPt}_2\text{Si}_2$  [45].  $C_{5f}$  is the contribution of 5f electrons in the specific heat estimated by subtracting the specific heat of  $\text{LaPt}_2\text{Si}_2$  from that of  $\text{UPt}_2\text{Si}_2$ . (b) The temperature dependences of the electrical resistivities of  $\text{UPt}_2\text{Si}_2$  along the  $a$ - and  $c$ -axes [45].

## CEF analysis

Given the large ordered magnetic moment and the slightly enhanced electronic specific heat coefficient, the magnetism in this system is basically discussed in terms of a well-localized 5f-electron picture within the  $UT_2X_2$  series. Inelastic neutron scattering experiments have notably observed anomalies suggestive of crystalline-electric-field (CEF) excitations, leading to the proposal of a singlet-singlet-doublet-singlet level scheme with  $J = 4$  ( $5f^2$ ) [48, 49]. Although this level scheme qualitatively reproduces the magnetic anisotropy and the AFM ordering of the system, the calculated ordered moment ( $2.9 \mu_B/U$ ) significantly exceeds the experimental value. This discrepancy is speculated to result from the screening of the magnetic moments due to the Kondo effect. In addition, subsequent studies by inelastic scattering experiments [50] and band calculations [51] have shown the itinerant nature of the 5f electrons. Further discussions are needed to understand the picture of the 5f electronic state in  $UPt_2Si_2$ .

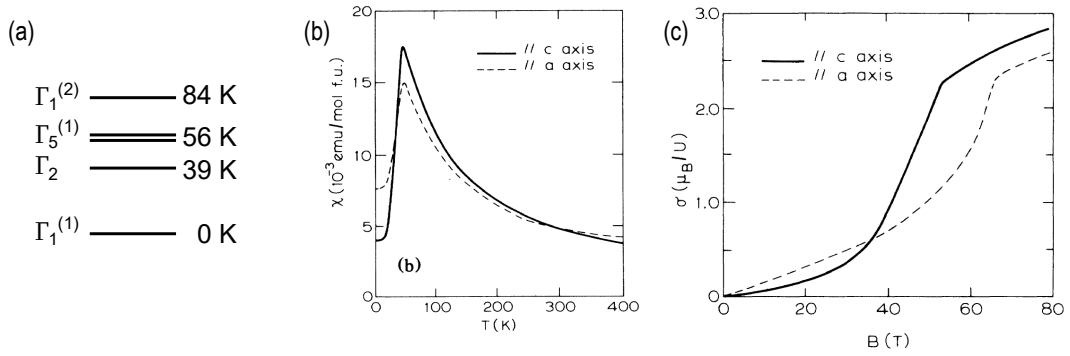


Figure 2.8: (a) The reported level scheme of CEF splitting from the calculation by Nieuwenhuys *et al.* (b) The calculated magnetic susceptibilities from the level scheme in (a). (c) The calculated magnetization processes from the level scheme in (a). [49]

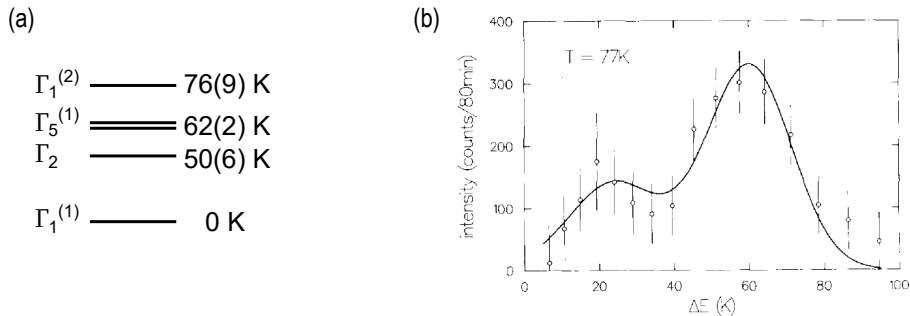


Figure 2.9: (a) The proposed level scheme of CEF splitting from the results of the inelastic neutron scattering experiments. (b) The elastic peak observed in the inelastic neutron scattering experiments [48].

## CDW order

Recently, the existence of another phase transition near room temperature has been found. The temperature dependence of electrical resistivities and specific heat [52], including the temperature region above room temperature, is shown in Fig. 2.10. Near 300 K, a lambda-shaped anomaly in specific heat and an increase in  $\rho_a$  are observed.

In the recent polarized neutron scattering and non-resonant X-ray scattering experiments, they found the non-magnetic superlattice reflections developing below about 320 K [53]. The diffraction pattern is shown in Fig. 2.11. Their results have revealed that the system exhibits a charge density wave (CDW) order by the 5d electrons of Pt with a propagation vector of  $\mathbf{q}_{\text{CDW}} = (\sim 0.42, 0, 0)$  below about 320 K ( $\equiv T_{\text{CDW}}$ ). The existence of harmonic components such as  $2\mathbf{q}_{\text{CDW}}$  and  $3\mathbf{q}_{\text{CDW}}$  is also confirmed. This diffraction pattern can be described by the single- $q$  CDW ordering, with the superposition of the  $\mathbf{q}_{\text{CDW}} \parallel \mathbf{a}^*$  domain and the  $\mathbf{q}_{\text{CDW}} \parallel \mathbf{b}^*$  domain. According to their structural analysis, this is mainly due to the 5d electrons of Pt in the second layer, accompanied by atomic displacements of Pt(2). Their analysis suggests that the displacement structure can be explained mainly as a transverse displacement in the  $c$ -plane. The results of an atomic pair-distribution-function (PDF) analysis reported very recently also support this result [54].

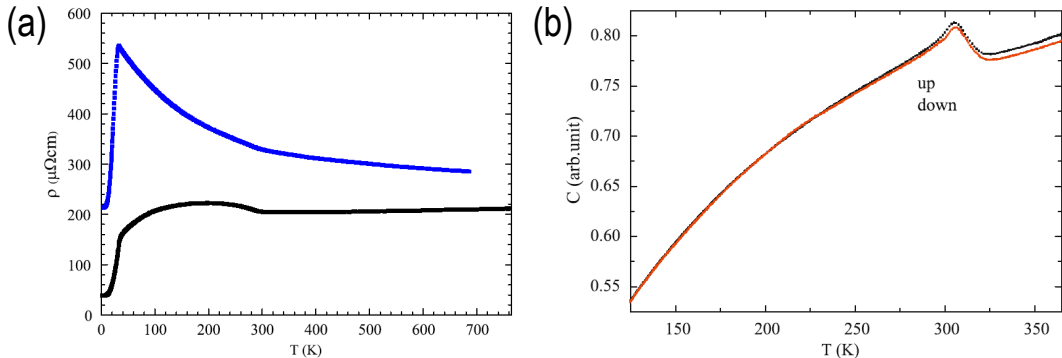


Figure 2.10: The temperature dependence of (a) electrical resistance and (b) specific heat [52].

The CDW orderings found in  $R\text{Pt}_2\text{Si}_2$  compounds are summarized in Table 2.2. They have the common feature that the transition temperature is about 100–300 K and the propagation vector  $\mathbf{q}_{\text{CDW}}$  is parallel to the  $a$  axis with the amplitude of about  $0.3\text{--}0.6\mathbf{a}^*$ . In the traditional scenario, the CDW is stabilized when the energy gain of electrons by the nesting of Fermi surfaces overcomes the loss of elastic energy. For these systems, (i) the two-dimensional Fermi surfaces and (ii) structural instability are thought to be responsible for the formation of CDWs. Related to (i), Fermi surfaces have been well studied in  $\text{SrPt}_2\text{As}_2$  and  $\text{LaPt}_2\text{Si}_2$  which show superconductivities [55, 56]. According to their band calculations for these systems, they have cylindrical Fermi surfaces from the Pt(2)-5d band as shown in Fig. 2.13, and these quasi-nesting features may be responsible for the CDW transitions. The existence of a similar two-

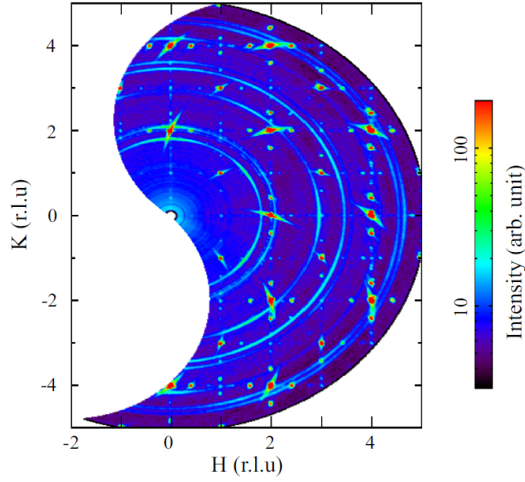


Figure 2.11: The diffraction patterns of fundamental lattice reflections and superlattice reflections associated with the CDW order observed in the neutron scattering experiments on  $\text{UPt}_2\text{Si}_2$  [53].

dimensional Fermi surface is also suggested by band calculations for  $\text{UPt}_2\text{Si}_2$  [51].

The detailed structural analysis has been performed on  $\text{UPt}_2\text{Si}_2$  by neutron diffraction experiments at 400 K ( $> T_{\text{CDW}}$ ), and they revealed that the atoms in Layer 2 have a large atomic displacement parameter within the  $c$ -plane. This feature may be related to (ii) of the reason for the stabilization of CDW in this system.

It is intriguing to note that the transverse atomic displacement occurs in association with the CDW order. If the CDW is simply a density wave in the charge distribution, the modulation should occur only in the direction of propagation and the associated atomic displacement should be longitudinal. The CDW order with the transverse atomic displacements reported in this system suggests a complex modulation of the charge distribution.

Such transversal atomic displacements were reported in  $\text{SrPt}_2\text{As}_2$  from the previous STM study [57], and the softening in the transverse phonon mode was observed in inelastic neutron scattering experiments on  $\text{LaPt}_2\text{Si}_2$  [58]. These facts indicate that the transversal atomic displacements a common feature of similar Pt-based systems, irrespective of the presence or absence of f electrons.

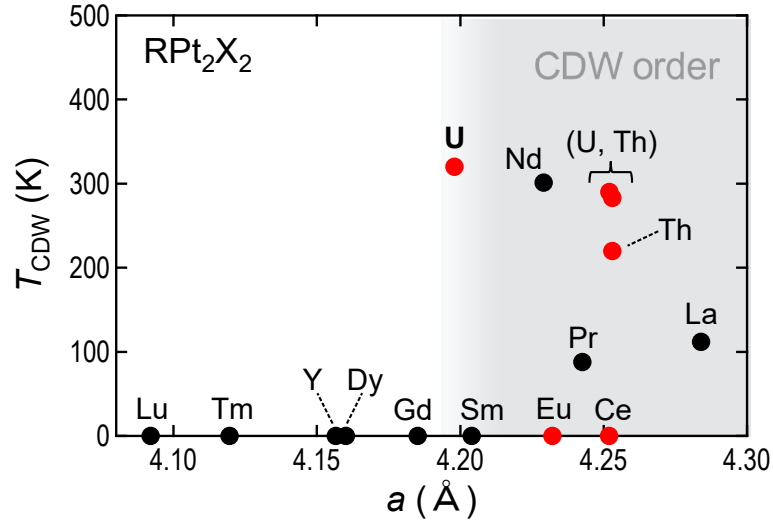


Figure 2.12: Relationship between CDW transition temperatures and lattice constants of  $a$  in  $RPt_2Si_2$ , based on the study by Nagano *et al.* [59], with the addition of red symbols. No CDW ordering is found for materials located below  $R = Pr$  (shown as  $T_{CDW} = 0$ ).

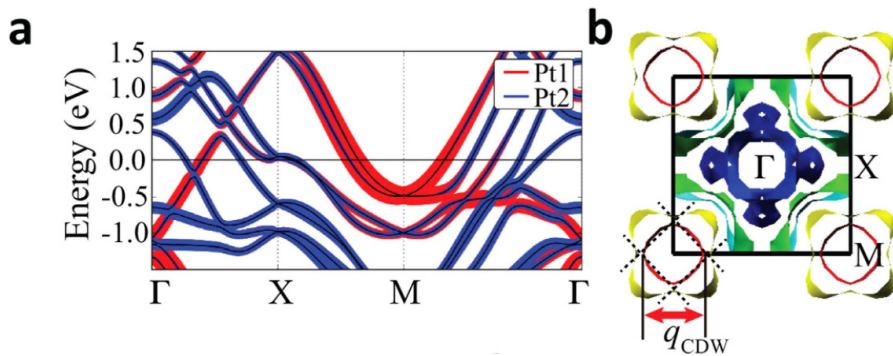


Figure 2.13: (a) The band structure and (b) the Fermi surface obtained from first-principles calculations performed for  $LaPt_2Si_2$  [56].

***RPt<sub>2</sub>Si<sub>2</sub>***

<i>An</i>	$T_c$	$T_N$	$T_{CDW}$	$q_{CDW}$	<i>Lattice constant at RT</i>	<i>Ref.</i>
UPt <sub>2</sub> Si <sub>2</sub>	-	35	320	0.42	4.198 ( <i>a</i> ), 9.694 ( <i>c</i> )	[53, 46]
ThPt <sub>2</sub> Si <sub>2</sub>	3 K	-	230	*	4.252, 9.762	**

<i>Ln</i>	$T_c$	$T_N$	$T_{CDW}$	$q_{CDW}$	<i>Lattice constant at RT</i>	<i>Ref.</i>
LaPt <sub>2</sub> Si <sub>2</sub>	1.87	-	112	0.36	4.288, 9.833	[59, 60]
NdPt <sub>2</sub> Si <sub>2</sub>	-	1.5	300	0.323	4.230, 9.780	[59, 61]
PrPt <sub>2</sub> Si <sub>2</sub>	-	-	88	*	4.243, 9.781	[62, 63]

***others***

<i>Ln</i>	$T_c$	$T_N$	$T_{CDW}$	$q_{CDW}$	<i>Lattice constant at RT</i>	<i>Ref.</i>
SrPt <sub>2</sub> As <sub>2</sub>	5.2	-	420	0.62	(orthrhombic)	[64]
LaPt <sub>2</sub> Ge <sub>2</sub>	0.41	-	385.8	*	(monoclinic)	[65, 66]

\* Not reported

\*\* Investigated by our group (private communication)

Table 2.2: A list of CDW systems (and possible CDW systems) with the CaBe<sub>2</sub>Ge<sub>2</sub>-type structure.

## 2.4 Physical Properties of UIr<sub>2</sub>Si<sub>2</sub>

### Magnetic properties

UIr<sub>2</sub>Si<sub>2</sub> is known to exhibit an AFM order with the Néel temperature  $T_N$  of 4.9–6 K [47, 67, 68]. In the magnetization process at low temperatures, a metamagnetic transition was reported and the critical field of the AFM order  $\mu_0 H_c$  was estimated about 1.5–2.2 T at the lowest temperatures [47, 67, 68]. The propagation vector of this AFM order has been identified as  $\mathbf{Q} = 0$  based on the previous neutron scattering experiments [69]. The ordered moment is parallel to the  $c$ -axis as in other similar AFM systems, but its magnitude is estimated to be only  $\sim 0.1\mu_B$ , which is particularly small among 122 systems.

### Specific heat and electric resistivity

The temperature dependence of specific heat shows a  $\lambda$ -type anomaly at  $T_N$ . It has a large specific heat (approximately 300 mJ/molK at 2 K), suggesting an increase in the electronic specific heat coefficient. The anomaly associated with the AFM order is gradually suppressed by the magnetic field and shifts to lower temperature. However, a broad peak remains in  $C/T$  even above  $\mu_0 H_c$  up to at least 5 T. The electric resistivity shows a pronounced anisotropy between along the  $c$ -axis and  $a$ -axis. Similar to other 122 systems, the resistivity along the  $c$ -axis exhibits relatively large values below 300 K. The influence of a magnetic field on these characteristics in this system had been largely unexplored so far. Recently, Szlawska *et al.* reported magnetization, specific heat and electric resistivities measured under the magnetic fields and obtained a  $H$ - $T$  phase diagram as shown in Fig. 2.15.



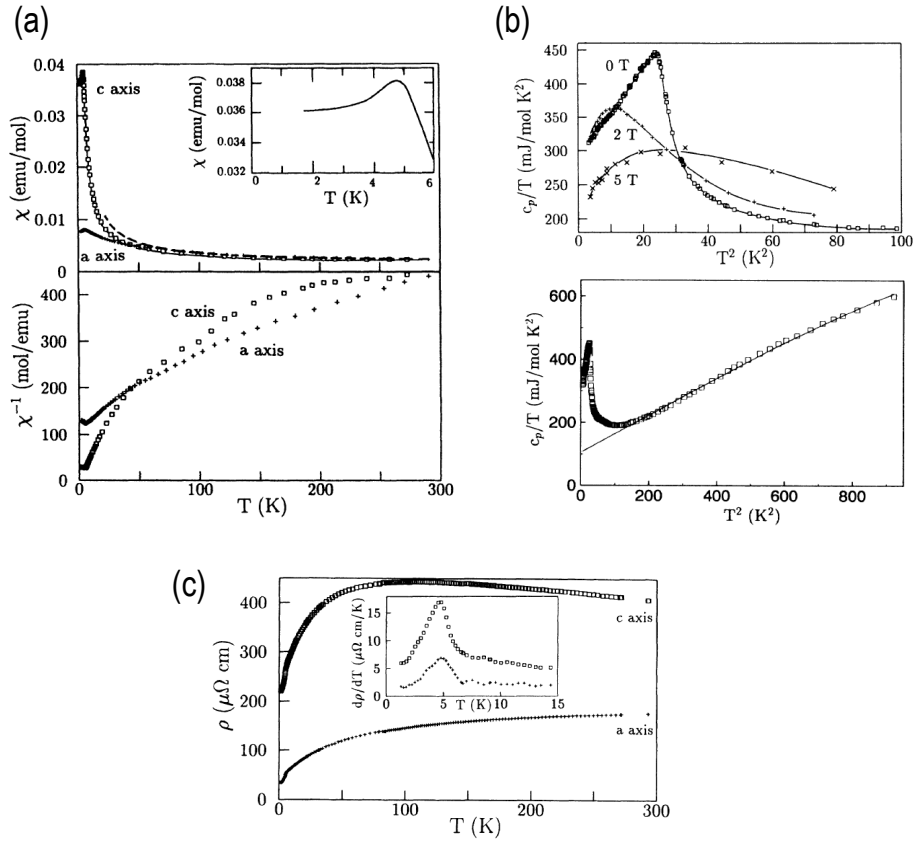


Figure 2.14: The physical properties of  $\text{UIr}_2\text{Si}_2$  reported in the previous study by Dirkmaat *et al.* [47]. The temperature dependences of (a) the magnetic susceptibilities (along the  $a$ - and  $c$ -axes), (b) the specific heat measured under the magnetic field 0–5 T and (c) the electric resistivities (along the  $a$ - and  $c$ -axes).

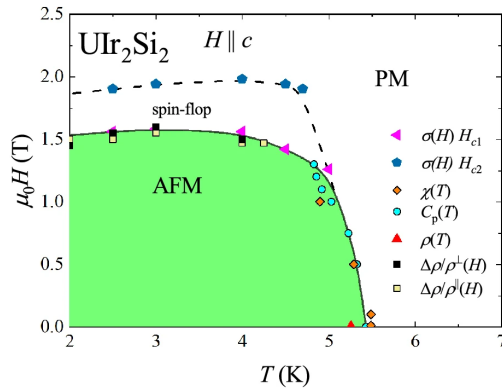


Figure 2.15: The magnetic field phase diagram reported in the previous study by Szlawska *et al.* [68].

# Chapter 3

## Purpose of Study

The present studies were carried out for the primary purpose of investigating the effects of the U-site environment, including the lack of local space inversion symmetry, on the hybridization effects of the 5f electrons. To achieve this purpose, we focused on  $\text{UPt}_2\text{Si}_2$  and  $\text{UIr}_2\text{Si}_2$  with the  $\text{CaBe}_2\text{Ge}_2$ -type structure from the following perspectives.

**UPt<sub>2</sub>Si<sub>2</sub>** Using diffraction techniques allows for the decomposition and extraction of CDW effects based on wave numbers, which in turn offers the potential to obtain microscopic information regarding the correlation between 5f and 5d electrons in this system. The effect of environmental changes at the U site on the 5f electrons was examined by examining the 5f electron state under CDW order in detail. From this viewpoint, two techniques are used in this study. One is resonant X-ray scattering, which allows orbital-selective and symmetry-sensitive investigation of 5f electronic states. However, this method does not provide quantitative information. Hence, another complementary technique, neutron diffraction experiments, was used to identify the magnetic structure of this material, including its quantitativity.

**UIr<sub>2</sub>Si<sub>2</sub>** For the systematic discussion of 5f electronic properties in the  $\text{UT}_2\text{X}_2$  systems, we have investigated the low temperature properties of 5f electrons in  $\text{UIr}_2\text{Si}_2$ , where only few physical properties have been reported. We have constructed the temperature-field phase diagram from the detailed magnetization and specific heat measurements under the magnetic field.

# Chapter 4

## Experimental Methods

### 4.1 Sample preparation

Single crystals of  $\text{UPt}_2\text{Si}_2$  were grown by the Czochralski method from a polycrystal made by arc-melting stoichiometric amounts of U (3N), Pt (3N), and Si (5N) in a pure argon atmosphere using a tetra-arc furnace at Hokkaido University. No additional heat treatment was performed on the samples. The obtained sample was evaluated by laboratory X-ray powder diffraction at the room temperature. All observed peaks were indexed with the  $\text{CaBe}_2\text{Ge}_2$ -type structure, and no impurity phases were detected within the S/N ratio of approximately 0.5%. Lattice constants were obtained as  $a = 4.198(7) \text{ \AA}$  and  $c = 9.69(2) \text{ \AA}$ , consistent with those reported in the previous study [46] within the range of experimental error.

A single-crystalline sample of  $\text{UIr}_2\text{Si}_2$  was prepared at International Research Center for Nuclear Materials Science Institute for Materials Research in Tohoku University by the Czochralski method as for  $\text{UPt}_2\text{Si}_2$ . The starting polycrystal was synthesized by arc-melting stoichiometric amounts of U (3N), Ir (3N) and Si (5N), and the single-crystalline sample was grown from it. No additional heat treatment was performed on the single crystal. Also for the obtained sample of  $\text{UIr}_2\text{Si}_2$ , laboratory X-ray powder diffraction measurement was performed at the room temperature. All observed peaks were indexed with the  $\text{CaBe}_2\text{Ge}_2$ -type structure, and no impurity phases were detected within the S/N ratio less than 1%. Lattice constants were obtained as  $a = 4.084(4) \text{ \AA}$  and  $c = 9.82(1) \text{ \AA}$ . These values are almost consistent with those reported in the previous study [69].

The crystal orientations of the obtained single crystals are identified from the Laue photographs. The samples are cut by an electric discharge machine and shaped into cubes or plates with their crystallographic orientations.

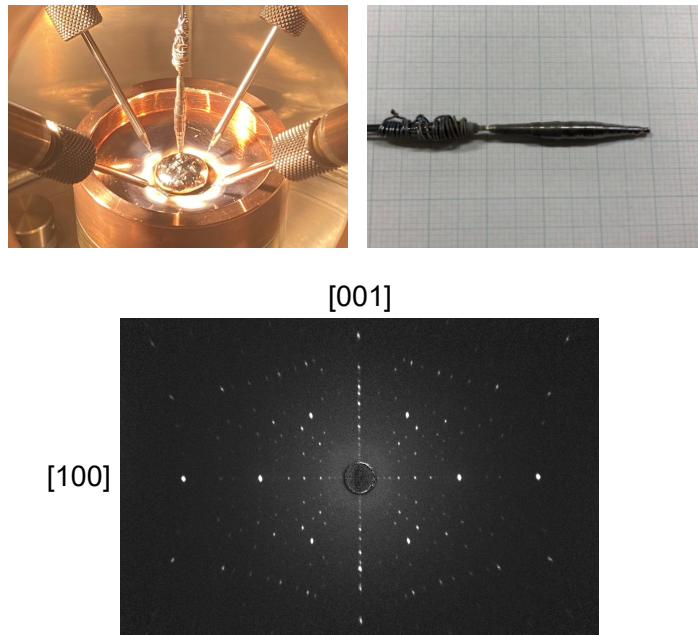


Figure 4.1: (Color online) The view of growing single crystal of  $\text{UPt}_2\text{Si}_2$  (top left), the obtained single-crystalline sample of  $\text{UPt}_2\text{Si}_2$  (top right) and the Laue photograph from  $[010]$  direction.

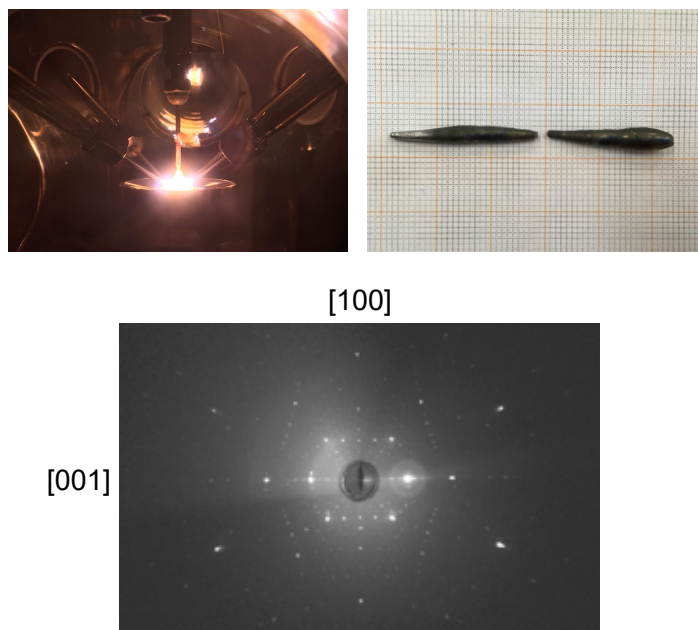


Figure 4.2: (Color online) The view of growing single crystal of  $\text{UIr}_2\text{Si}_2$  (top left), the obtained single-crystalline sample of  $\text{UIr}_2\text{Si}_2$  (top right) and the Laue photograph from  $[010]$  direction.

## 4.2 Resonant X-ray Scattering Experiment

Resonant X-ray scattering is a technique using the energy-variability and the polarizability of synchrotron X-rays. This technique enables element- and orbital-selective investigation of electronic states. The principle of resonant X-ray scattering is briefly introduced below.

### 4.2.1 Principle of resonant X-ray scattering experiment

#### Interaction between electrons and electromagnetic fields

For X-rays, the dominant contribution of scatterings in matter comes from the interaction with the electrons. When electromagnetic waves interact with electrons in a single atom, the Hamiltonian of the entire system is expressed as follows:

$$\begin{aligned} \mathcal{H} = & \sum_i \frac{1}{2m_e} \left( \mathbf{p}_i - \frac{e}{c} \mathbf{A}(\mathbf{r}_i) \right)^2 - \sum_i \frac{Ze^2}{r_i} + \sum_{i,j} \frac{e^2}{|r_i - r_j|} - \frac{e\hbar}{m_e c} \sum_i \mathbf{s}_i \cdot \nabla \times \mathbf{A}(\mathbf{r}_i) \\ & - \frac{e\hbar}{2m_e^2 c^2} \sum_i \mathbf{s}_i \cdot \mathbf{E}(\mathbf{r}_i) \times \left( \mathbf{p}_i - \frac{e}{c} \mathbf{A}(\mathbf{r}_i) \right) + \sum_{\mathbf{k}, \lambda} \hbar \omega_k \left( a_{\mathbf{k}\lambda}^\dagger a_{\mathbf{k}\lambda} + \frac{1}{2} \right). \end{aligned} \quad (4.1)$$

Here  $i$  is the label of each electron. The first term is the kinetic energy of the electron moving in the electromagnetic field, the second term is the potential energy the electron receives from the nucleus, the third term is the Coulomb interaction between the electrons, the fourth term is the magnetic interaction between the spin and the magnetic field, and the fifth term is the spin-orbit interaction, and the sixth term represents the energy of the electromagnetic field.

(4.2) can be summarized using the electromagnetic field potential as follows:

$$\begin{aligned} \mathcal{H} &= \mathcal{H}_0 + \mathcal{H}_R + \mathcal{H}' \\ \mathcal{H}_0 &= \sum_i \frac{p_i^2}{2m_e} - \sum_i \frac{Ze^2}{r_i} + \sum_{i,j} \frac{e^2}{|r_i - r_j|} + \sum_i \xi(\mathbf{r}_i) \hbar^2 \mathbf{s}_i \cdot \mathbf{l}_i \\ \xi(\mathbf{r}) &= \frac{e}{2m_e^2 c^2} \frac{1}{r} \frac{d\phi(\mathbf{r})}{dr} \\ \mathcal{H}_R &= \sum_{\mathbf{k}, \lambda} \hbar \omega_k \left( a_{\mathbf{k}\lambda}^\dagger a_{\mathbf{k}\lambda} + \frac{1}{2} \right) \\ \mathcal{H}' &= \frac{e^2}{2m_e c^2} \sum_i \mathbf{A}(\mathbf{r}_i)^2 - \frac{e^2 \hbar}{2m_e^2 c^4} \sum_i \mathbf{s}_i \cdot \left( \frac{\partial \mathbf{A}}{\partial t} \times \mathbf{A} \right) \\ & \quad - \frac{e}{m_e c} \sum_i \mathbf{A}(\mathbf{r}_i) \cdot \mathbf{p}_i - \frac{e\hbar}{m_e c} \sum_i \mathbf{s}_i \cdot (\nabla \times \mathbf{A}(\mathbf{r}_i)) \\ & \equiv \mathcal{H}'_1 + \mathcal{H}'_2 + \mathcal{H}'_3 + \mathcal{H}'_4. \end{aligned} \quad (4.2)$$

The terms corresponding to the interactions between the electrons and the electromagnetic field are summarized in  $\mathcal{H}'$ , which has been organized into four terms: the

first and second terms for the interaction with the electric charge, and the third and fourth terms for the interaction with the electron spin. The  $\mathcal{H}'$  is a function of the vector potential  $\mathbf{A}$  expressed as in (4.3) using the annihilation and creation operators for photons.  $a_{\mathbf{k}\lambda}^\dagger$  and  $a_{\mathbf{k}\lambda}$  are the creation and annihilation operators of photons with the wavenumber vector  $\mathbf{k}$  and polarization state  $\lambda$  respectively.  $\varepsilon_{k\lambda}$  is the polarization vector of that photon.

$$\mathbf{A} = \sum_{\mathbf{k}, \lambda} \sqrt{\frac{2\pi\hbar c^2}{V\omega_{\mathbf{k}}}} \left( \varepsilon_{k\lambda} a_{\mathbf{k}\lambda} e^{i\mathbf{k}\cdot\mathbf{r}} + \varepsilon_{k\lambda}^* a_{\mathbf{k}\lambda}^\dagger e^{-i\mathbf{k}\cdot\mathbf{r}} \right) \quad (4.3)$$

### X-ray scattering by electrons

Through the electron-electromagnetic field interaction  $\mathcal{H}'$  described above, the entire system of electrons and X-rays transits from the starting state of  $|i\rangle$  to the end state  $|f\rangle$ . In general, the transition probability  $w$  of the transition per unit time is expressed as follows using the intermediate state  $|n\rangle$ :

$$w = \frac{2\pi}{\hbar} \left| \langle f | \mathcal{H}' | i \rangle + \sum_n \frac{\langle f | \mathcal{H}' | n \rangle \langle n | \mathcal{H}' | i \rangle}{E_i - E_n} \right|^2 \delta(E_i - E_f), \quad (4.4)$$

where  $E_i$  ( $E_f$ ) is the energy of the entire system in the starting state (end state). The first and second terms in the equation (4.4) are the first-order and the second-order perturbation terms, respectively.

From here, we will consider the case of elastic scattering, which is the subject of this study, and derive the scattering intensity. In other words, we assume that the final state  $|a'\rangle$  of the electron system is equal to the initial state  $|a\rangle$ . The number of scattered X-ray photons per unit time is equal to the product of  $w$  and the density of states of the final state  $\rho(E_f)$ . Therefore, the scattered X-ray intensity  $I_{rad}$  detected in the angle  $\Delta\Omega$  can be calculated in the following equation.

$$\begin{aligned} I_{rad} &= w\rho(E_f)\Delta\Omega \\ \rho(E_f) &= \frac{V\omega_{k'}^2}{(2\pi)^3\hbar c^3} \end{aligned} \quad (4.5)$$

Then, the scattering cross section is obtained as follows.

$$\frac{d^2\sigma}{d\Omega dE} = \frac{I_{rad}}{\Delta\Omega\Phi_{in}} = \frac{w\rho(E_f)}{\Phi_{in}} \quad (4.6)$$

In our experiments, the scattered X-ray intensity is always normalized by the flux  $\Phi_{in}$  of the incident X-ray. Considering  $\rho(E_f)$  is constant, the transition probability  $w$  is proportional to the scattering cross section.

Here we calculate the differential scattering cross section from the transition probability  $w$  due to the interaction  $\mathcal{H}'$  given by the formula (4.6). The  $\mathbf{A}$  contains the

photon production and annihilation operator, as shown in Eq. (4.3). In the first order terms for  $\mathbf{A}$  in  $\mathcal{H}'$ , the first-order perturbation brings only photon production or annihilation without any scattering, but the second-order perturbation gives scattering through intermediate states. Also, the first-order perturbation term including the second order terms of  $\mathbf{A}$  gives scattering by  $a_{\mathbf{k}\lambda}a_{\mathbf{k}\lambda}^\dagger$ , keeping the electron system invariant. Without going into details (see the article written by Prof. Matsumura [70]), the scattering cross section for the elastic scattering case is obtained by using the scattering amplitude  $|F|$  defined below as follows:

$$\begin{aligned} \frac{d^2\sigma}{d\Omega dE} &\equiv |F|^2 \\ &= |F_c + F_{\text{mag}} + F_{\text{reso}}|^2 \end{aligned} \quad (4.7)$$

The first term is corresponding to non-resonant scattering (Thomson scattering), which is a first-order perturbation of  $\mathcal{H}'_1$ , and the second term is non-resonant magnetic scattering by electron spin, which is a first-order perturbation of  $\mathcal{H}'_2$ . The third term is the second-order perturbation term of  $\mathcal{H}'_3$  and  $\mathcal{H}'_4$ , which is the origin of the scattering known as ‘‘resonant scattering’’. The details of the first and second terms are as follows:

$$\begin{aligned} F_c &= -\frac{e^2}{mc^2} \sum_{\alpha,\beta} \varepsilon'_\alpha{}^* \varepsilon_\beta \langle a' | \sum_j e^{-i\mathbf{k}\cdot\mathbf{r}_j} | a \rangle \delta_{\alpha\beta} \\ &= -\frac{e^2}{mc^2} \langle a' | \sum_j e^{-i\mathbf{k}\cdot\mathbf{r}_j} | a \rangle (\varepsilon'^* \cdot \varepsilon) \\ F_{\text{mag}} &= -\frac{e^2}{mc^2} \sum_{\alpha,\beta} \varepsilon'_\alpha{}^* \varepsilon_\beta \left( -i \frac{\hbar\omega}{mc^2} \right) \langle a' | \sum_j e^{-i\mathbf{k}\cdot\mathbf{r}_j} \left\{ \frac{(\mathbf{p}_j \times \boldsymbol{\kappa})_\gamma}{\hbar\kappa^2} A^{\alpha\beta\gamma} + s_{j\gamma} B^{\alpha\beta\gamma} \right\} | a \rangle \\ &= -\frac{e^2}{mc^2} \left( -i \frac{\hbar\omega}{mc^2} \right) \langle a' | \sum_j e^{-i\mathbf{k}\cdot\mathbf{r}_j} \left\{ \frac{i}{\hbar\kappa^2} (\mathbf{p}_j \times \boldsymbol{\kappa}) \cdot \mathcal{A} + s_j \cdot \mathcal{B} \right\} | a \rangle, \end{aligned} \quad (4.8)$$

where we use  $\mathcal{A}$  and  $\mathcal{B}$  defined as follows:

$$\begin{aligned} \mathcal{A} &= 2 \left( 1 - \hat{k} \cdot \hat{k}' \right) (\varepsilon'^* \times \varepsilon) = 4 \sin^2 \theta (\varepsilon'^* \times \varepsilon) = \frac{\kappa^2}{k^2} (\varepsilon'^* \times \varepsilon) \\ \mathcal{B} &= \left\{ (\varepsilon'^* \times \varepsilon) - (\varepsilon \cdot \hat{k}') (\varepsilon'^* \times \hat{k}') + (\varepsilon'^* \cdot \hat{k}) (\varepsilon \times \hat{k}) - (\hat{k}' \times \varepsilon'^*) \times (\hat{k} \times \varepsilon) \right\}. \end{aligned} \quad (4.9)$$

Here, due to the coefficient  $(-i \frac{\hbar\omega}{mc^2})$  in the scattering amplitude  $F_{\text{mag}}$  of non-resonant magnetic scattering, its intensity is only about  $10^{-6}$  compared to Thomson scattering. It is hardly observed in usual experiments.

The scattering amplitude of resonant scattering is organized as follows:

$$\begin{aligned}
F_{\text{reso}} = & -\frac{e^2}{mc^2} \sum_b \left\{ \frac{m\omega_{ba}^3}{\omega} \frac{\langle a | \sum_{j'} \varepsilon'^* \cdot r_{j'} (1 - \frac{i}{2} k' \cdot r_{j'}) | b \rangle \langle b | \sum_j \varepsilon \cdot r_j (1 + \frac{i}{2} k \cdot r_j) | a \rangle}{\hbar\omega - \hbar\omega_{ba} + i\Gamma_b} \right. \\
& \left. + \frac{\hbar^2 \omega_{ba}}{4m \omega} \frac{\langle a | \sum_{j'} \varepsilon'^* \cdot ((l_{j'} + 2s_{j'}) \times k') | b \rangle \langle b | \sum_j \varepsilon \cdot ((l_j + 2s_j) \times k) | a \rangle}{\hbar\omega - \hbar\omega_{ba} + i\Gamma_b} \right\} \\
= & F_{\text{reso}}^{(E)} + F_{\text{reso}}^{(M)}
\end{aligned} \tag{4.10}$$

The first term corresponds to scattering caused by electrical transitions. The second term corresponds to the scattering caused by magnetic transitions, which is caused by magnetic interactions. The amplitude of magnetic transition, which is also significantly small than that of the electric transition and we do discuss below.

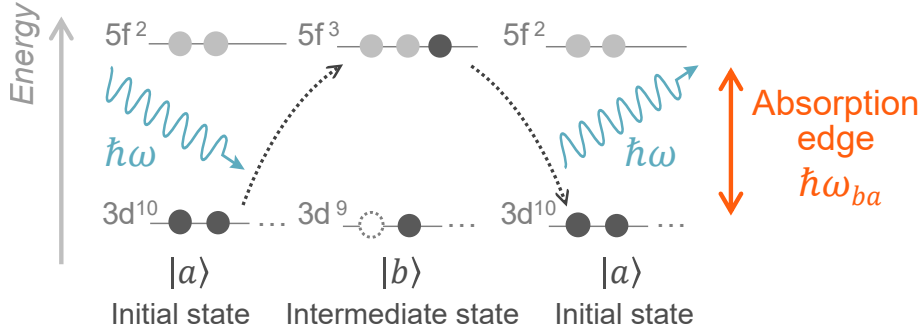


Figure 4.3: (Color online) Transition processes in resonant X-ray scattering.



## 4.2.2 Types of resonance processes

From here, the details of the resonance terms  $F_{\text{reso}}^{(E)}$  (Eq. (4.10)) are described. The atomic scattering factor of resonant X-ray scattering by the electrical transitions, which is the main contribution, can be organized using multipole operators as follows:

$$F_{\text{reso}}^{(E)} = -\frac{e^2}{mc^2} \sum_b \frac{m\omega_{ba}^3}{\omega} \sum_{\alpha,\beta} \varepsilon_{\alpha}^{\prime*} \varepsilon_{\beta} \sum_{\gamma,\delta} \frac{\langle a' | R_{\alpha} - \frac{i}{2} Q_{\alpha\gamma} k'_{\gamma} | b \rangle \langle b | R_{\beta} + \frac{i}{2} Q_{\beta\delta} k_{\delta} | a \rangle}{\hbar\omega - \hbar\omega_{ba} + i\Gamma_b}, \quad (4.11)$$

where  $R_{\alpha}$  corresponds to the electric dipole operator and  $Q_{\alpha\beta}$  ( $\alpha, \beta = x, y, z$ ) to the electric quadrupole operator. Equation (4.11) contains the following two types of transition processes.

$$\begin{aligned} \langle b | R_{\alpha} | a \rangle &= \int \psi_b^* R_{\alpha} \psi_a d\mathbf{r} \\ \langle b | Q_{\alpha\beta} | a \rangle &= \int \psi_b^* Q_{\alpha\beta} \psi_a d\mathbf{r} \end{aligned} \quad (4.12)$$

The electric dipole and the electric quadrupole transitions are called E1 and E2 transitions, respectively. For these integrals to be finite, there are constraints on the change in orbital angular momentum  $\Delta l$  between the states  $|a\rangle$  and  $|b\rangle$  derived from the Wigner-Eckart theorem (see Ref. [71] for example).

$$\text{E1 transition : } \Delta l = \pm 1,$$

$$\text{E2 transition : } \Delta l = 0, \pm 2.$$

In general, resonant X-ray diffractions use E1-E1 (E2-E2) transition, which accompany the E1 process with  $\Delta l = +1$  (E2 process with  $\Delta l = +2$ ) in both of X-ray absorption and emission processes. The atomic scattering factors for resonant X-ray scattering corresponding to these transitions are as follows:

$$\begin{aligned} F_{E1}(\omega) &= -\frac{e^2\omega_0^2}{c^2} \sum_{\alpha,\beta} \varepsilon_{\alpha}^{\prime*} \varepsilon_{\beta} \sum_b \frac{\langle a | R_{\alpha} | b \rangle \langle b | R_{\beta} | a \rangle}{\hbar\omega - \hbar\omega_{ba} + i\Gamma_b} \\ F_{E2}(\omega) &= -\frac{e^2\omega_0^2}{4c^2} \sum_{\alpha,\beta=1}^5 K_{\alpha}(\mathbf{k}', \varepsilon^{\prime*}) K_{\beta}(\mathbf{k}, \varepsilon) \sum_b \frac{\langle a | Q_{\alpha} | b \rangle \langle b | Q_{\beta} | a \rangle}{\hbar\omega - \hbar\omega_{ba} + i\Gamma_b} \end{aligned} \quad (4.13)$$

where  $K_{\mu}$  is defined as follows:

$$\begin{aligned} K_1 &= \frac{1}{2} \{ 3\varepsilon_z k_z - (\varepsilon_x k_x + \varepsilon_y k_y + \varepsilon_z k_z) \}, \\ K_2 &= \frac{\sqrt{3}}{2} (\varepsilon_x k_x - \varepsilon_y k_y), \\ K_3 &= \frac{\sqrt{3}}{2} (\varepsilon_y k_z + \varepsilon_z k_y), \\ K_4 &= \frac{\sqrt{3}}{2} (\varepsilon_z k_x + \varepsilon_x k_z), \\ K_5 &= \frac{\sqrt{3}}{2} (\varepsilon_x k_y + \varepsilon_y k_x). \end{aligned} \quad (4.14)$$

$l$		E1-E1	E1-E2 (elec.)	E1-E2 (mag.)	E2-E2
0	monopole	(+, +)			(+, +)
1	dipole	(+, -)	(-, +)	(-, -)	(+, -)
2	quadrupole	(+, +)	(-, +)	(-, -)	(+, +)
3	octupole		(-, +)	(-, -)	(+, -)
4	hexadecapole				(+, +)

Table 4.1: A list of the observable symmetries of electronic states in each experiment. The couple of signs (++, +-, -+, and --) represents space inversion symmetry and time reversal symmetry ( $\mathcal{P}$ ,  $\mathcal{T}$ ).

The energies listed as absorption edges often refer to this energy, and the values for each element are summarized, for example, in the booklet [72]. Resonance signals are typically observed at the absorption edge, known as the “main edge”, corresponding to the E1-E1 transition. In some cases, signals from the E2-E2 transition can be weakly observed at energies as low as  $\sim 10$  eV below the main edge, referred to as the “pre-edge”. In addition to E1-E1 and E2-E2 transitions, resonant X-ray scatterings can be caused by E1-E2 (E2-E1) transitions, where X-ray is absorbed in the E1(E2) transition and emitted in the E2(E1) transition. In principle, this process is allowed in the presence of parity hybridizations of the outer shell orbitals at the atomic site lacking local inversion symmetry. However, there is little experimental information on resonant X-ray scattering from this E1-E2 transition. The symmetries of the detectable electronic states in these resonant scatterings are listed in Table 4.1.

### 4.2.3 Detection of multipoles by resonant x-ray scattering

When multipole ordering occurs in a crystal, it can be detected as diffraction peaks of resonant X-ray scattering. So far we have considered scattering from a single atom. In the following part, we will consider diffractions from crystals. We redefine the scattering amplitude  $F$  as the atomic scattering factor  $F_{\text{reso},j}$  for site  $j$  as follows:  $F = F_{\text{reso},j}$ , where  $F$  is the scattering amplitude of site  $j$  in Eq. (4.11) as follows:

$$F_{\text{reso}}(\omega) = \sum_j F_{\text{reso},j}(\omega) e^{-i\boldsymbol{\kappa} \cdot \mathbf{r}_j}. \quad (4.15)$$

To calculate the atomic scattering factor in Eq. (4.15), we use the Nagao and Igarashi’s method[73], which is the main method for f-electron systems. The atomic scattering factors for resonant scattering by E1-E1 and E2-E2 transitions are obtained as follows:

$$\begin{aligned} F_{E1}(\omega) &= \sum_{\nu=0}^2 \alpha_{E1}^{(\nu)}(\omega) \sum_{\mu=1}^{2\nu+1} P_{E1,\mu}^{(\nu)}(\varepsilon, \varepsilon'^*) Z_{\mu}^{(\nu)}, \\ F_{E2}(\omega) &= \sum_{\nu=0}^4 \alpha_{E2}^{(\nu)}(\omega) \sum_{\mu=1}^{2\nu+1} P_{E2,\mu}^{(\nu)}(\varepsilon, \varepsilon'^*, k, k') Z_{\mu}^{(\nu)}. \end{aligned} \quad (4.16)$$

This is the result of summing  $|b\rangle$  in Eq. (3.17) based on the assumption that the Hamiltonian describing the intermediate state preserves rotational symmetry, which

is considered a good approximation for strongly localized systems such as  $f$  electron systems. Although this approximation does not allow analysis of the absolute value of the scattering intensity, it is a widely used method because it allows us to discuss the symmetry of the electronic state in terms of polarization dependence, for example. Here,  $Z_\mu^{(\nu)}$  is a multipole structure factor defined as

$$\sum_j \langle z_\mu^{(\nu)} \rangle_j e^{-i\mathbf{k} \cdot \mathbf{r}_j}. \quad (4.17)$$

$z_\mu^{(\nu)}$  is the multipole operator of rank- $\nu$  and  $\mu$  is the component (for example,  $\mu = x, y, z$  for  $\nu = 1$ ) of multipoles.  $P_{E1,\mu}^{(\nu)}$  and  $P_{E2,\mu}^{(\nu)}$  are geometric structure factors of E1-E1 and E2-E2 transitions for  $z_\mu^{(\nu)}$ . In the case of E1-E1 transition, they are obtained as follows:

$$\begin{aligned} P_{E1,1}^{(0)} &= (\boldsymbol{\varepsilon}'^* \cdot \boldsymbol{\varepsilon}), \\ P_{E1,\mu}^{(1)} &= -i (\boldsymbol{\varepsilon}'^* \times \boldsymbol{\varepsilon})_\mu, \\ P_{E1,\mu}^{(2)} &= K_\mu (\boldsymbol{\varepsilon}'^*, \boldsymbol{\varepsilon}). \end{aligned} \quad (4.18)$$

They are also calculated for the case of E2-E2 transition.

The coupling between  $P$  and  $Z$  in Eq. (4.16) means that the change in polarization of X-rays before and after scattering reflects the symmetry of the ordering multipole. In other words, the symmetry of  $Z^{(\nu)}$  can be identified by analyzing the polarization state of the scattered X-rays with the polarized incident X-ray. Furthermore, as shown in 4.4, its symmetry can be investigated in more detail by measuring the change in the scattering intensity with rotating the sample around the scattering vector. This rotational angle is defined as the azimuthal angle  $\varphi$ . The present analyses are based on the method described in the textbook written by Prof. Matsumura [70]. The following is a brief summary of the analyses.

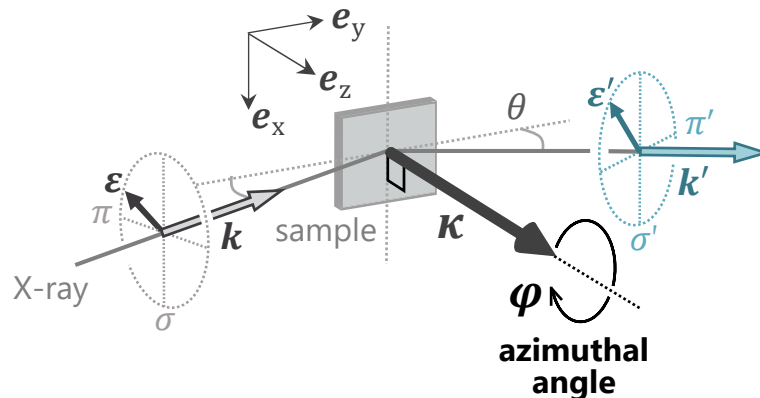


Figure 4.4: (Color online) The relationship between the scattering plane, polarization, and azimuth angle. Here we introduce a coordinate system  $xyz$ . The  $x$ -axis is perpendicular to the scattering plane and the  $z$  direction is defined as the direction of the scattering vector  $\boldsymbol{\kappa}$ .

The setting in our measurements is shown in Fig. 4.4. In this geometry, the wave vectors and polarization vectors in the  $xyz$  coordinate system are obtained as follows.

$$\begin{aligned} \mathbf{k} &= k(0, \cos \theta, -\sin \theta), & \mathbf{k}' &= k(0, \cos \theta, \sin \theta), \\ \boldsymbol{\varepsilon}_\sigma &= (1, 0, 0), & \boldsymbol{\varepsilon}'_\sigma &= (1, 0, 0), \\ \boldsymbol{\varepsilon}_\pi &= (0, -\sin \theta, -\cos \theta), & \boldsymbol{\varepsilon}'_\pi &= (0, \sin \theta, -\cos \theta) \end{aligned} \quad (4.19)$$

When the sample is rotated by azimuth angle  $\varphi$ , these vectors are considered to be rotated by  $-\varphi$  with respect to the sample. The resulting rotated vectors are obtained in the fixed  $xyz$  coordinate system as follows.

$$\begin{aligned} \boldsymbol{\varepsilon}_\sigma &= (\cos \varphi, -\sin \varphi, 0), & \boldsymbol{\varepsilon}'_\sigma &= (\cos \varphi, -\sin \varphi, 0), \\ \boldsymbol{\varepsilon}_\pi &= (-\sin \varphi \sin \theta, -\cos \varphi \sin \theta, \cos \theta), & \boldsymbol{\varepsilon}'_\pi &= (\sin \varphi \sin \theta, \cos \varphi \sin \theta, \cos \theta). \end{aligned} \quad (4.20)$$

The azimuth angle dependence of the scattering amplitude is obtained by substituting these polarization vectors into the geometric factor  $P$  for each type of scattering.

For the calculation of the azimuth angle dependence of the scattering intensity at a certain fixed energy or the polarization state of the scattered X-rays, it is convenient to discuss the scattering amplitude  $G$ , excluding the energy spectrum. For example, the scattering amplitude  $F$  of the E1-E1 transition (eq. (4.16)) can be rewritten using  $G$  as follows.

$$F_{E1}(\omega) = \sum_{\nu=0}^2 \alpha_{E1}^{(\nu)}(\omega) G_{E1}^{(\nu)}(\boldsymbol{\varepsilon}, \boldsymbol{\varepsilon}'^*). \quad (4.21)$$

Here, we introduce the scattering amplitude operator  $\hat{G}$ , defined as a  $2 \times 2$  matrix with elements of scattering amplitudes for the four scattering processes:  $\sigma$ - $\sigma'$ ,  $\sigma$ - $\pi'$ ,  $\pi$ - $\sigma'$ , and  $\pi$ - $\pi'$  scattering.

$$\hat{G} = \begin{pmatrix} G^{\sigma\sigma'} & G^{\pi\sigma'} \\ G^{\sigma\pi'} & G^{\pi\pi'} \end{pmatrix}. \quad (4.22)$$

Representing the polarization state of the incident X-ray by the Stokes parameter  $\mathbf{P}$ , the scattering cross section is obtained as follows.

$$\left( \frac{d\sigma}{d\Omega} \right) = \text{Tr} \left\{ \hat{\mu} \hat{G}^\dagger \hat{G} \right\}, \quad (4.23)$$

where  $\hat{\mu}$  is a matrix expressed as  $\hat{\mu} = \frac{1}{2}(\hat{I} + \mathbf{P} \cdot \hat{\boldsymbol{\sigma}})$  using the identity matrix  $\hat{I}$  and the Pauli matrix  $\hat{\boldsymbol{\sigma}}$ . When scattered X-rays are detected through a polarization analyzer, the intensity observed at the detector can be obtained using the cross section of X-ray scattering at the sample  $\left( \frac{d\sigma}{d\Omega} \right)$ .

$$\begin{aligned} I &= K \left( \frac{d\sigma}{d\Omega} \right) \left\{ 1 - \frac{1}{2} (1 - P_{3A}) \sin^2 2\theta_A \right\}, \\ P_{3A} &= -P'_1 \sin 2\phi_A + P'_3 \cos 2\phi_A. \end{aligned} \quad (4.24)$$

$\phi_A$  is the angle between the scattering planes of the sample and the analyzer (see Fig. 5.2 in Chapter 5). The scattering angle of the analyzer is denoted as  $2\theta_A$  and it

should be  $90^\circ$ , ideally.  $\mathbf{P}'$  is the Stokes parameter for scattered X-rays and has the following relationship with the scattering amplitude.

$$\left(\frac{d\sigma}{d\Omega}\right) \mathbf{P}' = \text{Tr} \left\{ \hat{\mu} \hat{G}^\dagger \hat{\boldsymbol{\sigma}} \hat{G} \right\}. \quad (4.25)$$

Namely,  $\mathbf{P}'$  can be obtained by dividing  $\left(\frac{d\sigma}{d\Omega}\right) \mathbf{P}'$  by  $\left(\frac{d\sigma}{d\Omega}\right)$ . By substituting the obtained  $\mathbf{P}'$  into eq. (4.24), the  $\varphi$ - and  $\phi_A$ -dependences of the scattering intensity were calculated and compared with the experimental results.

## 4.3 Neutron Scattering Experiment

Neutron scattering experiments can analyze periodic structures such as crystalline structures and magnetic structures through the interaction of neutrons with nuclei and spins. Quantitative analysis of magnetic structure is possible by measuring relative intensity of magnetic scattering to nuclear scattering. In this sense, it is a complementary technique to magnetic structure analysis using resonant X-ray scattering. Furthermore, the use of spin-polarized neutrons allows for more detailed analysis. In this chapter, we briefly describe unpolarized (4.3.1) and polarized (4.3.2) neutron scattering experiments.

### 4.3.1 Unpolarized neutron diffraction measurement

In general, the diffraction intensity observed in the scattering vector  $\boldsymbol{\kappa}$  is expressed by the following equation using the scattering cross section  $\left(\frac{d\sigma}{d\Omega}\right)$ .

$$I(\boldsymbol{\kappa}) = KL(\boldsymbol{\kappa}) \left(\frac{d\sigma}{d\Omega}\right), \quad (4.26)$$

where  $K$  is a factor that depends on the experimental conditions, such as incident neutron intensity and equipment, and is a common quantity within an experiment conducted under the same conditions.  $L(\boldsymbol{\kappa})$  is a Lorentz factor. The magnetic structure, including the absolute value of the magnetic moment, can be determined by analyzing the absolute value of the magnetic scattering intensity using  $K$  evaluated from the nuclear scattering intensity.

#### ***Nuclear scattering***

Nuclear scattering is caused by the nuclear force between neutrons and nuclei in matter. The effective potential of interaction at the neutron position  $\mathbf{r}$  is introduced as  $V_N$  (Fermi pseudopotential) using the position of the  $j$ -th nucleus  $\mathbf{R}_j$ .

$$V_N(\mathbf{r}_j) = \frac{2\pi\hbar^2}{m_N} b_j \delta(\mathbf{r}_j). \quad (4.27)$$

The Fourier transform of this potential is calculated as follows:

$$\frac{m_N}{2\pi\hbar^2} V_N(\boldsymbol{\kappa}) = \sum_j b_j \exp(i\mathbf{Q} \cdot \boldsymbol{\kappa}). \quad (4.28)$$

Using this, the scattering cross section is obtained as follows:

$$\left(\frac{d\sigma}{d\Omega}\right)_{\text{coh}}^{\text{el}} = N \frac{(2\pi)^3}{v_0} \sum_{\mathbf{G}} |F_N(\boldsymbol{\kappa})|^2 \delta(\boldsymbol{\kappa} - \mathbf{G}). \quad (4.29)$$

$\mathbf{G}$  is the reciprocal lattice point where the fundamental lattice reflection is observed. The scattering amplitude per unit cell of the nucleus is introduced as

$$F_N(\boldsymbol{\kappa}) = \sum_d \bar{b}_d \exp(-W_d) \exp(i\boldsymbol{\kappa} \cdot \mathbf{d}), \quad (4.30)$$

where  $\mathbf{d}$  is the atomic positions in the nuclear unit cell. The  $\bar{b}$  is the nuclear scattering length, a quantity unique to each atom. The values summarized in this paper [74] are used in this analysis.  $N$  is the number of nuclear unit cells in the sample and  $v_0$  is the volume of nuclear unit cell. The  $W$  is a factor due to thermal fluctuations of the atomic positions (Debye-Waller factor), but since all the experiments are performed in the low temperature region below 50 K, all the analyses are performed with  $W = 0$ .  $F_N(\boldsymbol{\kappa})$  becomes 0 at  $\boldsymbol{\kappa} = \boldsymbol{\tau}$  where  $\boldsymbol{\tau} = (h, k, 0)$  with  $h + k = \text{odd}$ .

### ***Magnetic scattering***

Magnetic scattering of neutrons is caused by the dipole interaction between the neutron spin and the magnetic moment in the sample. The interaction potential and its Fourier transform are obtained as follows:

$$\begin{aligned} V_M(\mathbf{r}) &= -\boldsymbol{\mu}_N \cdot \mathbf{B}(\mathbf{r}), \\ \left(\frac{2\pi\hbar^2}{m_N}\right) V_m(\boldsymbol{\kappa}) &= \frac{\gamma r_0}{\mu_B} \boldsymbol{\sigma} \cdot \mathbf{M}_\perp(\boldsymbol{\kappa}). \end{aligned} \quad (4.31)$$

Here,  $\mathbf{M}_\perp(\boldsymbol{\kappa})$  refers to the projection of  $\mathbf{M}(\boldsymbol{\kappa})$  onto the plane perpendicular to  $\boldsymbol{\kappa}$ , defined as  $\mathbf{M}_\perp(\boldsymbol{\kappa}) \equiv \boldsymbol{\kappa} \times \mathbf{M}(\boldsymbol{\kappa}) \times \boldsymbol{\kappa}$ .  $\mathbf{M}(\boldsymbol{\kappa})$  is the component of the Fourier-transformed magnetic-moment distributions with respect to  $\boldsymbol{\kappa}$ .

The scattering cross section at the scattering vector  $\boldsymbol{\kappa}$  is obtained using  $\mathbf{M}_\perp(\boldsymbol{\kappa})$  as follows.

$$\begin{aligned} \left(\frac{d\sigma}{d\Omega}\right)_{\text{coh}}^{\text{el}} &= \mathbf{M}_\perp^*(\boldsymbol{\kappa}) \mathbf{M}_\perp(\boldsymbol{\kappa}), \\ \mathbf{M}_\perp(\boldsymbol{\kappa}) &\equiv \sum_{\mathbf{l}, \mathbf{d}} (-2.7 \boldsymbol{\mu}_\perp(\mathbf{l}, \mathbf{d}) f_d(\boldsymbol{\kappa}) \exp(i\boldsymbol{\kappa} \cdot (\mathbf{l} + \mathbf{d}))), \end{aligned} \quad (4.32)$$

where  $\mathbf{l}$  is the position of the nuclear unit cell.  $\boldsymbol{\mu}_\perp(\mathbf{l}, \mathbf{d})$  is the projection of the ordered moment at  $\mathbf{l} + \mathbf{d}$ .  $\mathbf{M}_\perp(\boldsymbol{\kappa})$  includes the factor of  $-2.7$ , which is the magnetic scattering length per Bohr magneton. The further calculations depend on the assumed magnetic structure, but in general, as in the case of nuclear scattering, the magnetic structure factor  $|F_m(\boldsymbol{\kappa})|$  per nuclear unit cell can be defined. The subsequent calculations depend on the type of magnetic structure, but in general, one can define a magnetic structure factor  $|F_m(\boldsymbol{\kappa})|$  per nuclear unit cell, as in the case of nuclear scattering. However, in the case of a commensurate structure, magnetic unit cells can be defined to simplify calculations. Hereafter, we calculate the magnetic structure factors for the commensurate and incommensurate structures, respectively.

#### **(i) Commensurate order**

Assuming the magnetic unit cell is  $X$  times larger than the nuclear one ( $X$ : an integer), its magnetic structure factor can be calculated in the same way as nuclear scattering. In such cases,  $\boldsymbol{\mu}_\perp(\mathbf{l}, \mathbf{d})$  can be simplified to  $\boldsymbol{\mu}_\perp(\mathbf{d}')$  using  $\mathbf{l}'$  and  $\mathbf{d}'$  for the magnetic unit cells instead of  $\mathbf{l}$  and  $\mathbf{d}$ . The magnetic structure factor for the magnetic unit cell

is as follow.

$$\begin{aligned}\frac{d\sigma}{d\Omega} &= N_m \frac{(2\pi)^3}{v_{m0}} |F_m(\boldsymbol{\kappa})|^2 \delta(\boldsymbol{\kappa} - \mathbf{G}_m), \\ |F_m(\boldsymbol{\kappa})| &\equiv (2.7) \left| \sum_{\mathbf{d}}' \boldsymbol{\mu}_{\perp}(\mathbf{d}') f_{\mathbf{d}'}(\boldsymbol{\kappa}) \exp(i\boldsymbol{\kappa} \cdot \mathbf{d}') \right|.\end{aligned}\quad (4.33)$$

$\mathbf{G}_m$  is the reciprocal lattice vector defined on the bases of the translational symmetry of the magnetic unit cell. In this equation,  $N_m (= N/X)$  represents the number of magnetic unit cells in the system, and  $v_{m0} (= Xv_0)$  is the volume of a magnetic unit cell. The obtained structure factor is further transformed to use the same scale factor as nuclear scattering as follow.

$$\frac{d\sigma}{d\Omega} = N \frac{(2\pi)^3}{v_0} \left| \frac{F_m(\boldsymbol{\kappa})}{X} \right|^2 \delta(\boldsymbol{\kappa} - \mathbf{G}_m) \quad (4.34)$$

Here, we assume the AFM order of  $\mathbf{Q} = 0$  in  $\text{UPt}_2\text{Si}_2$  for the calculation. In this case, two U ions in the nuclear unit cell have magnetic moments antiparallel to each other:  $\boldsymbol{\mu}_{\perp}(\mathbf{d}) = \boldsymbol{\mu}_{\perp}$  (for U ion 1) and  $-\boldsymbol{\mu}_{\perp}$  (for U ion 2). Consequently, the cross section for this specific magnetic structure is determined as

$$\begin{aligned}\frac{d\sigma}{d\Omega} &= N \frac{(2\pi)^3}{v_0} |F_m(\boldsymbol{\kappa})|^2 \delta(\boldsymbol{\kappa} - \mathbf{G}_m), \\ |F_m(\boldsymbol{\kappa})| &\equiv (2.7) |\boldsymbol{\mu}_{\perp}| f_{\text{U}}(\boldsymbol{\kappa}) A(\boldsymbol{\kappa}).\end{aligned}\quad (4.35)$$

The phase factor  $A(\boldsymbol{\kappa})$  for this structure is as follow.

$$A(\boldsymbol{\kappa}) = \left| \sum_{\mathbf{d}} \left( \frac{\boldsymbol{\mu}_{\perp}(\mathbf{d})}{|\boldsymbol{\mu}_{\perp}|} \right) \exp(i\boldsymbol{\kappa} \cdot \mathbf{d}) \right|. \quad (4.36)$$

It would be 2 for  $\boldsymbol{\kappa} = \boldsymbol{\tau}$  and 0 elsewhere.

### (ii) Incommensurate order

As an example, the calculation for the case of a sinusoidal magnetic modulation in the  $c$ -plane with a propagation vector of  $\mathbf{q}$  is presented below. The magnetic distribution  $\boldsymbol{\mu}$  is described as follow.

$$\boldsymbol{\mu}_{\perp}(\mathbf{l}, \mathbf{d}) = \delta \boldsymbol{\mu}_{\perp} \sin(\mathbf{q} \cdot (\mathbf{l} + \mathbf{d})). \quad (4.37)$$

The scattering cross section for this modulation is given as

$$\begin{aligned}\frac{d\sigma}{d\Omega} &= N \frac{(2\pi)^3}{v_0} \{ |F_m^+(\boldsymbol{\kappa})|^2 \delta(\boldsymbol{\kappa} - \mathbf{q} - \mathbf{G}) \\ &\quad + |F_m^-(\boldsymbol{\kappa})|^2 \delta(\boldsymbol{\kappa} + \mathbf{q} - \mathbf{G}) \},\end{aligned}\quad (4.38)$$

where  $\mathbf{G}$  represents the reciprocal lattice vector, and  $F_m^{\pm}$  denotes the magnetic structure factor corresponding to the superlattice reflection at  $\mathbf{G} \pm \mathbf{q}$ , which is calculated



as

$$|F_{m'}^{\pm}(\boldsymbol{\kappa})| \equiv b_{mag} \frac{|\delta\boldsymbol{\mu}_{\perp}|}{2} f_U(\boldsymbol{\kappa}) A^{\pm}(\boldsymbol{\kappa}),$$

$$A^{\pm}(\boldsymbol{\kappa}) = \left| \sum_{\mathbf{d}} \exp(i(\boldsymbol{\kappa} \mp \mathbf{q}) \cdot \mathbf{d}) \right|. \quad (4.39)$$

In this case, the phase factor  $A^{\pm}(\boldsymbol{\kappa})$  becomes 2 at  $\boldsymbol{\kappa} = \mathbf{G} \pm \mathbf{q}$  except for the case of  $\mathbf{G} = \boldsymbol{\tau}$  and 0 elsewhere. The magnetic structure factors incorporate the factor of  $N \frac{(2\pi)^3}{v_0}$ , which is also present in the nuclear structure factor.

### 4.3.2 Polarized neutron diffraction measurement

As seen in Eq. (4.28) and (4.31), nuclear scattering is independent of the neutron spin, whereas magnetic scattering is dependent on the spin state of the neutron. Using spin-polarized neutrons, detailed information of the scatterer in the sample can be obtained by analyzing the spin state of the scattered neutrons. Here, we introduce the method called ‘‘uniaxial polarization analysis’’ and briefly explain its principle. In uniaxial polarization analysis, the spin of the incident neutron is polarized in a certain direction, and the polarization of the scattered neutron is analyzed only in that direction. Namely, spin-flip (SF) signals, in which the spin state of the incident neutron is inverted by the scattering, and non-spin-flip (NSF) signals, in which the spin state remains unchanged, are detected separately. In the following, the relationships between the SF/NSF signals and their respective scatterers are explained for two settings.

#### (i) $P_{zz}$ setting

In this setting, the spin of the incident neutron is polarized in the direction perpendicular to the scattering plane ( $z$  direction in the Fig. 4.5). In the case of nuclear scattering, the spin state does not change. Thus all of nuclear scattering contributions are observed as the NSF signal. In magnetic scattering, on the other hand, the incident (scattered) neutron spin state is  $s$  ( $s'$ ), and the scattered intensity is as follows:

$$I \propto |\langle s, k | V_m | s', k \rangle|^2 \propto |\langle s | \boldsymbol{\sigma} \cdot \mathbf{M}_{\perp}(\boldsymbol{\kappa}) | s' \rangle|^2. \quad (4.40)$$

Separating the NSF and SF signals, the respective scattering intensities are obtained as follows:

$$\begin{aligned} I_{\uparrow\uparrow} &\propto |\langle \uparrow | \boldsymbol{\sigma} \cdot \mathbf{M}_{\perp}(\boldsymbol{\kappa}) | \uparrow \rangle|^2 \\ &= |\langle \uparrow | \sigma_y M_{\perp y}(\boldsymbol{\kappa}) + \sigma_z M_{\perp z}(\boldsymbol{\kappa}) | \uparrow \rangle|^2 = |\langle M_{\perp z}(\boldsymbol{\kappa}) \rangle|^2 \quad (\text{NSF}), \\ I_{\uparrow\downarrow} &\propto |\langle \uparrow | \boldsymbol{\sigma} \cdot \mathbf{M}_{\perp}(\boldsymbol{\kappa}) | \downarrow \rangle|^2 \\ &= |\langle \uparrow | \sigma_y M_{\perp y}(\boldsymbol{\kappa}) + \sigma_z M_{\perp z}(\boldsymbol{\kappa}) | \uparrow \rangle|^2 = |\langle M_{\perp y}(\boldsymbol{\kappa}) \rangle|^2 \quad (\text{SF}). \end{aligned} \quad (4.41)$$

This means that the scattering by the component  $M_{\perp z}(\boldsymbol{\kappa})$  perpendicular to the scattering plane is observed as NSF signal and the scattering by the component  $M_{\perp y}(\boldsymbol{\kappa})$  within the scattering plane is observed as SF signal.

(ii)  $P_{xx}$  setting

In this setting, the spin of the incident neutron is polarized in the direction parallel to the scattering vector  $\boldsymbol{\kappa}$  ( $x$  direction in the Fig. 4.5). All of nuclear scattering contributions are observed as the NSF signal as in  $P_{zz}$  setting. The magnetic scattering intensities of the NSF and SF signals are obtained in the same way for  $P_{zz}$  setting.

$$\begin{aligned}
 I_{\uparrow\uparrow} &\propto |\langle \uparrow | \boldsymbol{\sigma} \cdot \mathbf{M}_{\perp}(\boldsymbol{\kappa}) | \uparrow \rangle|^2 \\
 &= |\langle \uparrow | \sigma'_y M_{\perp y}(\boldsymbol{\kappa}) + \sigma'_z M_{\perp z}(\boldsymbol{\kappa}) | \uparrow \rangle|^2 = 0 && \text{(NSF),} \\
 I_{\uparrow\downarrow} &\propto |\langle \uparrow | \boldsymbol{\sigma} \cdot \mathbf{M}_{\perp}(\boldsymbol{\kappa}) | \downarrow \rangle|^2 \\
 &= |\langle \uparrow | \sigma'_y M_{\perp y}(\boldsymbol{\kappa}) + \sigma'_z M_{\perp z}(\boldsymbol{\kappa}) | \uparrow \rangle|^2 = |\langle M_{\perp y}(\boldsymbol{\kappa}) \rangle|^2 + |\langle M_{\perp z}(\boldsymbol{\kappa}) \rangle|^2 && \text{(SF).}
 \end{aligned} \tag{4.42}$$

Note that, in this setting, the direction of the neutron spin quantization axis corresponds to the  $x$  axis direction. In this case, all the magnetic contributions are observed as SF scatterings and only the nuclear contribution is observed as NSF scattering.

The relationship between the SF/NSF signal and the corresponding scatterers in the  $P_{zz}$  and  $P_{xx}$  settings obtained from the above calculations are summarized in the table 6.1. Together, the results obtained in these two setting patterns allow us to distinguish three different signals: nuclear scattering, magnetic scattering from  $M_y$ , and magnetic scattering from  $M_z$ .

	$P_{xx}$	$P_{zz}$
SF	$M_{\perp y}, M_{\perp z}$	$M_{\perp y}$
NSF	nuclear	nuclear, $M_{\perp z}$

Table 4.2: The relationship between signal types and their origins in polarized neutron diffraction measurements with  $P_{xx}$  or  $P_{zz}$  setting. Non-spin-flip (NSF) scattering refers to the case where the spin of the scattered neutron does not invert from the incident neutron spin state, while spin-flip (SF) scattering refers to the case where the spin of the scattered neutron inverts from the incident neutron spin state.  $M_{\perp z}$  denotes the component of the magnetic moment that is perpendicular to the scattering plane, while  $M_{\perp y}$  denotes the in-plane component, which is perpendicular to  $\boldsymbol{\kappa}$ .

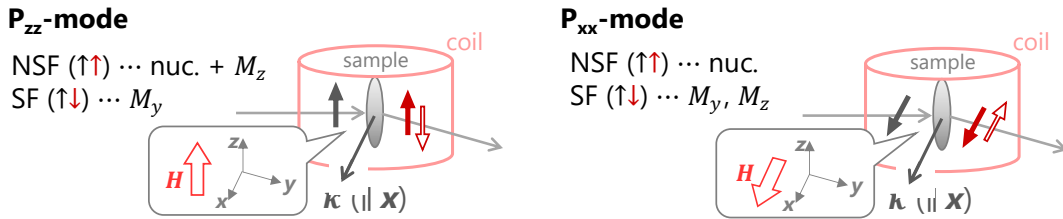


Figure 4.5: (Color online) The geometric configurations in the  $P_{zz}$  and  $P_{xx}$  settings.

## 4.4 Magnetization and Specific heat measurements

For magnetization measurements of  $\text{UIr}_2\text{Si}_2$ , we used SQUID magnetometers of MPMS-2 MPMS-3 manufactured by Quantum Design Inc. The data were obtained in the temperature range from 2 K to 300 K under the magnetic field of 0.1-7 T.

Specific heat of  $\text{UIr}_2\text{Si}_2$  was measured using a thermal relaxation technique by a PPMS, also manufactured by Quantum Design Inc. The measurements were performed in the temperature range from 2 to 60 K under the magnetic fields up to 12 T. The applied fields were parallel to the  $c$ -axis.

# Chapter 5

## Resonant X-ray Scattering Experiments on $\text{UPt}_2\text{Si}_2$

### 5.1 Experimental Procedure

We performed the RXS experiments at BL-11B of KEK Photon Factory on single-crystalline samples of  $\text{UPt}_2\text{Si}_2$  using an in-vacuum two-circle diffractometer [75] (Fig. 5.1). The crystal was shaped into two rectangular parallelepipeds of  $\sim 1 \times 3 \times 3 \text{ mm}^3$  with polished wide planes of (100) and (001) for the measurements in the scattering plane of  $(hk0)$  and  $(h0l)$ , respectively. The measurements were performed in temperature range of 6–300 K by using  $^4\text{He}$ -flow cryostat. The incident beams were monochromatized with Si (111) double crystals and tuned around the energy of 3.72 keV ( $U$   $M_4$ -edge:  $3d_{3/2} \leftrightarrow 5f$  dipole ( $E1$ ) transition).

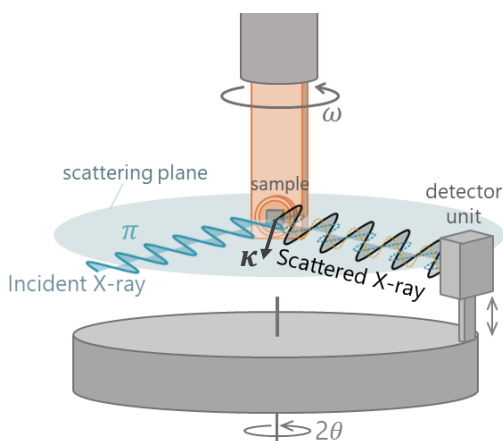


Figure 5.1: (Color online) The schematic view of an in-vacuum two-circle diffractometer.

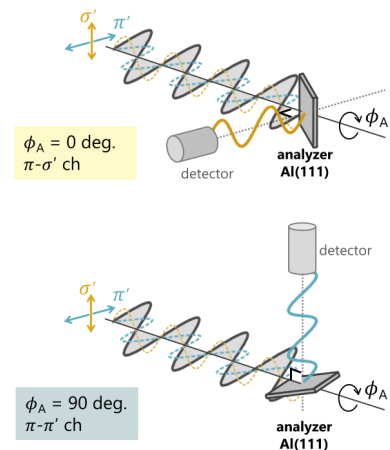


Figure 5.2: (Color online) The schematic view of a polarization analyzer at  $\phi_A = 0$  (upper) and  $90^\circ$  (lower).

The polarization of the incident beam  $\varepsilon$  is  $\pi$  (linearly polarized within the scattering

plane). We performed polarization analyses for the scattered X-ray in the configuration shown in the Fig. 5.2 using Al [111] analyzer ( $d = 2.338 \text{ \AA}$ ,  $2\theta_A = 90.8^\circ$  at  $E = 3.722 \text{ keV}$ ). The polarization of the scattered X-ray  $\boldsymbol{\varepsilon}'$  can be analyzed by rotating the polarizer scattering plane by angle  $\Phi_A$ ; the detectable polarization component of the scattered beam is switched  $\sigma'$  to  $\pi'$  by rotating  $\Phi_A$  from  $0$  to  $90^\circ$ .

## 5.2 Results

### 5.2.1 $Q = 0$ magnetic reflections

Firstly, we searched the magnetic reflections with  $Q = 0$ , which have been reported in previous neutron scattering studies [44, 46], at  $\sim 10 \text{ K}$  using the resonant energy without a polarization analyzer. In the AFM phase, we observed a series of reflections  $(h, k, 0)$  ( $h+k = \text{odd}$ ), which are forbidden positions for this crystal structure with the space group  $P4/nmm$ . The peak profile for one of those reflections,  $(1, 0, 0)$ , is shown in Fig. 5.3 (a). As shown in Fig. 5.3 (c), the energy dependence of this reflection intensity shows a clear resonant spectrum with a peak at  $3.722 \text{ keV}$ . This energy corresponds to the U  $M_4$  absorption edge, as checked in the fluorescence spectrum of  $\text{UPt}_2\text{Si}_2$  (Fig. 5.3 (b)). This result indicates the existence of order by U  $5f$  electrons, which breaks the  $n$ -glide symmetry of the crystal structure. We then performed a polarization analysis on the  $(1, 0, 0)$  reflection intensity at  $10 \text{ K}$ . The results are shown in Fig. 5.4. The scattering intensity clearly shows a behavior with a minimum value of almost zero in the  $\sigma'$  channel ( $\Phi_A = 0$ ) and a maximum in the  $\pi'$  channel ( $\Phi_A = 90^\circ$ ). The observed  $\Phi_A$  dependence is well reproduced by calculations using scattering amplitudes of  $F^{\pi\pi'} \neq 0$  and  $F^{\pi\sigma'} = 0$ , as shown by the solid line in Fig. 5.4. It is also observed that the intensity of  $\pi\pi'$  scattering decreases with increasing temperature and disappears at  $T_N$  (Fig. 5.4 inset).

According to the formalism proposed by Nagao and Igarashi [73] (see Appendix for details), the scattering amplitude for the  $E1$  resonance originating from the magnetic dipole moment  $\mathbf{m}$  can be written as

$$F_{E1, \text{mag}} \propto -i(\boldsymbol{\varepsilon}' \times \boldsymbol{\varepsilon}) \cdot \mathbf{m}. \quad (5.1)$$

This means that the component of magnetic moment perpendicular to the scattering plane contributes to  $\pi\pi'$  scattering, while the in-plane component contributes to  $\pi\sigma'$  scattering. In the present scattering configuration, the experimental results of  $F^{\pi\pi'} \neq 0$  and  $F^{\pi\sigma'} = 0$  shows that the ordered magnetic moments are aligned along the  $c$ -axis. Thus, we confirmed by RXS measurements the existence of  $Q = 0$  component of AFM order, which is consistent with the previous reports based on neutron diffraction [44, 46]. In this case, a strong magnetic signal is expected to appear also at a ‘‘nearly forbidden’’ reciprocal lattice point in the  $(h0l)$  plane, where  $h+l = \text{odd}$ . Indeed, the magnetic signal was observed at  $(1, 0, 4)$  with a intensity 20 times larger than the lattice contribution.

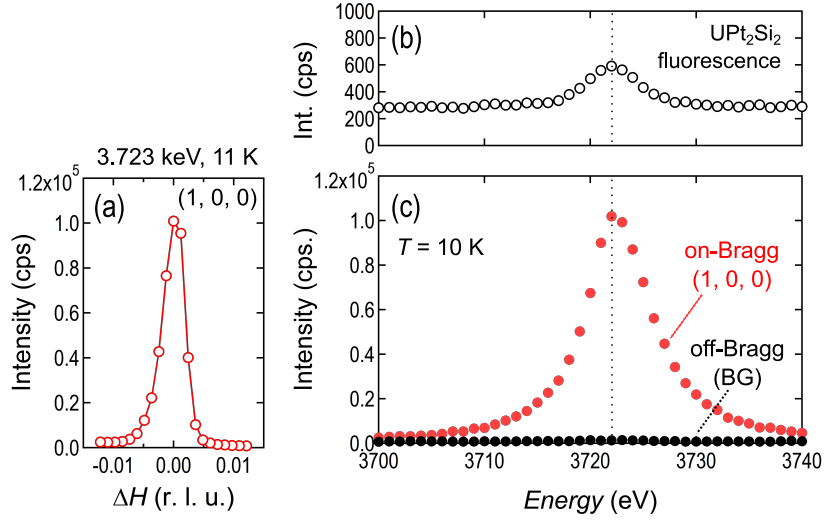


Figure 5.3: (Color online) (a) Peak profile of (1, 0, 0) reflection. Energy dependences of the scattering intensity of (a) fluorescence and (b) (1, 0, 0) reflection of  $\text{UPt}_2\text{Si}_2$  near the U  $M_4$  absorption edge.

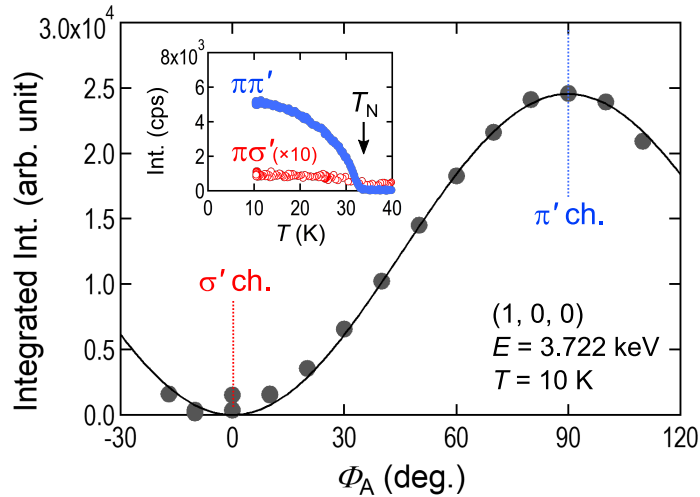


Figure 5.4: (Color online) Polarization dependence of (1, 0, 0) reflection intensity. The solid line is the model with magnetic moments parallel to the  $c$ -axis. The inset shows the temperature dependences of reflection intensity in  $\pi'$ -channel (blue filled circles) and  $\sigma'$ -channel (red open circles).

## 5.2.2 Search for superlattice reflections

Secondly, we investigated superlattice reflections corresponding to the period of the CDW in the AFM phase at the energy of 3.722 keV. Scanning along the  $h$  direction between the  $(2, 0, 0)$  fundamental lattice reflection and the  $(2, 1, 0)$  magnetic reflection, we found several reflections as shown in Fig. 5.5(a). The most prominent one,  $(2, 0.42, 0)$ , can be indexed as  $(2, 0, 0) + \mathbf{q}_{\text{CDW}}$ . Here  $\mathbf{q}_{\text{CDW}} = (0, \sim 0.42, 0)$ , which corresponds to one of the two  $\mathbf{q}$ -domains with  $\mathbf{q}_{\text{CDW}} \parallel [100]$  and  $\parallel [010]$  confirmed by previous study [53]. In addition, small reflections were observed at  $(2, 0.83, 0)$  and  $(2, 0.75, 0)$ , which can also be indexed using  $\mathbf{q}_{\text{CDW}}$  as  $(2, 0, 0) + 2\mathbf{q}_{\text{CDW}}$  and  $(2, 2, 0) - 3\mathbf{q}_{\text{CDW}}$ , respectively. The presence of harmonic components of  $2\mathbf{q}_{\text{CDW}}$  and  $3\mathbf{q}_{\text{CDW}}$  in the CDW has been confirmed by Lee *et al* [53]. Besides these reflections around the fundamental lattice reflections, this line scan also shows the presence of  $\mathbf{q}_{\text{CDW}}$  reflection,  $(2, 0.58, 0)$ , around the magnetic reflection, which has not been reported previously.

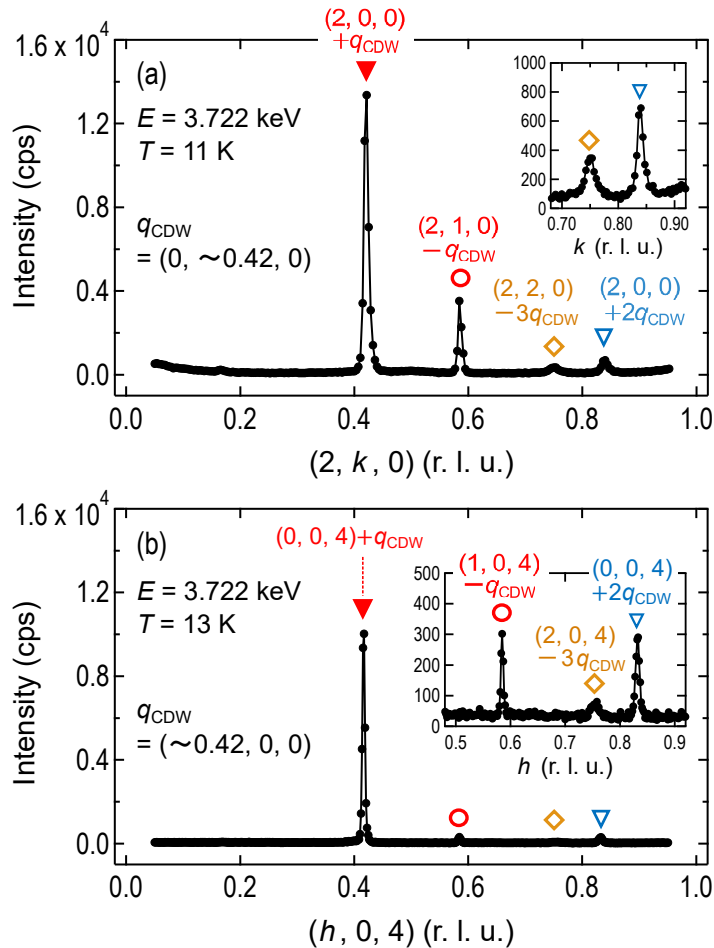


Figure 5.5: (Color online) (a)  $k$ -scan from  $(2, 0, 0)$  to  $(2, 1, 0)$  and (b)  $h$ -scan from  $(0, 0, 4)$  to  $(1, 0, 4)$  in the AFM phase with the energy of U  $M_4$  absorption edge. Insets show magnified views around satellite peaks of  $2\mathbf{q}_{\text{CDW}}$  and  $3\mathbf{q}_{\text{CDW}}$ .

A similar diffraction pattern was also found in the  $(h0l)$  scattering plane. Figure 5.5(b) displays the result of the  $h$ -scan between  $(0, 0, 4)$  and  $(1, 0, 4)$ . As observed in the  $k$ -scan, there is a prominent first satellite and weak second and third satellite peaks from the fundamental lattice reflections,  $(0, 0, 4)$  and  $(2, 0, 4)$ . There is also a weak first satellite peak from the main peak of  $(1, 0, 4)$ . Note that  $(1, 0, 4)$  is the nearly forbidden position where the strong magnetic signal was observed, while  $(0, 0, 4)$  is a large fundamental lattice reflection. In the following, the 1st satellite peak around the positions of  $(h, k, 0)$  for  $h + k = \text{odd}$  and  $(h, 0, l)$  for  $h + l = \text{odd}$ , where the magnetic signal corresponding to the AFM order with  $\mathbf{Q} = 0$  is observed, is distinguished and denoted as  $\boldsymbol{\tau}_M + \mathbf{q}_{\text{CDW}}$  reflection. The results of investigations of the features for the  $\mathbf{q}_{\text{CDW}}$  reflections, the  $2\mathbf{q}_{\text{CDW}}$  and  $3\mathbf{q}_{\text{CDW}}$  reflections, and  $\boldsymbol{\tau}_M + \mathbf{q}_{\text{CDW}}$  reflections will be presented separately in the following.



### 5.2.3 $q_{\text{CDW}}$ reflections

The polarization analyses were performed for  $(2, 0.42, 0)$  reflection in the energy range near the U  $M_4$ -edge. Figure 5.7 shows the polarization dependences of the scattering intensity at the resonant energy (3.722 keV) in the AFM phase and the PM phase. In the AFM phase, we observed strong intensities in the  $\pi'$  channel and significant signals in the  $\sigma'$  channel. As shown in Fig. 5.7(a), the energy dependence in  $\pi'$  channel shows an absorption of about 50% at 3.722 keV. This is typical behavior for non-resonant signals derived from crystal lattices near an absorption edge. The scattering intensities in  $\pi'$  channel at resonant and non-resonant energy do not show significant change around  $T_N$ , as shown in Fig. 5.7(c). The scattering observed in the  $\pi'$  channel can therefore be attributed to Thomson scattering due to the crystal lattice modulation by the CDW order with the atomic displacements confirmed by Lee *et al.* [53].

By contrast, the energy spectrum of the intensity in  $\sigma'$  channel exhibits a resonance-like enhancement at the absorption edge energy in the AFM phase as shown in Fig. 5.7(c). Scattering with a change in the polarization state of X-rays (from  $\pi$  to  $\sigma'$ ) is an inherent feature of RXS, suggesting the presence of magnetic dipoles or higher-order multipoles. Here we note that the finite signal intensity was also observed at off-resonance energies such as 3700 eV, due to a small contamination of the  $\sigma$ -polarized incident X-rays causing a  $\sigma\sigma'$  scattering (Thomson scattering) from the crystal lattice.

The scattering intensity at the resonance energy decreases with increasing temperature and almost disappears above  $T_N$  while the scattering intensity at non-resonance energy does not show temperature variation as shown in Fig. 5.7(d). As apparent from the energy spectrum of the PM phase in Fig. 5.7, the remaining signal above  $T_N$  is a contamination of the non-resonant  $\sigma\sigma'$  scattering. From these results, the resonant  $\pi\sigma'$  scattering observed only in the AFM phase is considered to be a magnetic signal. In this case, given from Eq. (1), the magnetic signal must be derived from the  $c$ -plane component of the magnetic moments of  $5f$  electrons. This means that the magnetic structure of this system has not only a  $\mathbf{Q} = 0$  component where the magnetic moments parallel to the  $c$ -axis form the staggered ordering, but also a component of magnetic modulation with the propagation vector of  $q_{\text{CDW}}$  where the  $c$ -plane components of the magnetic moments are spatially distributed.

To identify the structure of this  $c$ -plane magnetic modulation, we also performed the polarization analyses on another  $q_{\text{CDW}}$  superlattice reflection,  $(0.42, 0, 4)$ , with the scattering angle  $2\theta = 90.0^\circ$  at the resonant energy in the AFM phase. This specific diffraction condition allows us to extract only magnetic signals because the intensity of Thomson scattering in the  $\pi\pi'$  channel is proportional to  $\sin^2 2\theta$  and it becomes  $\sim 0$  at this reflection condition. Consequently, in this scattering configuration with the scattering plane of  $(h0l)$ , the  $c$ -plane component of the magnetic moment can be detected separately into the  $a$ -axis and  $b$ -axis components as  $\pi\sigma'$  and  $\pi\pi'$  scattering signals, respectively. Figure shows the polarization dependence of the scattering intensity and it is apparent that the scattered X-ray is purely  $\pi'$  polarized. This  $\pi'$  signal shows the clear resonant peak at the absorption edge as shown in the inset of Fig. 5.8.

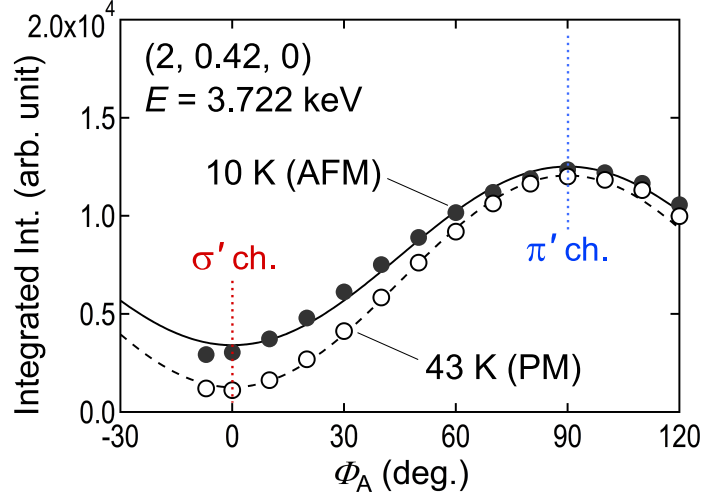


Figure 5.6: (Color online) The polarization dependence of  $(2, 0.42, 0)$  reflection at the resonant energy. The filled and blank symbols represent the data in the AFM phase at 10 K and the PM phase at 43 K, respectively. The bold and dashed lines are the fitting results assuming the combination of  $\pi'$  and  $\sigma'$  signals.

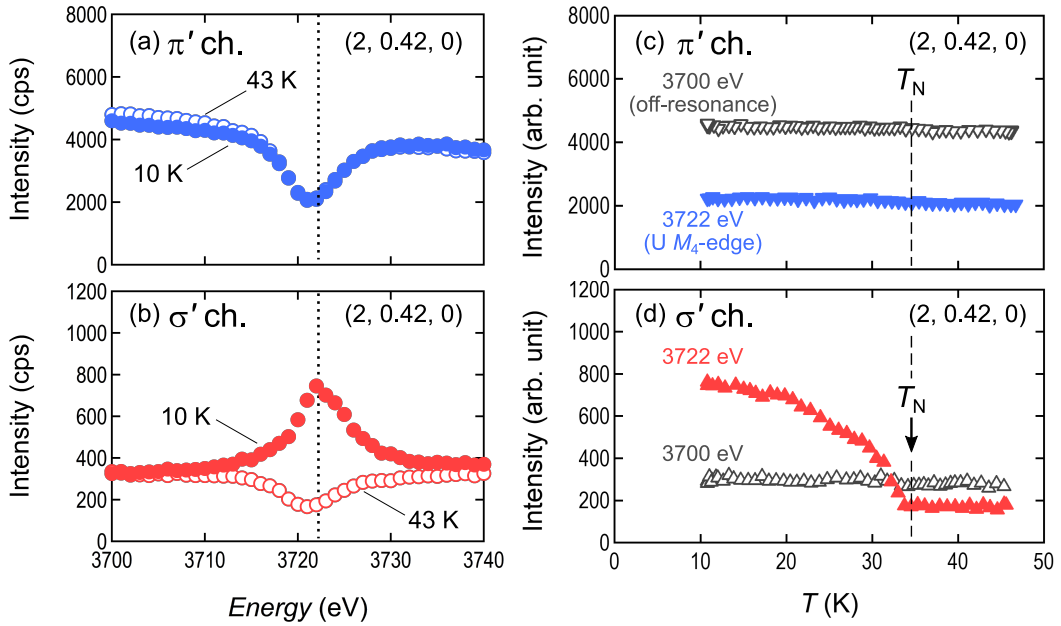


Figure 5.7: (Color online) Energy dependences of  $(2, 0.42, 0)$  reflection intensity at 10 K (filled circles) and 43 K (blank circles) of (a)  $\pi'$  signal and (b)  $\sigma'$  signal. Temperature dependences at the resonant energy (filled triangles) and non-resonant energy (blank triangles) of  $(2, 0.42, 0)$  reflection intensity in (c)  $\pi'$ -channel and (d)  $\sigma'$ -channel.

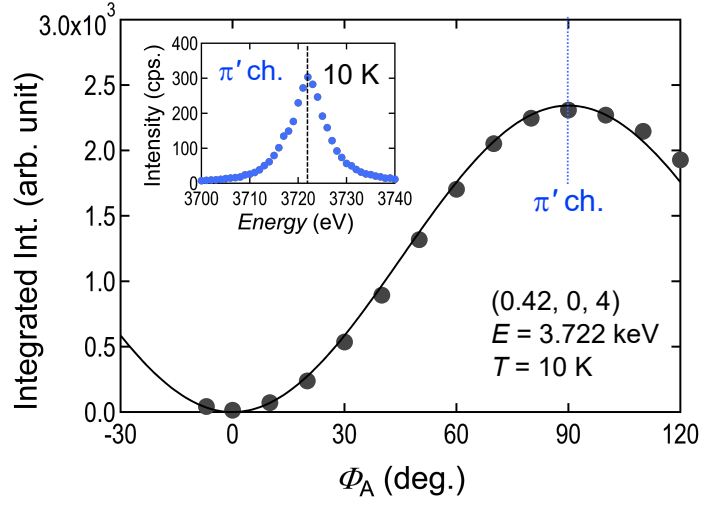


Figure 5.8: (Color online) The polarization dependence of (0.42, 0, 4) reflection at the resonant energy. The bold line is the fitting result for the magnetic components along the [010] direction. The inset shows the energy dependence at  $\pi'$ -channel.

In this scattering configuration,  $\pi\pi'$  scattering is caused by the  $b$ -axis component of magnetic moment which is perpendicular to  $\mathbf{q}_{\text{CDW}}$  and the absence of  $\pi\sigma'$  means that the  $c$ -plane magnetic modulation has only a transversal component.

## 5.2.4 $2\mathbf{q}_{\text{CDW}}$ and $3\mathbf{q}_{\text{CDW}}$ reflections

Further, polarization analyses have been performed also for higher harmonics components ( $2\mathbf{q}_{\text{CDW}}$ ,  $3\mathbf{q}_{\text{CDW}}$ ). The polarization dependence of  $2\mathbf{q}_{\text{CDW}}$  reflection intensity, (2, 0.83, 0), at the resonant energy in the AFM phase is shown in Fig. 5.9(a). It is well-fitted by the model assuming the fully  $\sigma'$ -polarized scattered X-rays. As presented in Fig. 5.9(b) and (c), the energy dependence of this  $\pi\sigma'$  scattering intensity shows a clear resonance peak at the absorption edge and this signal can be observed only below  $T_{\text{N}}$ . These energy spectrum and the temperature variation of the signal intensity are similar to those of other magnetic signals, and in this configuration this is a resonance signal corresponding to the  $c$ -plane component. In addition, a non-resonant  $\pi\pi'$  scattering signal was observed in the (2, 0.42, 0) reflection, which is the 1st satellite peak, but no such contribution was observed in this 2nd satellite peak.

In addition to this  $2\mathbf{q}_{\text{CDW}}$  superlattice reflection, we also checked another  $2\mathbf{q}_{\text{CDW}}$  reflection, (0.83, 0, 4). The polarization dependence of the scattering intensity is shown in Fig. 5.10(a) and it takes maximum at  $\Phi_{\text{A}} = 0$  and non-zero minimum at  $\Phi_{\text{A}} = 90^\circ$ . The signal of  $\pi\sigma'$  also shows a clear resonant energy spectrum while the  $\pi\pi'$  signal shows the typical non-resonant energy spectrum (Fig. 5.10(b) and (c)). The latter one can be regarded as the charge contribution caused by the CDW order as observed at (2, 0.42, 0). This non-resonant signals was not observed in the other  $2\mathbf{q}_{\text{CDW}}$  reflection, (2, 0.83, 0), suggesting the complexity of the diffraction pattern of the CDW reflections. Contrarily, the magnetic resonant signals are observed in both  $2\mathbf{q}_{\text{CDW}}$  reflections as  $\pi\sigma'$  scattering signals. This indicates that the signals originate from the parallel component of the magnetic moment to the  $\mathbf{q}_{\text{CDW}}$ . Namely, the structure of the  $c$ -plane magnetic modulation has not only a transverse component with  $\mathbf{q}_{\text{CDW}}$  but also a longitudinal component with  $2\mathbf{q}_{\text{CDW}}$ .

Such a contribution of magnetic modulation was also observed in the  $3\mathbf{q}_{\text{CDW}}$  reflection, (0.75, 0, 4). The measured polarization dependence of the scattering intensity indicates that the scattered X-rays are fully polarized in  $\pi'$ -state (Fig. 5.11(a)). Figures 5.11(b) and (c) display the energy spectrum of this reflection and the temperature dependence of the scattering intensity at 3.722 keV, measured without polarization analyzer. These results show that this is clearly a magnetic resonant signal which develops below  $T_{\text{N}}$ , with no significant non-resonant signal. This magnetic resonant signal of  $\pi\pi'$  scattering observed in the ( $h0l$ ) plane is different from the magnetic resonant signal of  $\pi\sigma$  scattering observed at (0.83, 0, 4), which originates from the [010] component of the magnetic moment perpendicular to the  $\mathbf{q}_{\text{CDW}}$  vector. In other words, this signal suggests the presence of transverse magnetic modulation in the  $c$ -plane that was observed in the  $\mathbf{q}_{\text{CDW}}$  reflection.

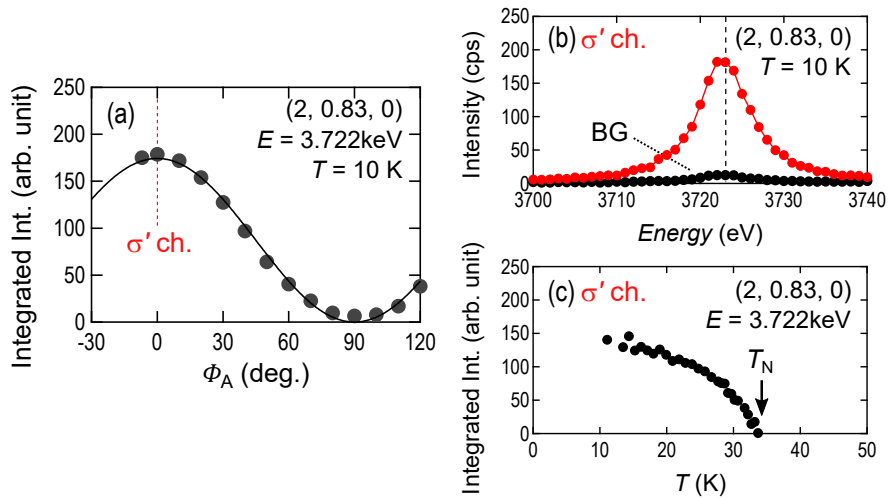


Figure 5.9: (Color online) (a) Polarization dependence of  $(2, 0.83, 0)$  reflection intensity at the resonant energy in the AFM phase. (b) Energy dependence of  $(2, 0.83, 0)$  reflection intensity in  $\sigma'$  channel at 10 K. The black circles are background (off-Bragg) data. (c) Temperature dependence of  $(2, 0.83, 0)$  reflection intensity in  $\sigma'$  channel.

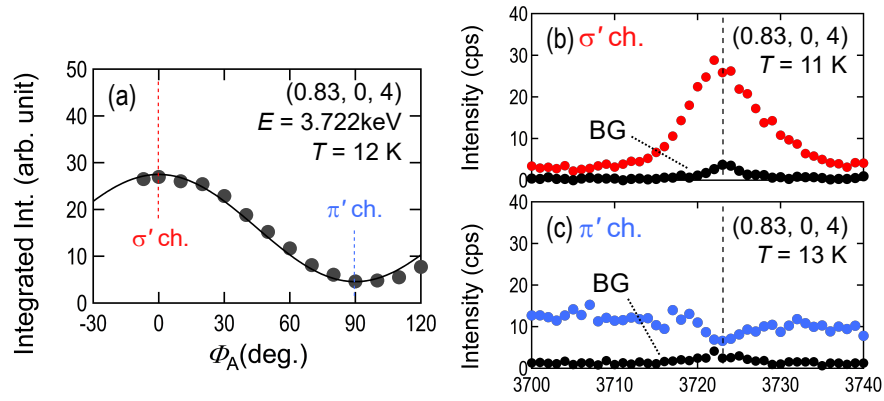


Figure 5.10: (Color online) (a) Polarization dependence of  $(0.83, 0, 4)$  reflection intensity at the resonant energy in the AFM phase. Energy dependence of  $(0.83, 0, 4)$  reflection intensity (b) in  $\sigma'$  channel at 11 K and (c) in  $\pi'$  channel at 13 K. The black circles are background (off-Bragg) data.

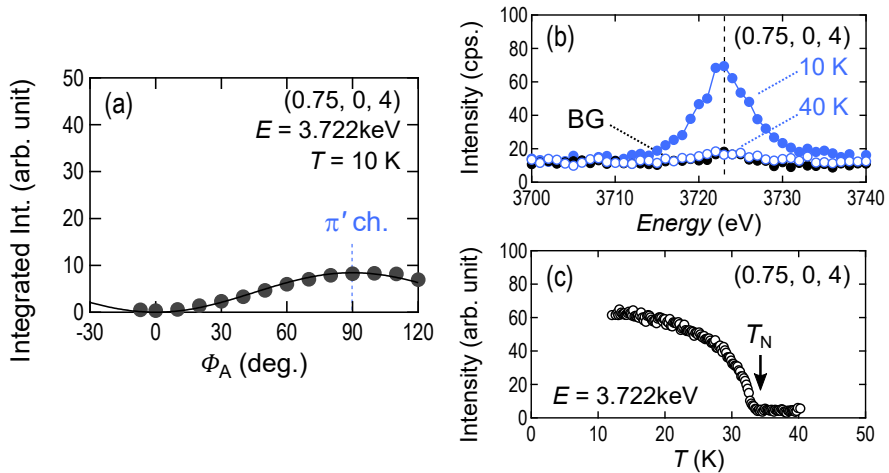


Figure 5.11: (Color online) (a) Polarization dependence of  $(0.75, 0, 4)$  reflection intensity at the resonant energy in the AFM phase. (b) Energy dependence of  $(0.75, 0, 4)$  reflection intensity at 10 K (blue filled circles) and 40 K (blue opened circles) without the polarization analyzer. The black circles are background (off-Bragg) data. (c) Temperature dependence of  $(0.75, 0, 4)$  reflection intensity without the polarization analyzer.

### 5.2.5 $\tau + \mathbf{q}_{\text{CDW}}$ reflections

The most surprising finding is the resonant signal at  $\mathbf{q}_{\text{CDW}}$  superlattice reflections around  $(2, 1, 0)$  forbidden reflection,  $(2, 0.58, 0)$ . The results of the polarization analyses on  $(2, 0.58, 0)$  reflection performed to investigate the origin of this signal are summarized in Fig. 5.12. The polarization dependence of the scattering intensity shows that the  $\pi\pi'$  scattering signal was observed as the dominant contribution in the AFM phase, while a finite  $\pi\sigma'$  scattering contribution was also observed. Each signal exhibits a distinct peak in the AFM phase (Figs. 5.12(a) (b)). In these peaks, the  $\pi\sigma'$  scattering signal appears to remain even above  $T_{\text{N}}$ , while the  $\pi\pi'$  scattering signal disappears. The continuous temperature variations are shown in inset in Fig. 5.12. The  $\pi\pi'$  signal disappears toward  $T_{\text{N}}$ , whereas the  $\pi\sigma'$  signal does not show significant change around  $T_{\text{N}}$ . As shown in Fig. 5.13, the energy spectrums of these signals are both clear resonance signals with peaks at the absorption edge. While this  $\pi\pi'$  resonant signal can be derived from the  $c$ -axis component of magnetic moments, the  $\sigma'$  polarized resonant signal seems not to be magnetic one. Since spherically symmetric electronic states do not change the polarization of X-ray, this resonant signal of  $\pi\sigma'$  scattering is considered to be caused by anisotropic  $5f$  electronic states such as electric quadrupoles.

Such a non-magnetic signal was also found in the  $(h0l)$  plane as the satellite from the main peak of  $(1, 0, 4)$ ,  $(0.58, 0, 4)$  reflection. The polarization dependence of this signal in the AFM phase is shown in Fig. 5.14. This result indicates that this signal is perfect  $\pi\sigma'$  scattering with no  $\pi\pi'$  scattering contribution within experimental accuracy. This  $\pi\sigma'$  signal is apparently a resonant signal, where the energy spectrum shows a resonant peak near the absorption edge (Fig. 5.15 (a)). As the temperature increases to the PM phase, the intensity decreases slightly, but the distinct peak is largely retained even in the PM phase. This slight deviation can be attributed to the magnetic contribution associated with the  $c$ -axis component of the magnetic moments observed as  $\pi\pi'$  scattering signal at  $(2, 0.58, 0)$ . The remaining resonant signal above  $T_{\text{N}}$  is similar to the signal observed at  $(2, 0.58, 0)$ .

To investigate the properties of this remaining signal, we performed some measurements on the  $(2, 0.58, 0)$  reflection in higher temperature region above 50 K without the polarization analyzer. Figure 5.16 (a) shows the  $k$ -scans from  $(2, 0.56, 0)$  to  $(2, 0.62, 0)$  at temperatures ranging from 50 K to 280 K. The intensity gradually decreases with increasing temperature and almost disappears at 280 K. For the data at each temperature, we performed Gaussian-fitting and calculated integrated intensities. The obtained temperature dependence of integrated intensity and peak position are plotted in Fig. 5.16 (b) and (c), respectively. The peak position  $k$  is shifted  $\sim 0.58$  to  $\sim 0.60$  above near 180 K which is reported as the lock-in temperature of  $\mathbf{q}_{\text{CDW}}$  [53].

To identify the origin of this resonant signal, we performed the azimuthal angle dependence measurement using a sample with a wide plane perpendicular to the scattering vector of  $\kappa = (2, 0.58, 0)$ . Figure 5.17 shows the azimuthal angle dependence of  $(2, 0.58, 0)$  reflection intensity in PM phase (40 K) at the resonant energy with the polarization analyzer fixed at  $\pi\sigma'$ -channel. The intensity shows a complex depen-

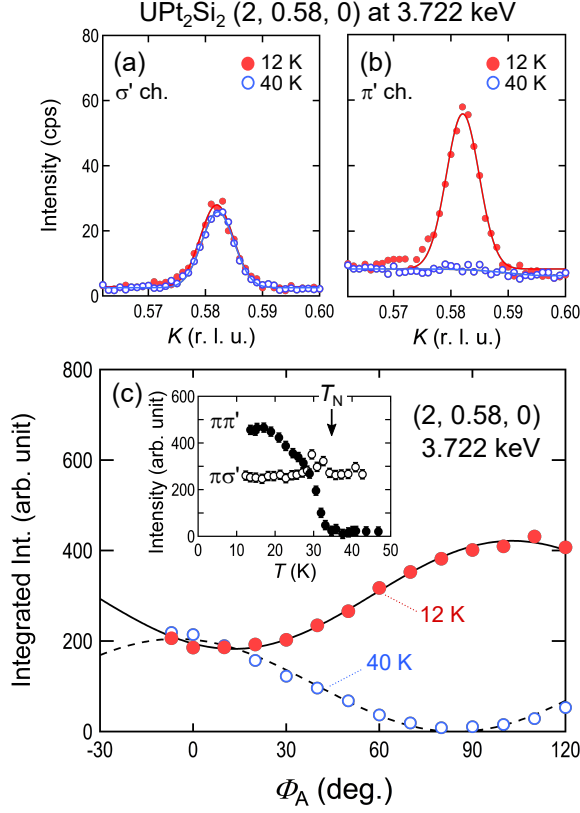


Figure 5.12: (Color online) (a)  $K$ -scan profiles through (2, 0.58, 0) reflection in (a)  $\sigma'$  and (b)  $\pi'$  channel. Red filled circles and blue blank circles denote the data measured at 12 K and 40 K, respectively. (c) Polarization dependences of (2, 0.58, 0) reflection intensity at 12 K (red filled circles) and 40 K (blue blank circles) at the resonant energy. Solid-line and dashed-line are fitting results for the data at 12 K and 40 K, respectively. The inset shows temperature dependences of the intensities of  $\pi\sigma'$  scattering (filled circles) and  $\pi\pi'$  scattering (blank circles) at the resonant energy.

dence on  $\varphi$ -angle, taking a local minimum around  $\varphi = 0$  and the maximum around  $\varphi = -45^\circ$ . This behavior cannot be explained by a 2-fold rotationally symmetric component alone, suggesting the presence of a 4-fold rotational symmetry component arising from the presence of electric quadrupoles. We performed curve-fitting with a model assuming the quadrupole density wave (QDW) with the period of  $\mathbf{q}_{\text{CDW}}$  by using eq. (9) in Appendix. The bold line in Fig. 5.17 is the fitting result assuming the density wave of  $O_{yz}$  and  $O_{zx}$  quadrupoles with the multipole structure factors  $Z_A$  (for A-sublattice) and  $Z_B$  (for B-sublattice) as follows:

$$\begin{aligned}
 Z_A &= \begin{cases} \sum_j O_{zx}^0 \sin(\mathbf{q}_{\text{CDW}} \cdot \mathbf{r}_j) e^{i\mathbf{k} \cdot \mathbf{r}_j} \\ \sum_j O_{yz}^0 \sin(\mathbf{q}_{\text{CDW}} \cdot \mathbf{r}_j) e^{i\mathbf{k} \cdot \mathbf{r}_j} \end{cases} \\
 Z_B &= \begin{cases} \sum_j -O_{zx}^0 \sin(\mathbf{q}_{\text{CDW}} \cdot \mathbf{r}_j) e^{i\mathbf{k} \cdot \mathbf{r}_j} \\ \sum_j -O_{yz}^0 \sin(\mathbf{q}_{\text{CDW}} \cdot \mathbf{r}_j) e^{i\mathbf{k} \cdot \mathbf{r}_j} \end{cases}
 \end{aligned} \tag{5.2}$$



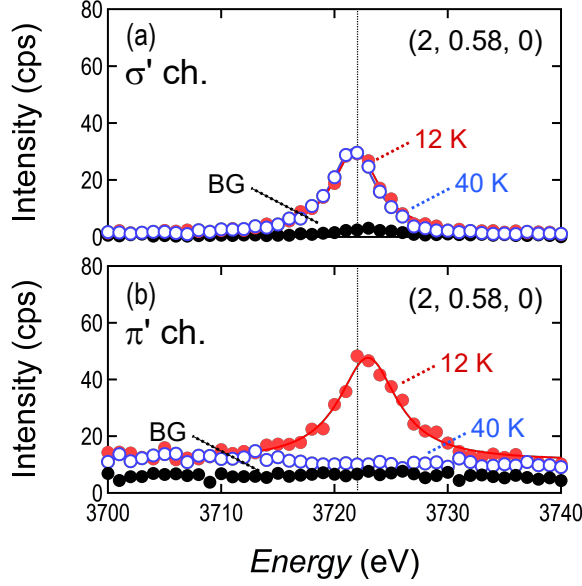


Figure 5.13: (Color online) Energy dependences of  $(2, 0.58, 0)$  scattering intensity in (a)  $\sigma'$  channel and (b)  $\pi'$  channel measured at 12 K and 40 K. The solid lines are Lorentzian-fitting for the data.

where  $\mathbf{r}_j$  is the position of  $j$ -th ion in the unit cell,  $\boldsymbol{\kappa}$  is the scattering vector,  $O_{zx}^0$  and  $O_{yz}^0$  are the amplitudes of the QDW for each quadrupole component, which are the fitting parameters in this calculation. The obtained fitting result is  $O_{zx}^0 : O_{yz}^0 = 1 : 0.056(7)$  and it shows good agreement with the experimental data. We also checked the consistency of the model with the polarization dependence of this reflection intensity. As shown in Fig. 5.18 (a), we observed the rotation of polarization plane of the scattered X-rays with  $\varphi$ -rotation. Around  $\varphi = -30^\circ$  to  $-45^\circ$ , the polarization plane rotated by  $\sim 20^\circ$  and the intensity reaches maximum. Turning  $\varphi$  further, the polarization plane can be seen to return to  $\sigma'$  state with decreasing intensity. We calculated the polarization dependence at each  $\varphi$  from the model for the fitting of  $\varphi$  dependence at  $\sigma'$ -channel and plotted in Fig. 5.18 (b). Comparison with experimental results shows that this model can successfully explain the features mentioned above. The  $O_{zx}$ -type quadrupole, which provides the dominant component in this model, corresponds to a charge distribution extending in the plane perpendicular to the direction of  $\mathbf{q}_{\text{CDW}}$ . The imbalance between  $O_{zx}^0$  and  $O_{yz}^0$  here means the breaking of the four-fold rotational symmetry in the U 5f electronic state as the CDW is formed. Note that only modulation of the charge distribution with  $\mathbf{q}_{\text{CDW}}$  can be detected in our experiments, and the observed QDWs correspond to deviations from the electronic state under the tetragonal symmetry. Furthermore, the obtained QDW model also well explains the presence of the  $\pi\sigma'$  scattering contribution and the absence of the  $\pi\pi'$  scattering contribution in the  $(0.58, 0, 4)$  reflection. It is also important to note that this reflection belongs to the domain with  $\mathbf{q}_{\text{CDW}} \parallel [100]$ , while the  $(2, 0.58, 0)$  reflection belongs to the another domain with  $\mathbf{q}_{\text{CDW}} \parallel [010]$ . Namely, for the  $(0.58, 0, 4)$  reflection, the

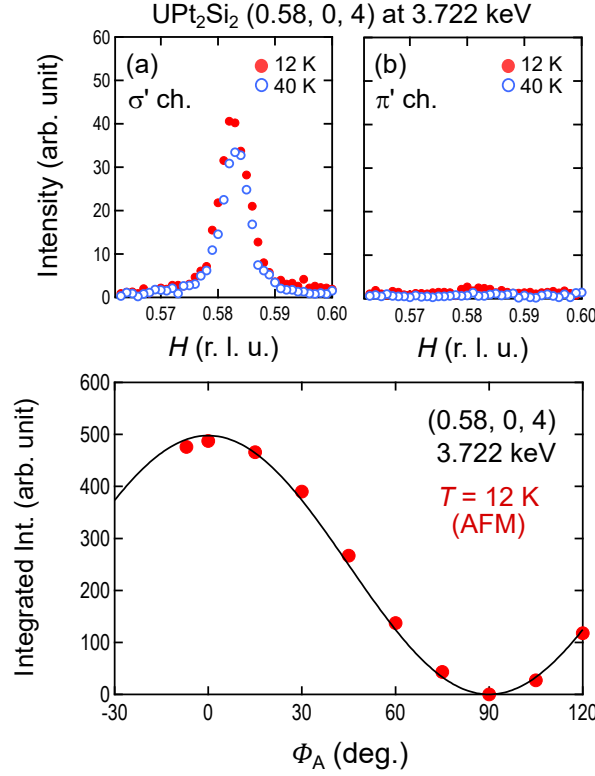


Figure 5.14: (Color online) The  $h$ -scan profiles through (0.58, 0, 4) reflection in (a)  $\sigma'$  and (b)  $\pi'$  channel. Red filled circles and blue blank circles denote the data measured at 12 K and 40 K, respectively. (c) Polarization dependences of (0.58, 0, 4) reflection intensity at 12 K (red filled circles) and 40 K (blue blank circles) at the resonant energy. Solid-line is the fitting results for the data at 12 K assuming only  $\sigma'$  polarized scattered X-rays.

observed resonant signals of  $\pi\sigma'$  scattering and the absence of the  $\pi\pi'$  scattering signal can be explained consistently with the obtained QDW model, where  $O_{yz}$  is the dominant contribution for  $\mathbf{q}_{\text{CDW}} \parallel [100]$ .

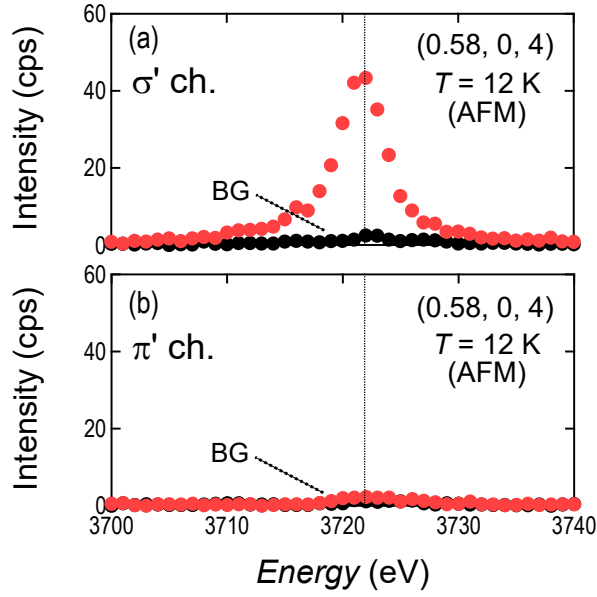


Figure 5.15: (Color online) Energy dependences of  $(0.58, 0, 4)$  reflection intensity of (a)  $\pi\sigma'$  and (b)  $\pi\pi'$  at 12 K and 40 K.

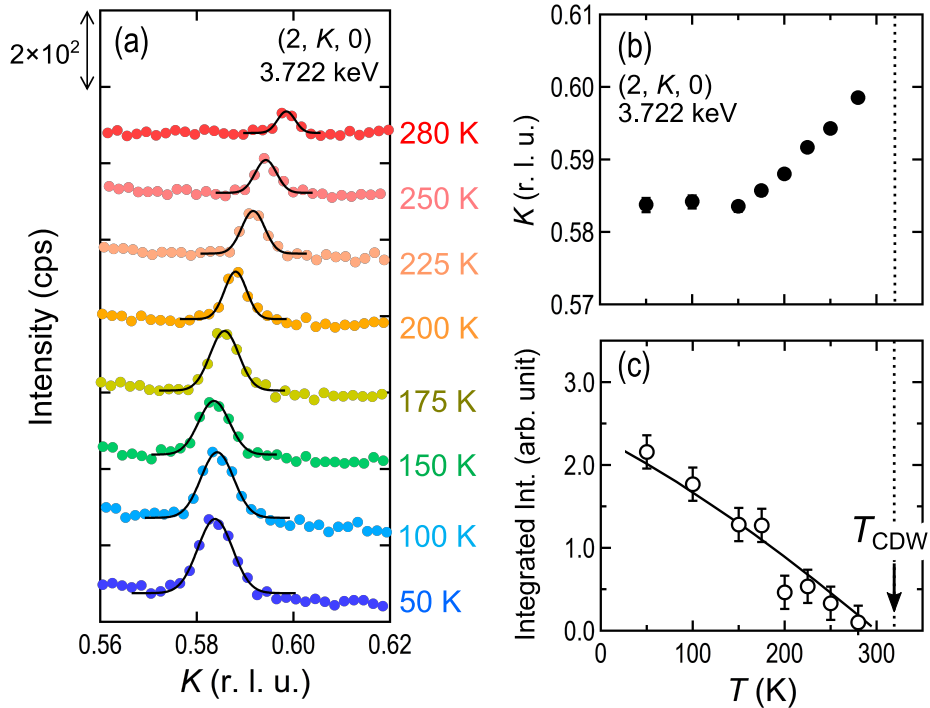


Figure 5.16: (Color online) (a)  $k$ -scan profiles of  $(2, \sim 0.58, 0)$  reflection at the resonant energy without polarization analyzer system. The base lines are shifted for clarity. The bold lines are Gaussian-fitting curves at each temperature. Temperature dependences of (b) the integrated intensity and (c) the peak position obtained from the Gaussian-fitting. The curved line in (b) is guide to the eye.

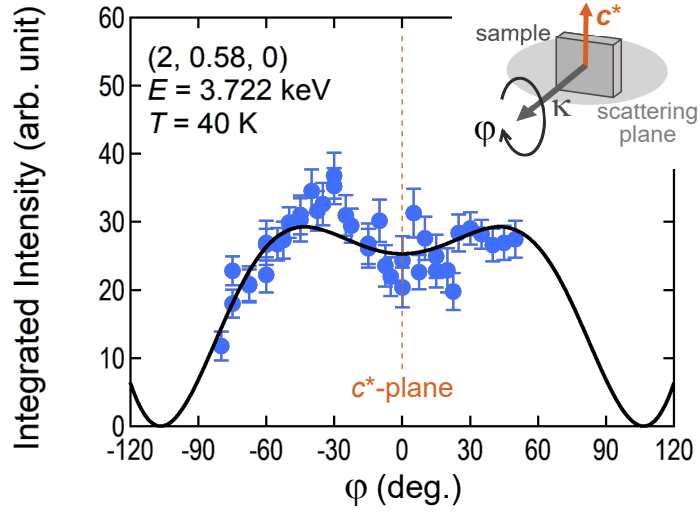


Figure 5.17: (Color online) Azimuthal angle ( $\varphi$ ) dependences of  $(2, 0.58, 0)$  reflection intensity in  $\sigma'$  channel measured at 40 K. The inset shows the sample setting at  $\varphi = 0$ , where  $c^*$  is perpendicular to the scattering plane. The solid line is the fitting result assuming the combination of  $O_{zx}$  and  $O_{yz}$  type QDWs.

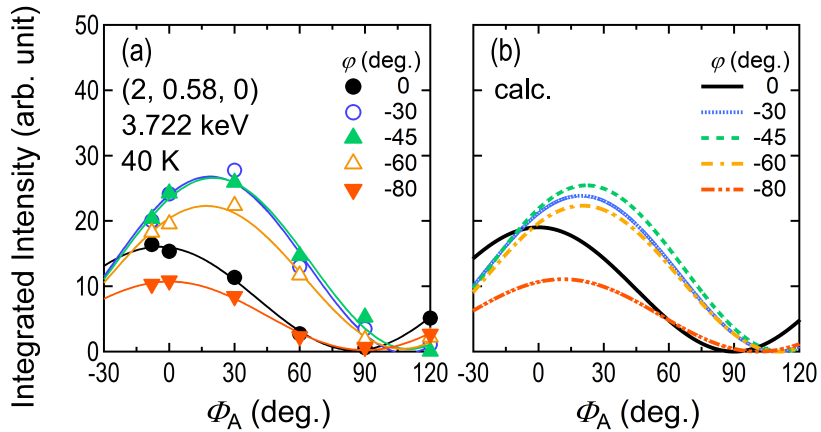


Figure 5.18: (Color online) (a) Polarization dependences of  $(2, 0.58, 0)$  reflection intensity at  $\varphi = 0$  to  $-80^\circ$ . (b) Calculation of the polarization dependences of  $(2, 0.58, 0)$  reflection intensity at each  $\varphi$  for the model assuming the combination of  $O_{zx}$  and  $O_{yz}$  type QDWs.

## 5.2.6 Short summary of results in RXS experiments

We performed RXS experiments using the energy of U  $M_4$  absorption edge to obtain the information of  $5f$  electronic states under the CDW order by Pt  $5d$  electrons. The observed resonant signals in our experiments are summarized in Table 5.1. It is revealed that the magnetic structure of this system is modulated with the same periodicity to the CDW order including its higher harmonics components. The observed magnetic components are summarized in Fig. 5.19. We found the  $c$ -plane magnetic modulation, which consists of three components: the transverse components ( $\delta\mu$  with  $q_{\text{CDW}}$ ,  $\delta\mu''$  with  $3q_{\text{CDW}}$  and the longitudinal component ( $\delta\mu'$  with  $2q_{\text{CDW}}$ ). In addition, the magnetic modulation along the  $c$ -axis ( $\delta\mu'''$ ) is also found. Moreover, it is also found that the resonant signals in the PM phase indicating the modulation of electronic distributions of  $5f$  electrons as the  $O_{yz}$  and  $O_{\bar{y}\bar{z}}$ -types of QDWs. This electronic modulation is antiphase between the two sublattices of U as mentioned in Chapter 7.

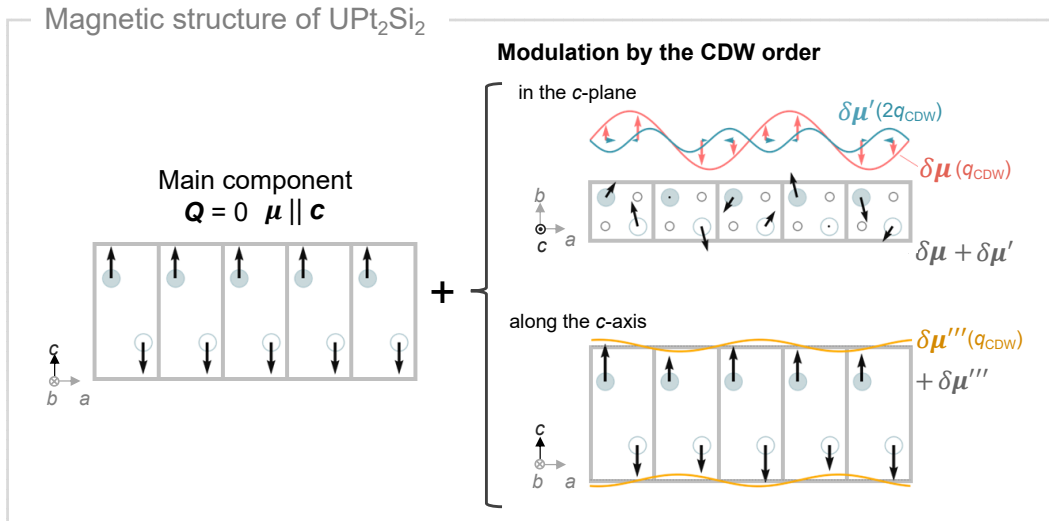


Figure 5.19: (Color online) Illustration of the magnetic structure determined from the results of these RXS experiments including the magnetic modulations.

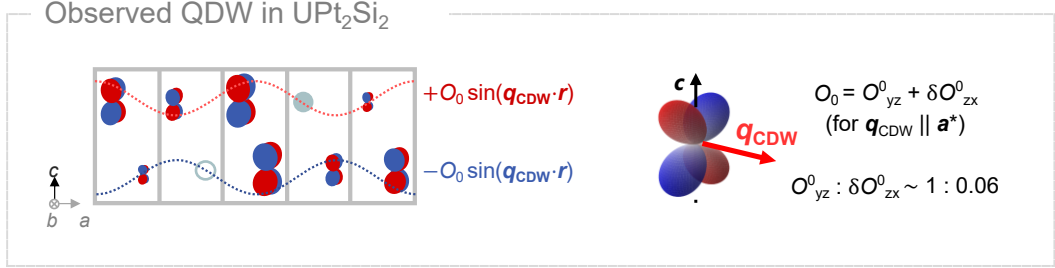


Figure 5.20: (Color online) Illustration of the QDW determined from the results of these RXS experiments. Note that it is shown for the domain with  $\mathbf{q}_{\text{CDW}} \parallel \mathbf{a}^*$ .

Table 5.1: The summary of the observed signals associated with the AFM order, the CDW order and the CDW-induced magnetic modulations ( $\delta\boldsymbol{\mu}$ ,  $\delta\boldsymbol{\mu}'$ ,  $\delta\boldsymbol{\mu}''$  and  $\delta\boldsymbol{\mu}'''$ ) and QDW.

Propagation vector	Reflection	Pol.	Energy dependence	Observed temp. range	Origin
$\mathbf{Q} = 0$	(1, 0, 0)	$\pi\pi'$	reso.	$T < T_N$	$\boldsymbol{\mu}$ ( $\parallel \mathbf{c}$ )
$\mathbf{q}_{\text{CDW}}$	(2, 0.42, 0)	$\pi\sigma'$	reso.	$T < T_N$	$\delta\boldsymbol{\mu}$
		$\pi\pi'$	non-reso.	$T < T_{\text{CDW}}$	charge
	(0.42, 0, 4)	$\pi\pi'$	reso.	$T < T_N$	$\delta\boldsymbol{\mu}$
$2\mathbf{q}_{\text{CDW}}$	(2, 0.83, 0)	$\pi\sigma'$	reso.	$T < T_N$	$\delta\boldsymbol{\mu}'$
	(0.83, 0, 4)	$\pi\sigma'$	reso.	$T < T_N$	$\delta\boldsymbol{\mu}'$
		$\pi\pi'$	non-reso.	$T < T_{\text{CDW}}$	charge
$3\mathbf{q}_{\text{CDW}}$	(0.75, 0, 4)	$\pi\sigma'$	reso.	$T < T_N$	$\delta\boldsymbol{\mu}''$
$\boldsymbol{\tau} + \mathbf{q}_{\text{CDW}}$	(2, 0.58, 0)	$\pi\sigma'$	reso.	$T < T_{\text{CDW}}$	QDW
		$\pi\pi'$	reso.	$T < T_N$	$\delta\boldsymbol{\mu}'''$ ( $\parallel \mathbf{c}$ )
$\boldsymbol{\tau} + \mathbf{q}_{\text{CDW}}$	(0.58, 0, 4)	$\pi\sigma'$	reso.	PM (40 K)	QDW
		$\pi\sigma'$	reso.	AFM (12 K)	$\delta\boldsymbol{\mu}'''$ ( $\parallel \mathbf{c}$ )

# Chapter 6

## Neutron Scattering Experiments on $\text{UPt}_2\text{Si}_2$

### 6.1 Experimental Procedure

The rod-shaped single-crystalline sample, grown along the  $c$ -axis, was synthesized using the Choklarzky method at Hokkaido University. The neutron diffraction experiments were performed by using the polarized neutron triple-axis spectrometer PONTA in Japan Research Reactor 3 (JRR-3). The schematic view of the spectrometer is illustrated in Fig. 6.2. The measurements were performed in the following two modes. The first, “unpolarized mode”, utilized neutrons with the energy of  $E = 34.06$  meV ( $\lambda = 1.550$ ), without spin polarizationpyrolytic graphite (PG) crystals served as both the monochromator and analyzer. The second, “polarized mode”, employed neutrons with  $E = 14.7$ meV ( $\lambda = 2.359$ ) monochromized and polarized by a Heusler crystal. Simultaneously, the spin state of scattered neutrons is analyzed in the polarization direction of the incident neutrons using another Heusler crystal. In this mode, to determine the change in the neutron spin state before and after scattering, the spin polarity of the incident neutrons is controlled by turning on and off the spin flipper. The device is positioned just before the sample, as illustrated in Fig. 6.3. When the flipper is activated, a spin flip (SF) signal is detected, indicating that the neutron spin flips from down to up during the scattering. Conversely, when the flipper is deactivated, a non-spin flip (NSF) signal is observed, signifying that the spin state remains up throughout the scattering process. The direction of spin polarization at the sample position is controlled by the magnetic field ( $\sim 1$  mT) generated by the Helmholtz coil. In the present study, we used two configurations: the  $P_{xx}$  setting, which polarizes the neutron spin parallel to the scattering vector, and the  $P_{zz}$  setting, which polarizes the neutron spin perpendicular to the scattering plane. Here, we adopt a coordinate system with the  $x$ -axis parallel to the scattering vector, and the  $z$ -axis perpendicular to the scattering vector, as depicted in Fig. 6.2.

In polarized neutron diffraction measurements, three distinct signals can be differentiated: nuclear scattering, magnetic scattering from the  $y$  component of magnetic

moment ( $M_y$ ), and magnetic scattering from the  $z$  component of magnetic moment ( $M_z$ ). This distinction can be achieved by analyzing the SF and NSF signals in the two aforementioned settings [76]. The relationships between the SF/NSF signals and their respective scatterers in the  $P_{xx}$  and  $P_{zz}$  settings are concisely summarized in Table 6.1. In the present experimental setup, the spin polarizations of the neutron beam were estimated to be  $P_0 = 0.8842$  in the  $P_{xx}$  setting and  $P_0 = 0.9116$  (in  $P_{zz}$  setting). These values were measured using  $(2, 0, 0)$  nuclear Bragg reflection of the sample. We used a  $^3\text{He}$  0-dimensional detector in both modes. The temperature at the sample position was controlled by a closed-cycle GM (Gifford-McMahon) refrigerator, with a range spanning from 2.3 K to 50 K.



Figure 6.1: (Color online) The sample used for this neutron diffraction measurements.

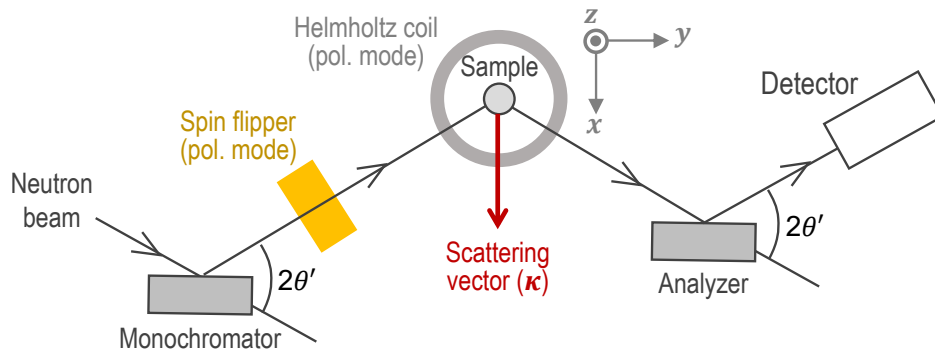
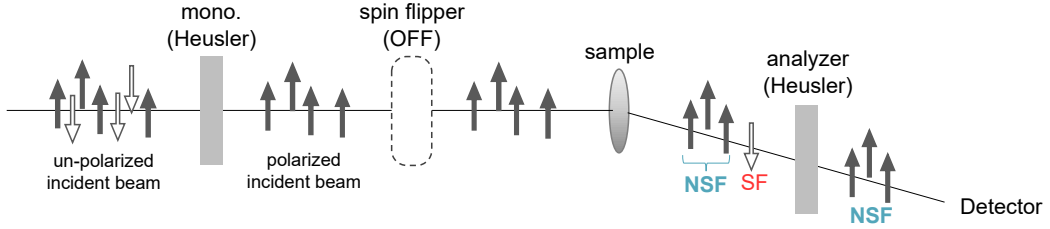


Figure 6.2: (Color online) A Schematic view of a triple-axis spectrometer (PONTA). The Cartesian coordinate  $xyz$  is introduced with the  $z$ -axis perpendicular to the scattering plane and the  $x$ -axis parallel to the scattering vector  $\kappa$ .



### 1. detection of NSF signal



### 2. detection of SF signal

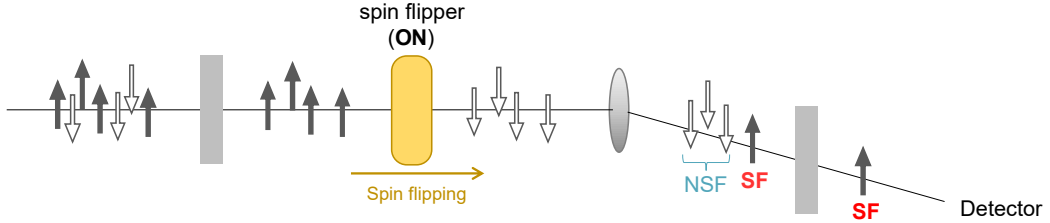


Figure 6.3: (Color online) A schematic view of the selective detection of SF and NSF signals using the spin flipper.

	$P_{xx}$	$P_{zz}$
SF	$M_{\perp c}$	$M_{\perp c}, M_{\parallel c}$
NSF	nuclear, $M_{\parallel c}$	nuclear

Table 6.1: The relationship between signal types and their origins in polarized neutron diffraction measurements with  $P_{xx}$  or  $P_{zz}$  setting. Non-spin-flip (NSF) scattering refers to the case where the spin of the scattered neutron does not invert from the incident neutron spin state, while spin-flip (SF) scattering refers to the case where the spin of the scattered neutron inverts from the incident neutron spin state.  $M_z$  denotes the component of the magnetic moment that is perpendicular to the scattering plane, while  $M_y$  denotes the in-plane component, which is perpendicular to  $\kappa$ .

## 6.2 Experimental Results

### 6.2.1 $Q = 0$ magnetic reflections

As reported in previous studies [44, 43, 46], we observed diffraction peaks in the AFM phase at the positions  $\tau = (h, k, 0)$  ( $h + k = \text{odd}$ ) that are forbidden for this crystal structure. Figure 6.4 shows typical peak profiles obtained from rocking curve measurements at the  $(1, 0, 0)$  and  $(2, 1, 0)$  reflection positions at 2.3 K and 50 K in the AFM and paramagnetic (PM) phases, respectively. Clear reflections were observed in the AFM phase at both positions, and their intensities significantly decreased upon heating to 50 K. The residual signals at 50 K are attributed to nuclear reflections of  $2\tau$ , caused by the higher order contamination ( $\lambda/2$ ) in the incident neutrons. By subtracting this extrinsic contribution at 50 K as background, we analyzed the intrinsic magnetic scattering intensities that develop at low temperatures. The net scattering profiles at 2.3 K are shown with black symbols and the solid lines in Fig. 6.4.

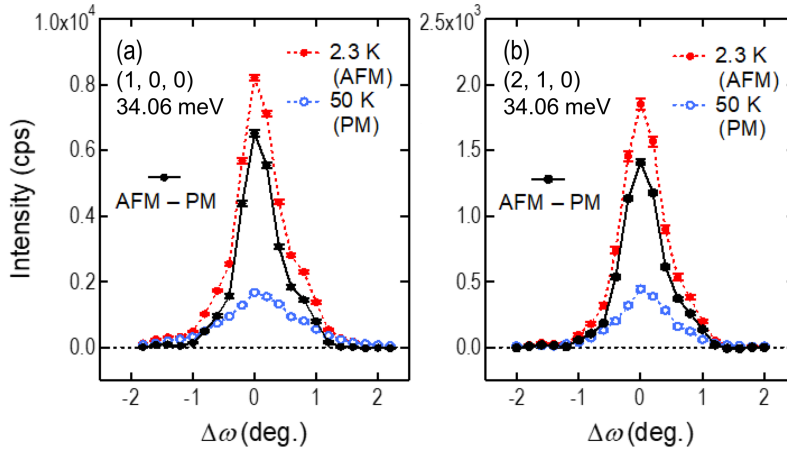


Figure 6.4: (Color online) The peak profiles measured in the unpolarized mode for (a)  $(1, 0, 0)$  and (b)  $(2, 1, 0)$  reflections. The dashed lines with red symbols correspond to the data in the AFM phase at 2.3 K, and the dashed lines with blank blue symbols represent the data in the PM phase at 50 K. The data represented by the solid lines with black symbols are the results of subtracting the PM phase data from the AFM phase data.

The integrated intensity,  $I_{mag}$ , of a magnetic profile at the scattering vector  $\kappa$  is proportional to the square of  $\mathbf{M}_{\perp}(\kappa)$ . Here,  $\mathbf{M}_{\perp}(\kappa)$  refers to the projection of  $\mathbf{M}(\kappa)$  onto the plane perpendicular to  $\kappa$ .  $\mathbf{M}(\kappa)$  is the component of the Fourier-transformed magnetic-moment distributions with respect to  $\kappa$  (see section 4.3).  $I_{mag}$  is expressed by the following equation:

$$I_{mag}(\kappa) = KL(\kappa) |F_m(\kappa)|^2, \quad (6.1)$$

where  $K$  is the scale factor typically estimated from nuclear scattering intensities,  $L(\kappa)$  is the Lorentz factor, and  $F_m(\kappa)$  is the magnetic structure factor per nuclear unit cell,

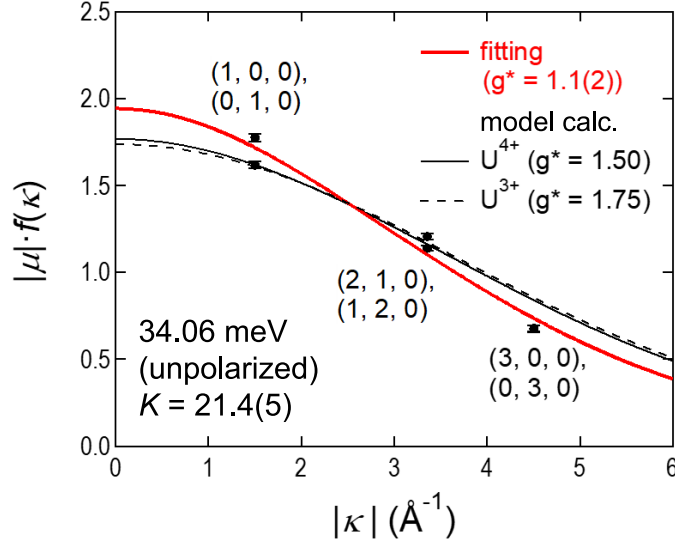


Figure 6.5: (Color online) The values of  $|\mu| \cdot f_U$  estimated from the integrated intensities of magnetic reflections with  $\mathbf{Q} = 0$ , where  $|\mu|$  represents the amplitude of magnetic moments, and  $f_U$  is the form factor of U. The curved lines are the fitting results to the experimental data. The thin solid and dashed black curves are based on assumptions for  $U^{4+}$  and  $U^{3+}$  ions, respectively. The bold red curve represents the fitting result using the parameters of  $|\mu|$  and  $g^*$  with the calculated functions of  $\langle j_0(\kappa) \rangle$  and  $\langle j_2(\kappa) \rangle$  for  $U^{4+}$ .

defined as

$$|F_m(\boldsymbol{\kappa})| = b_{mag} \cdot |\boldsymbol{\mu}_\perp| \cdot f_U(\kappa) \cdot A(\kappa). \quad (6.2)$$

Here,  $b_{mag}$  is the factor that converts the magnitude of the magnetic moment to the scattering length, a constant corresponding to the scattering length per  $1\mu_B$  (2.7 fm).  $A(\kappa)$  represents the phase factor, and  $|\boldsymbol{\mu}_\perp|$  is the magnitude of the projected vector of  $\boldsymbol{\mu}$  onto the plane perpendicular to  $\boldsymbol{\kappa}$ . For the AFM order with  $\mathbf{Q} = 0$ , where the ordered moments are parallel to the  $c$ -axis, these values are calculated as  $A(\kappa) = 2$  and  $|\boldsymbol{\mu}_\perp| = |\boldsymbol{\mu}|$ , respectively. The magnetic form factor of U,  $f_U(\kappa)$ , is a function that can be approximated by expanding it using an  $l$ 'th order basis  $j_l(\kappa)$  of spherical Bessel functions as follows:

$$f_U(\kappa) = \langle j_0(\kappa) \rangle + g^* \langle j_2(\kappa) \rangle, \quad (6.3)$$

where  $g^*$  is defined as:

$$g^* = \frac{J(J+1) + L(L+1) - S(S+1)}{3J(J+1) - L(L+1) + S(S+1)}. \quad (6.4)$$

In this formula,  $j_0(\kappa)$  is the term derived from the spin and orbital angular momentum of the electron, and  $\langle j_2(\kappa) \rangle$  is the term derived purely from the orbital angular momentum. These terms have been calculated using the Dirac-Fock method for the free ion model of  $U^{4+}$  ( $g^* = 1.50$ ) and  $U^{3+}$  ( $g^* = 1.75$ ) [77].

These calculations are based on the assumption of isotropic electronic states. However, in actual crystals, anisotropic electronic states may arise due to CEF effects, which necessitate consideration. In our analysis, following the approach commonly used for many f-electron systems, the magnetic form factor for this system experimentally estimated using  $g^*$  as a fitting parameter. The magnetic scattering intensity observed at each reflection is converted into the product of  $\mu$  and  $f_U(\kappa)$  using the Eqs. (6.1) and (6.2). The resulting values are then plotted against  $\kappa$ , as shown in Fig. 6.5. The thin solid and dashed black curves represent the fitting results using the calculated values of  $f_U(\kappa)$  for  $U^{4+}$  and  $U^{3+}$ , respectively, with  $|\boldsymbol{\mu}|$  being the only parameter in the calculations. There are no significant differences between the two models, and reproduce the experimental results quite well. To further improve the agreement with the experimental data,  $f_U(\kappa)$  was experimentally determined by fitting both of  $|\boldsymbol{\mu}|$  and  $g^*$  as parameters, taking into account the anisotropy of the electronic state. The result is shown in Fig. 6.5 with a red bold curve. For this fitting,  $j_l(\kappa)$  ( $l = 0, 2$ ) for  $U^{4+}$  was used. The obtained value of  $\mu$  is  $1.93(5) \mu_B$  ( $g^* = 1.1(2)$ ), which is consistent with the variation in values previously reported ( $1.67\text{--}2.5 \mu_B/U$ ) [44, 43, 46].

To ascertain the direction of the moment, these signals were also investigated in polarized mode. Figure 6.6 displays representative profiles from rocking curve measurements at the  $(1, 0, 0)$  reflection. Specifically, Fig. 6.6 (a) and (b) present the peak profiles measured at 2.3 K (in the AFM phase) and 50 K (in the PM phase) in the  $P_{xx}$  setting. In this setting, nuclear and magnetic scatterings can be distinctly observed as NSF and SF signals, respectively. Regarding the SF signal, a prominent peak was observed in the AFM phase, which nearly vanished when the temperature reached the PM phase. In contrast, no clear NSF signal was observed in either AFM and PM phases. We extracted the magnetic scattering contribution by subtracting the PM phase data, serving as background, from the AFM phase data, using the same approach as in the unpolarized mode. The resulting magnetic signals are shown in Fig. 6.6 (c). A distinct temperature-dependent variation is evident in the SF signal, while the NSF signal shows no such change. This indicates that the observed variation in reflection intensity with temperature is solely attributed to magnetic scattering.

Rocking curve measurements for this reflection were also performed in the  $P_{zz}$  setting to differentiate between the in-plane and  $c$ -axis components of the magnetic moment. Figure 6.6 (d), (e) and (f) display their profiles in the AFM and PM phases, along with the extracted temperature differences, respectively. Contrary to the results in the  $P_{xx}$  setting, a clear temperature difference was observed only in the NSF mode. The magnetic signal of SF scattering, corresponding to the  $c$ -plane component of the magnetic moment, was not detected within the experiment accuracy ( $\lesssim 0.01 \mu_B$ ), which implies that, for the  $\mathbf{Q} = 0$  component, the magnetic moments are aligned parallel to the  $c$ -axis. These observations are consistent with the results from previous neutron scattering experiments [44, 43, 46] and our RXS experiments. Similar measurements performed on other reflections, such as  $(0, 1, 0)$ ,  $(1, 2, 0)$ , and  $(2, 1, 0)$ , also yielded consistent results.

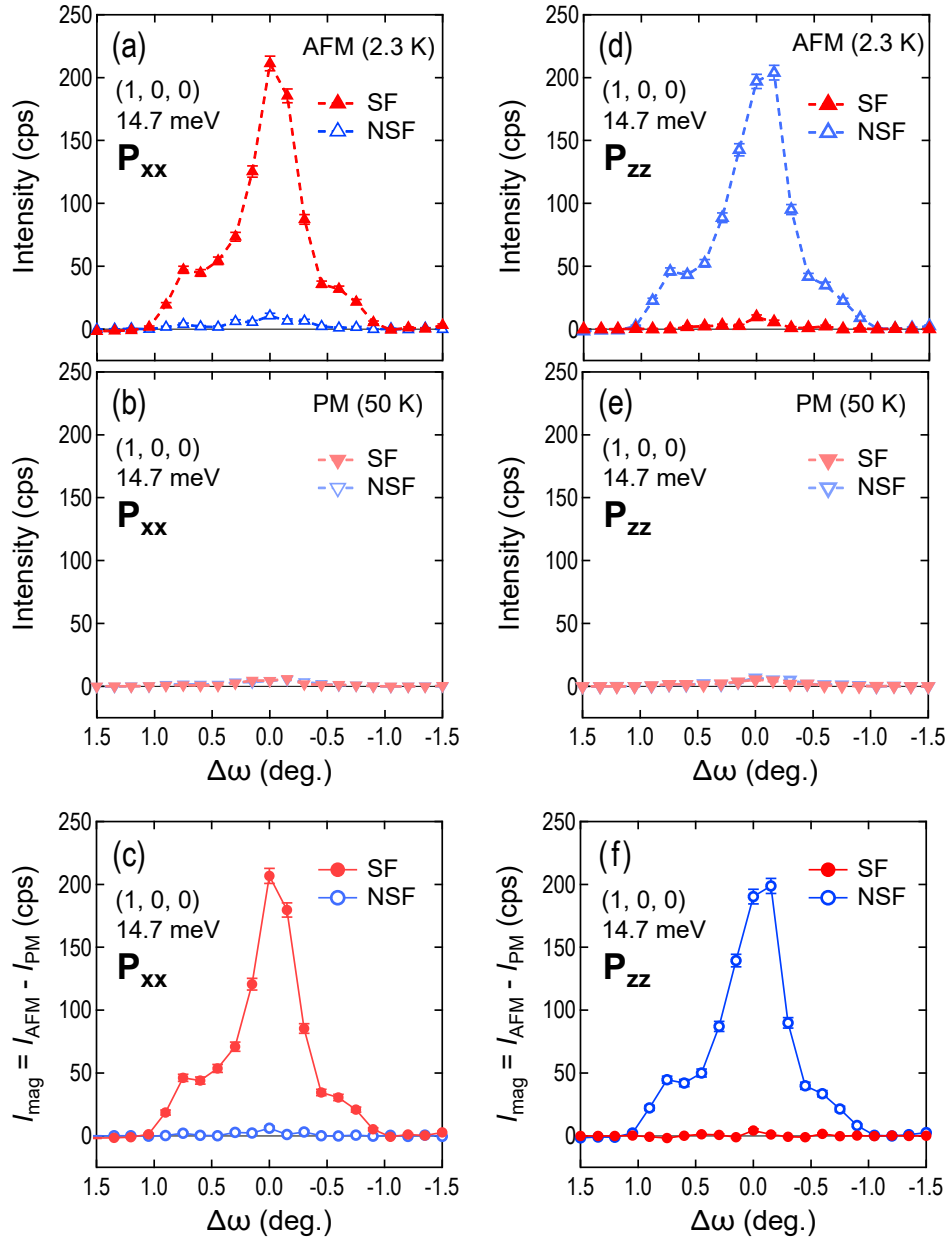


Figure 6.6: (Color online) The peak profiles of SF and NSF scatterings for  $(1, 0, 0)$  reflection, measured in the polarized mode. (a) (d) Data of SF signal (represented by red  $\blacktriangle$  symbols) and NSF signal (blue  $\triangle$  symbols) measured at 2.3 K in the  $P_{xx}$  and  $P_{zz}$  settings. (b) (e) Data of SF signal (red  $\blacktriangledown$  symbols) and NSF signal (blue  $\triangledown$  symbols) measured at 50 K in the  $P_{xx}$  and  $P_{zz}$  settings. (d) (f) Data of SF signal (red  $\bullet$  symbols) and NSF signal (blue  $\circ$  symbols) obtained by subtracting the PM phase data from the AFM phase data in the  $P_{xx}$  setting and  $P_{zz}$  settings.

### 6.2.2 $q_{\text{CDW}}$ reflections

Next, we performed  $h, k$  scans around the reciprocal lattice point  $(2, 0, 0)$  to search for superlattice reflections due to the CDW, in the unpolarized mode at 3 K. Figure 6.7 displays clear superlattice reflections observed at  $(2, q_{\text{CDW}}, 0)$  and  $(2 - q_{\text{CDW}}, 0, 0)$ . There is a marked difference in the scattering intensities of these reflections, the latter being less than one-tenth the intensity of the former. Upon raising the temperature to the PM phase, the already low scattering intensity of the  $(2 - q_{\text{CDW}}, 0, 0)$  reflection diminishes further, while the higher scattering intensity of  $(2, q_{\text{CDW}}, 0)$  largely persists in the PM phase.

Figure 6.8 presents the detailed temperature dependence of the integrated intensities for these reflections, obtained through  $\theta$ - $2\theta$  scans. The scattering intensity of  $(2 - q_{\text{CDW}}, 0, 0)$  is observed to continuously increase below  $T_{\text{N}}$  with a distinct bend. This increase in the intensity is considered to be due to a magnetic scattering resulting from the modulation of the AFM order, similar to the magnetic signal from U 5f moments observed in our previous RXS measurements.

Although the data for the  $(2, q_{\text{CDW}}, 0)$  reflection is somewhat noisy, a similar increase in intensity below around  $T_{\text{N}}$  is apparent. This reflection position of  $(2, q_{\text{CDW}}, 0)$  is, however, precisely where it would be affected by multiple scattering from the strong magnetic reflection at  $(1, 0, 0)$  as shown in Fig. 6.9 (a). Additionally, no signal was observed within the accuracy of experiments performed in the polarized mode using different incident wavelengths as referred in the following part. We can thus conclude that the observed weak temperature variation in the intensity at  $(2, q_{\text{CDW}}, 0)$  is not intrinsic.

The scattering intensities observed in the PM phase (blank blue circles in Figs. 6.7(a) and 6.7(b)) are notable. This is especially significant at  $(2, q_{\text{CDW}}, 0)$  but very weak at  $(2 - q_{\text{CDW}}, 0, 0)$ . In fact, we have ascertained that the latter is an extrinsic signal resulting from multiple scatterings of the nuclear reflection at  $(3, 1, 0)$  as shown in Fig. 6.9 (b). Thus, it can be stated that around  $(2, 0, 0)$ , CDW satellite reflections are observed only in the  $k$  direction. This result aligns with Lee *et al.*'s observations [53], where satellites are detected in the  $k$  direction for  $(h, 0, 0)$  ( $h \neq 0$ ) and in both  $h$  and  $k$  directions for  $(h, k, 0)$  ( $h \neq 0, k \neq 0$ ).

To identify the magnetic modulation structure, we performed rocking curve measurements on the superlattice reflections within the accessible range in the  $(h, k, 0)$  plane and made a quantitative analysis of the magnetic contributions to their integrated intensities. The magnetic scattering intensities observed can be transformed into magnetic structure factors per nuclear unit cell using Eq. (6.1), similar to the  $Q = 0$  case. For the magnetic modulation with  $q_{\text{CDW}}$ , the magnetic structure factor is calculated as follows:

$$|F_{m'}(\boldsymbol{\kappa})| = b_{\text{mag}} \cdot |\boldsymbol{\delta\mu}_{\perp}| \cdot f_{\text{U}}(\boldsymbol{\kappa}) \quad (6.5)$$

(refer to section 4.3 for the details). Here, the amplitude of the magnetic modulation with  $q_{\text{CDW}}$  is denoted as  $|\boldsymbol{\delta\mu}|$ , and the magnitude of its projected component onto the plane perpendicular to  $\boldsymbol{\kappa}$  is  $|\boldsymbol{\delta\mu}_{\perp}|$ .

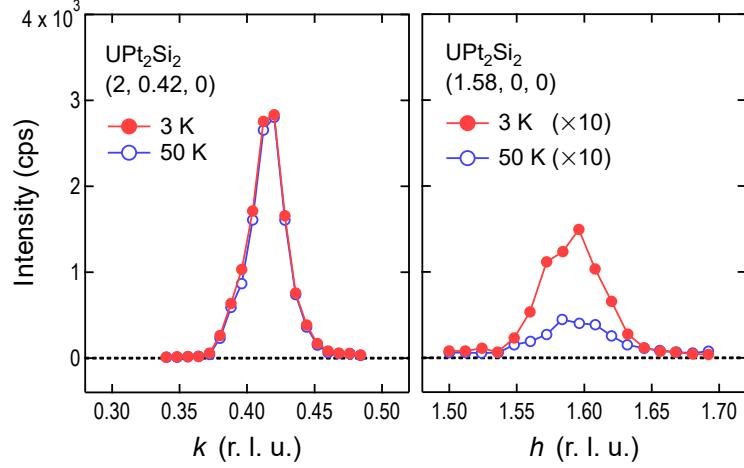


Figure 6.7: (Color online) The diffraction peak profiles for (a)  $k$ -scan and (b)  $h$ -scan measured around the nuclear reflection of  $(2, 0, 0)$  in the unpolarized mode. The filled red symbols denote the data in the AFM phase at 3 K and the blank blue symbols represent the data in the PM phase at 50 K. Note that the vertical axis of graph (b) is scaled to 1/10 of that in (a).

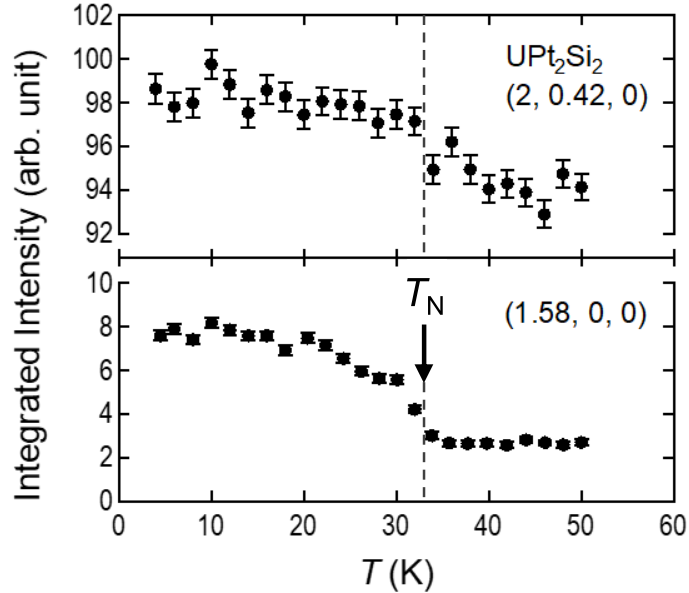


Figure 6.8: The temperature dependence of the integrated intensities obtained in  $\theta$ - $2\theta$  scans for the  $(2, 0.42, 0)$  reflection (upper) and the  $(1.58, 0, 0)$  reflection (lower).

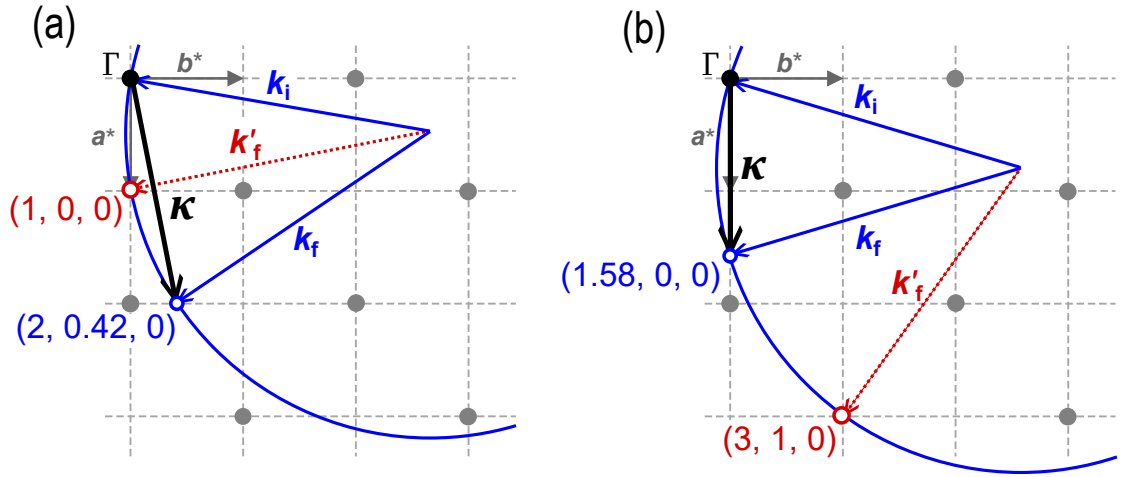


Figure 6.9: (Color online) The Ewald spheres on the  $(hk0)$  plane associated with the reflections at (a)  $(2, 0.42, 0, 0)$  and (b)  $(1.58, 0, 0, 0)$  in the unpolarized mode ( $\lambda = 1.55$ ,  $k = 4.05^{-1}$ ) are represented by blue solid-line circles. The blue thin arrows indicate the wave vectors of the incident ( $\mathbf{k}_i$ ) and scattered ( $\mathbf{k}_f$ ) neutrons in the Bragg conditions for the target reflections. The scattering vectors are denoted by the black bold arrows. The red circle in each panel denotes a reflection present on the Ewald sphere besides the target reflection. Scattering from  $\mathbf{k}_i$  to both  $\mathbf{k}_f$  and  $\mathbf{k}'_f$  occurs simultaneously. Additionally,  $\mathbf{k}'_f$  can cause multiple scattering in the sample, such as diffracting to  $\mathbf{k}_f$  or diffracting back to  $\mathbf{k}_i$  and then to  $\mathbf{k}_f$ . These processes can lead to a non-essential enhancement of the scattering intensity in the target reflections.



To find the orientation of  $\delta\mu$ , we first evaluated the variation of  $|\delta\mu_{\perp}|$  inferred from each reflection intensity with respect to the scattering vector  $\kappa$ . Figure 6.10 (a) displays the data for  $|\delta\mu_{\perp}|$ , derived from the observed magnetic scattering intensities, and plotted as a function of the angle  $\alpha$ . This angle,  $\alpha$ , is defined as the angle between the ordered wavenumber vector  $q_{\text{CDW}}$  and the scattering vector  $\kappa$  at each reflective position, as illustrate in Fig. 6.10 (b). The  $\alpha$  dependence of  $|\delta\mu_{\perp}|$  provides insights into the orientation of the magnetic moment relative to the  $q_{\text{CDW}}$  vector. By comparing the calculations for different magnetic modulation structures, we can identify the actual magnetic structure. For example, in transverse modulation structures within the  $c$ -plane,  $|\delta\mu_{\perp}|$  is proportional to  $\cos \alpha$ , whereas it's proportional to  $\sin \alpha$  in longitudinal magnetic modulations. If we consider a transverse wave modulation structure where only the  $c$ -axis component of magnetic moments undergoes modulation, or a cycloidal structure in the  $c$ -plane,  $|\delta\mu_{\perp}|$  remains constant. Moreover, more intricate structures, like conical modulations, can be understood as combinations of these three scenarios. Our observations show that  $|\delta\mu_{\perp}|$  significantly decreases in a manner consistent with  $\cos \alpha$  as  $\alpha$  increases, aligning well with the transverse magnetic modulation model in the  $c$ -plane. This suggests that the magnetic structure of this system incorporates a transverse magnetic modulation component in the  $c$ -plane, with a periodicity of  $q_{\text{CDW}}$ , leading to a deviation of moments from the  $c$ -axis. This conclusion is consistent with the structure proposed from our RXS experiments.

Figure 6.11 displays a comparison between the structure factor derived from the experimental data and that calculated for the  $c$ -plane transverse magnetic modulation structure. The experimental values, extracted from the observed magnetic scattering intensities, show a good agreement with the calculated ones. This analysis reveals the amplitude of the magnetic modulation to be  $|\delta\mu| = 0.72(2) \mu_{\text{B}}/U$ . Notably, this value exceeds one-third of the amplitude for the  $Q = 0$  component, which is  $1.93(5)/3 \mu_{\text{B}}/U$  as determined in this study. This suggests that the ordered magnetic moments are canted from the  $c$ -axis at a maximum angle of approximately  $20^{\circ}$ .

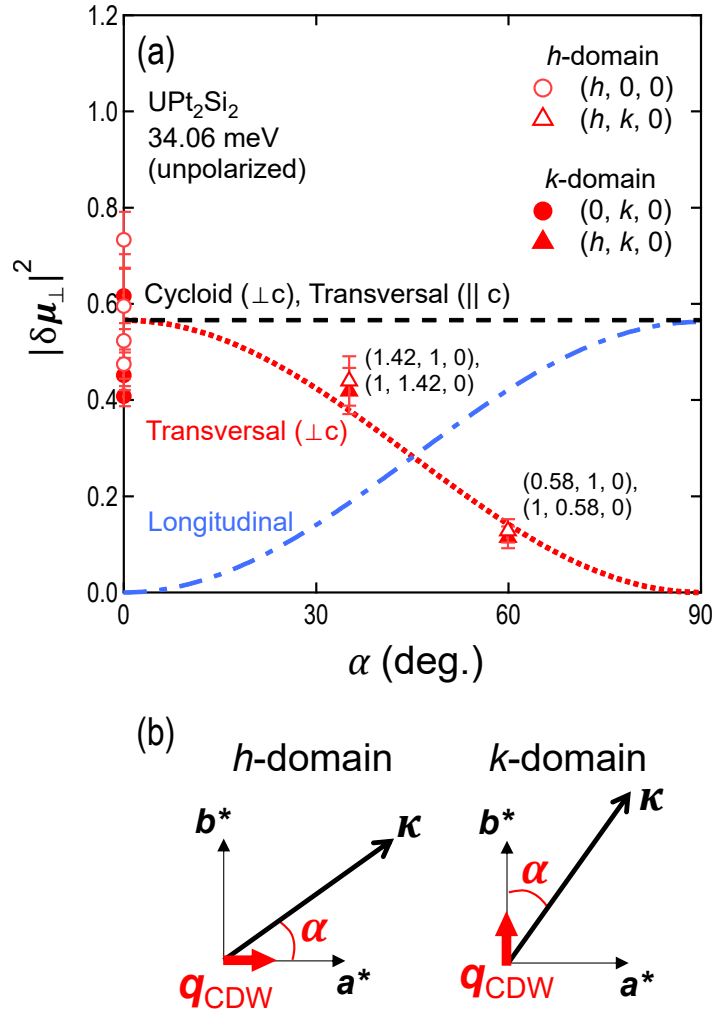


Figure 6.10: (Color online) (a) The  $\alpha$  dependence of the  $|\delta\mu_{\perp}|$ . The red symbols represent data derived from the intensities of magnetic scatterings. The filled symbols and the blank symbols correspond to the reflections of  $h$ -domain and  $k$ -domain, respectively. The curves indicate calculated values for different modulations: the  $c$ -plane transverse modulation (red dotted line), the longitudinal modulation (blue dashed-dotted line), and the cycloid modulation within the  $c$ -plane or the transversal modulation parallel to the  $c$ -axis (black dashed line). (b) The definition of  $\alpha$  for the superlattice reflections of  $h$ -domain and  $k$ -domain.

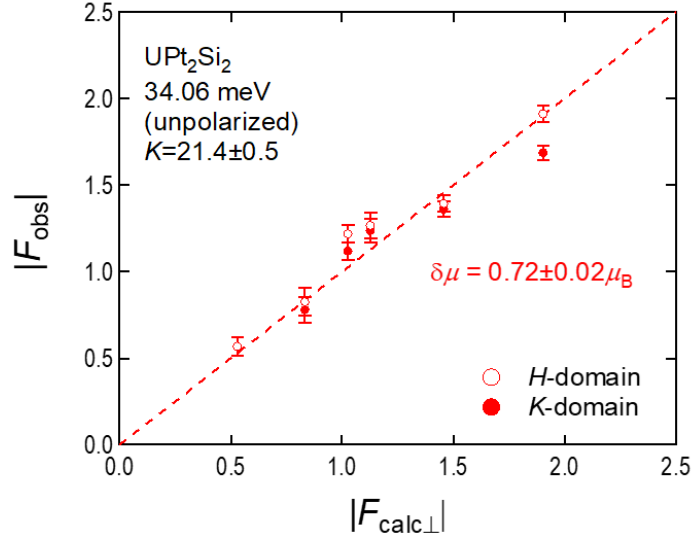


Figure 6.11: (Color online) Comparison of the observed magnetic structure factor  $F_{\text{obs}}$ , derived from magnetic scattering intensities, with the calculated  $F_{\text{calc}\perp}$  assuming the transversal magnetic modulation. Filled symbols and blank symbols represent the reflections of *h*-domain and *k*-domain, respectively. The dashed line denotes  $F_{\text{obs}}/F_{\text{calc}\perp} = 1$ .

To further confirm the determined magnetic modulation structure, rocking curve measurements in the polarized mode were performed for several reflections. Figure 6.14 features a representative profile of the  $(0.42, 0, 0)$  reflection. In the  $P_{xx}$  setup, a broad NSF signal without intensity change across  $T_N$  and a sharp SF signal observable only in the AFM phase are noted (Fig. 6.14 (a)). As per Table 6.1, the former is attributed to nuclear scattering, and the latter to magnetic scattering in this setup. To distinguish between the magnetic modulation contributions along the  $c$ -axis and in the  $c$ -plane in the observed magnetic scattering, the  $P_{zz}$  setting was employed. Here, NSF signals correspond to  $c$ -axis modulation, while SF signals indicate  $c$ -plane modulation. As Fig. 6.14 (b) shows, both NSF and SF signals exhibit no difference from those in the  $P_{xx}$  setting. The temperature dependence of integrated intensities of these signals is detailed in Fig. 6.14 (c). The SF signal is present only below  $T_N$ , while the NSF signal shows no notable temperature variation around  $T_N$ . These observations confirm that the magnetic modulation predominantly involves the  $c$ -plane component of the magnetic moments, with negligible  $c$ -axis component contribution within the experimental accuracy ( $\lesssim 0.01 \mu_B$ ). Similar results are obtained for other  $q_{\text{CDW}}$  superlattice reflections like  $(0.58, 1, 0)$  and  $(1.58, 0, 0)$ .

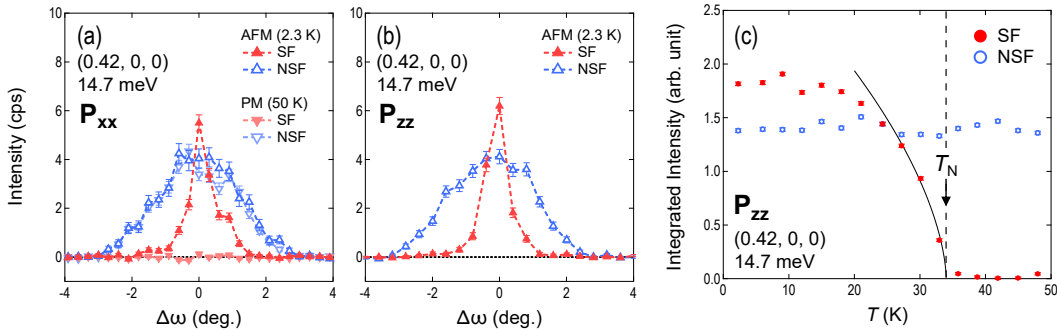


Figure 6.12: (Color online) The peak profiles and the temperature dependence of SF and NSF signals of the  $(0.42, 0, 0)$  reflection measured in the polarized mode. (a) The profiles measured in the  $P_{xx}$  setting at 2.3 K ( $\blacktriangle$  and  $\triangle$ ) and at 50 K ( $\blacktriangledown$  and  $\triangledown$ ). (b) The profiles measured in the  $P_{zz}$  setting at 2.3 K ( $\blacktriangle$  and  $\triangle$ ). (c) The temperature dependence of the integrated intensity measured in the  $P_{zz}$  setting. The red symbols are the data for SF signals and the blank blue symbols are the data for NSF signals. The black curved line is the fitting result for the SF scattering intensity near the  $T_N$  with the equation of  $*$  ( $\beta = 0.3$ ).

As mentioned above, the unpolarized mode, using neutrons with shorter wavelengths, is more prone to multiple reflections and scatterings compared with the polarized mode. Therefore, our discussion on the diffraction patterns of both nuclear and magnetic scatterings in this system primarily relies on the polarized mode results. The obtained patterns are shown in Fig. 6.13(a), with panels (b)–(e) displaying the profiles of the superlattice reflections identified in Fig. 6.13(a). All of these profiles, measured in the  $P_{xx}$  setting, enable us to distinguish between nuclear (NSF) and magnetic (SF)

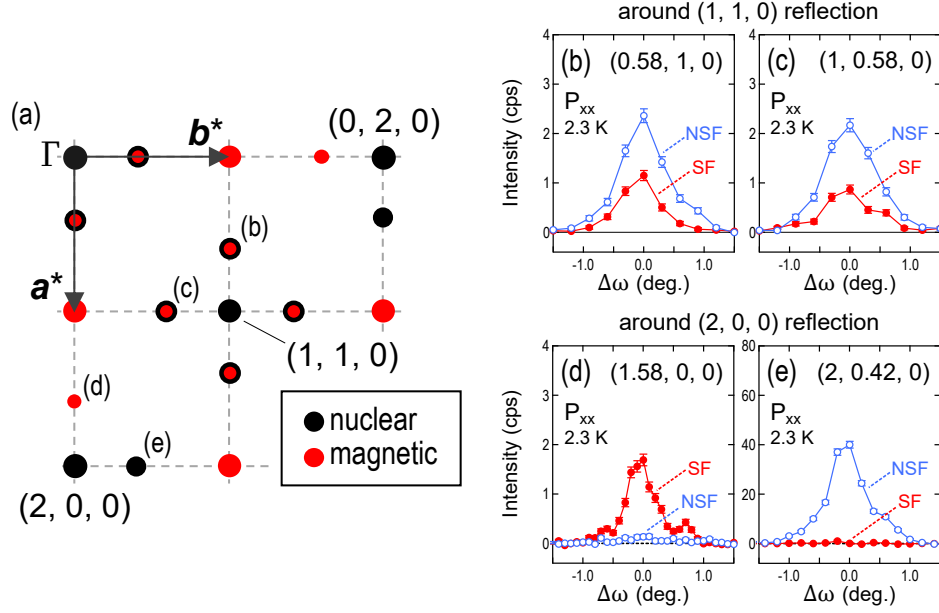


Figure 6.13: (Color online) (a) Map of the diffraction pattern in the  $(hk0)$  plane, drawn on the basis of the results in the polarized mode. The black and red circles indicate the nuclear and magnetic reflections, respectively. (b)–(e) Peak profiles of SF and NSF signals at the superlattice reflections characterized by  $\mathbf{q}_{\text{CDW}}$ , measured in the polarized mode with the  $P_{xx}$  setting. The profiles of the reflections around  $(1, 1, 0)$  and  $(2, 0, 0)$  nuclear Bragg peaks are shown in panels (b), (c) and (d), (e), respectively.

scatterings. Around the  $(1, 1, 0)$  reflection, at 2.3 K, there are  $q_{\text{CDW}}$  superlattice reflections in both  $h$  and  $k$  directions. These contain both NSF and SF signals, as shown in Figs. 6.13(b) and 6.13(c). In contrast, the  $(1.58, 0, 0)$  reflection (Fig. 6.13(d)) shows only the SF signal, indicating magnetic scattering without nuclear scattering contributions within the experimental accuracy. Conversely, the  $(2, 0.42, 0)$  reflection (Fig. 6.13(e)) presents a strong NSF signal but no detectable magnetic scattering. This absence of the magnetic signal is reasonable, since the condition of large values of  $\alpha$  ( $\sim 76^\circ$ ) and  $\kappa$  makes it difficult to detect the  $c$ -plane transverse magnetic modulation. The diffraction pattern of nuclear scatterings is consistent with that reported by Lee *et al* [53]., as mentioned in the main text. In conclusion, the polarized mode confirmed the extrinsic nature of (i) the magnetic signal in the  $(2, 0.42, 0)$  reflection and (ii) the non-magnetic contribution in the  $(1.58, 0, 0)$  reflection, likely caused by multiple scatterings in the unpolarized mode.

### 6.3 Short summary of results in neutron scattering experiments

In this study, we performed the detailed magnetic structure analysis in the AFM phase of  $\text{UPt}_2\text{Si}_2$  and examined the reported magnetic modulation by the CDW. As a result, the signal of magnetic scattering by the  $c$ -plane transverse magnetic modulation with the period of the CDW was observed, which reproduces the result of our previous RXS experiments. From the quantitative analysis of the magnetic scattering intensities, it was found that its amplitude is  $0.72(2) \mu_B$ . This value means that the magnetic moments of U are tilted about  $20^\circ$  from the  $c$ -axis by the CDW. As discussed in later chapters, this result suggests a strong hybridization effect between the 5f electrons of U and the 5d electrons of Pt.

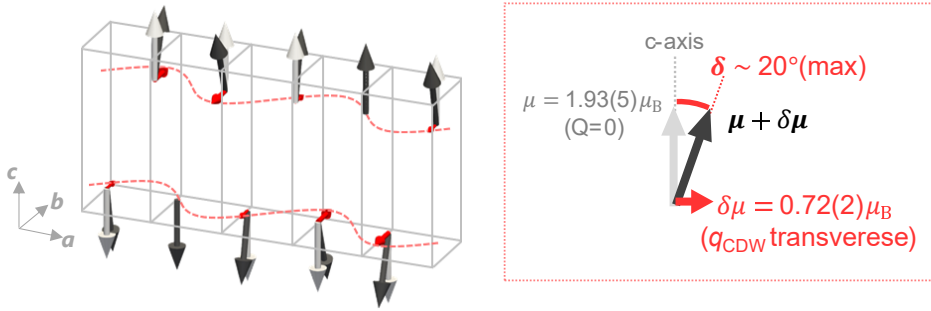


Figure 6.14: (Color online) The obtained structure of the magnetic modulation.

# Chapter 7

## Discussion – UPt<sub>2</sub>Si<sub>2</sub>

### 7.1 Diffraction patterns and modulation types

In this section, the types of satellite reflections observed in the RXS and neutron scattering experiments and the types of corresponding modulations are summarized. To begin with, the symmetry of the crystal structure and the diffraction pattern of the fundamental reflection should be mentioned. The CaBe<sub>2</sub>Ge<sub>2</sub>-type structure belongs to the space group  $P4/nmm$ , which has a primitive tetragonal unit cell. As illustrated in Fig. 7.2(a), it contains two U ions related by the  $n$ -glide symmetry (A- and B-sublattices). In the case of nuclear reflection, the scattered waves from these two sublattices cancel each other for the scattering conditions of  $\boldsymbol{\kappa} = (h, k, 0)$  for  $h + k = \text{odd}$ . Therefore, so the reciprocal lattice points such as  $(2, 1, 0)$  are forbidden. Scattered waves from other elements are also cancelled out in the same way, so that reciprocal lattice points such as  $(2, 1, 0)$  are forbidden. This is a reflection condition arising from the presence of the  $n$ -glide plane perpendicular to the  $c$ -axis.

Here we provide simple examples of magnetic ordered states and explain expected diffraction patterns arising in this structure as a result of electronic orderings and modulations on them. In the case of FM ordering, the reflection condition is maintained because the scattered waves from the two sublattices are in-phase as in the nuclear scattering. Therefore, magnetic scattering contributions are observed on the fundamental lattice reflections (Fig. 7.2(b), top). On the other hand, in the staggered AFM ordering as illustrated in Fig. 7.2(c), the phase of the scattered wave from each sublattice is inverted, thus magnetic reflections are observed at the forbidden positions. When modulation with the wave vector of  $\mathbf{q}$  occurs for these ordered states, satellite peaks appear at different positions. Namely, in the case of modulation on the FM ordered state, satellite peaks with the wavevector  $\mathbf{q}$  appear around the fundamental lattice reflections. Conversely, for the modulation on the AFM ordered state, they appear around the forbidden positions, where the magnetic reflections arise.

In this study, all the signals of the  $c$ -plane magnetic modulation with  $\mathbf{q}_{\text{CDW}}$  (and  $2\mathbf{q}_{\text{CDW}}$ ,  $3\mathbf{q}_{\text{CDW}}$ ) are observed as satellite peaks around the fundamental lattice reflections. Whereas, all signals related to QDW (and  $c$ -axis magnetic modulation) are

observed as satellite peaks around forbidden reflections. An interesting point is that only satellite peaks of QDW are observed in the PM phase. No resonance signal is found at the forbidden positions where the signals of staggered electronic states, which corresponds to the  $\pm\mathbf{m}$  magnetic distribution in the example in Fig. 7.2(c), should be observed.

One possible reason for this is the presence of odd-parity electronic states, as explained below. The polar point group symmetry of  $C_{4v}$  at U site means the presence of an odd-parity CEF, which allows local parity hybridizations as mentioned in Chapter 1. Since the A and B sublattices are connected by an  $n$ -glide symmetry operation, the odd-parity CEFs are inverted between the sublattices. If such parity hybridizations occur in this structure, the resultant odd-parity electronic states should also be staggered. Note that standard RXS experiments, including this study, utilize E1-E1 transitions, where such odd-parity electronic states are unobservable. This means that only the even-parity component of the 5f electronic state in this system is observed as the QDW, and there may be underlying odd-parity electronic states. It is necessary to perform further RXS experiments using the E1-E2 transition to examine this scenario through direct observations of the parity mixed state.



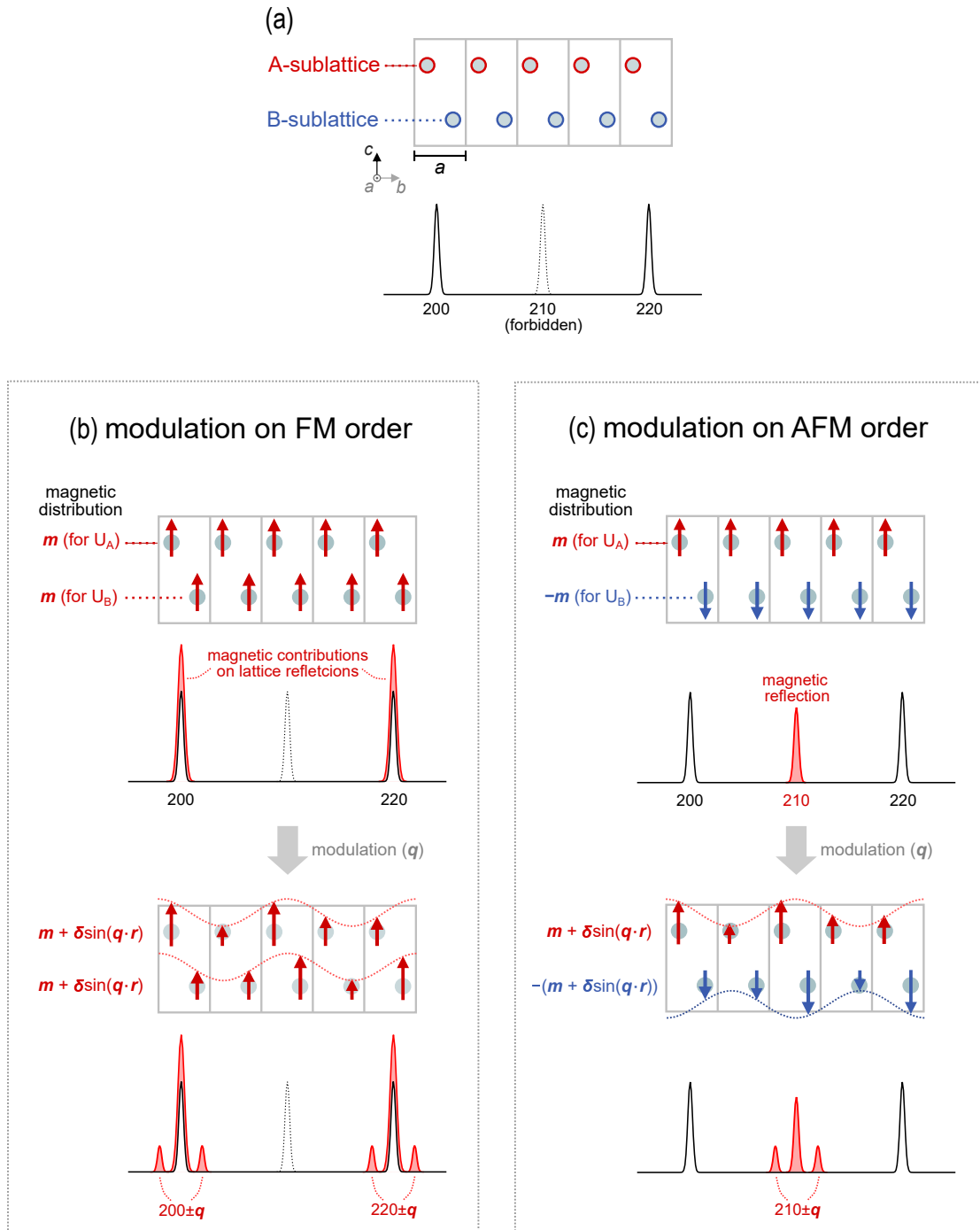


Figure 7.1: (Color online) (a) Schematic drawings of the crystal structure of  $UPt_2Si_2$  and the diffraction pattern of the fundamental lattice reflections. The bold rectangles indicates the primitive unit cell in this crystal structure. The magnetic ordered states and the modulation on them with the propagation vector of  $\mathbf{q}$  are shown for the case of (b) FM order and (c) AFM order. The expected diffraction peaks in each case are also depicted together.

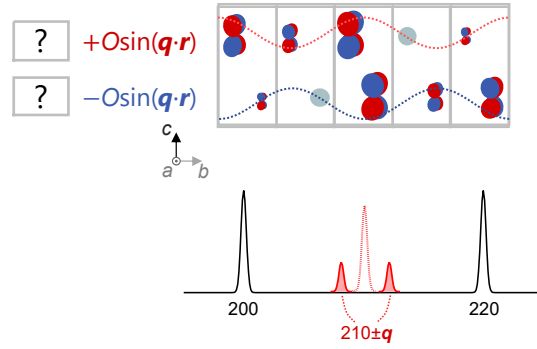


Figure 7.2: (Color online) Schematic drawings of the observed QDW and the diffraction pattern.

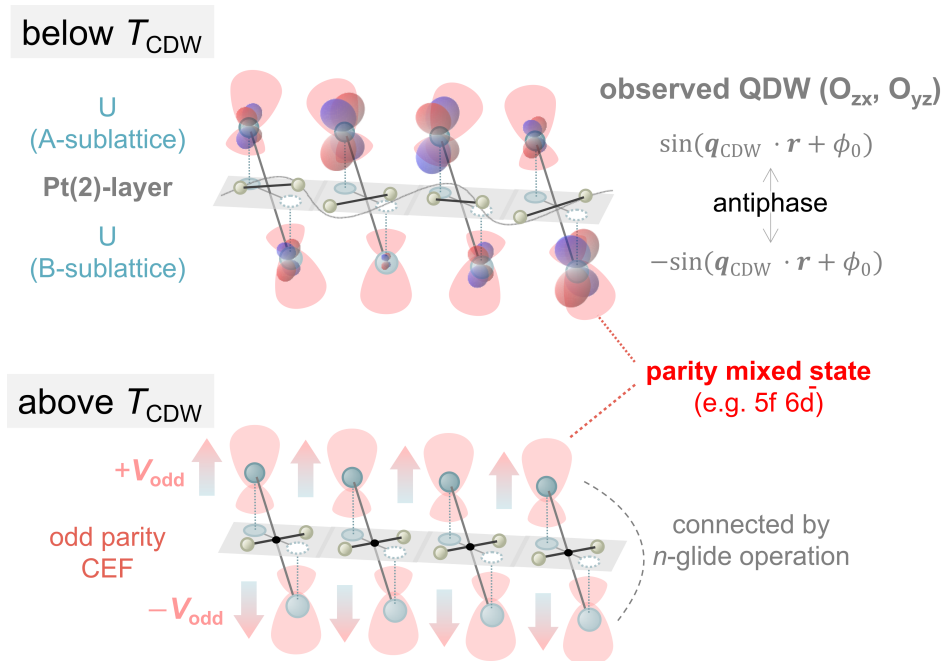


Figure 7.3: (Color online) Illustration of the antiphase QDW observed below  $T_{\text{CDW}}$  and the possible underlying parity mixed states. Pink hatchings schematically illustrate the parity mixed states.

## 7.2 Origin of modulation in 5f electronic states by CDW

Now, we discuss how the CDW induces magnetic modulation in  $\text{UPt}_2\text{Si}_2$ . Similar phenomena have been observed in the 4f electron system of  $\text{TbTe}_3$ [78, 79]. As well as  $\text{UPt}_2\text{Si}_2$ ,  $\text{TbTe}_3$  has a quasi-two-dimensional layered structure, with the 5p electrons of Te forming a CDW order below  $\sim 330$  K and the 4f electrons of Tb undergoing an AFM order below  $\sim 6.6$  K. The AFM structure is modulated with the same period as the CDW, causing the principal axis of the magnetic moment to tilt by up to *sim*  $5^\circ$ . This magnetic modulation is considered to be attributed to the spatial modulation of the CEF levels, impacting the well-localized 4f electrons in Tb. Specifically, the amplitude of modulation in the CEF level splitting is estimated to be about 5 meV, from the RXS measurements [78]. This CEF modulation, involving changes in the shape of the 4f electron orbitals, results in the modulation of the direction of the magnetic moments. Namely, the CDW induces an orbital order of the 4f electrons, which, through spin-orbit interaction, also modulates the magnetic order. The essential element of this scenario is the CEF modulation, which is presumed to arise from the displacement of Te ions and an approximate 0.3% change in the Te-Tb interionic distance associated with the CDW order.

In the case of  $\text{UPt}_2\text{Si}_2$ , a similar scenario might be applicable when viewed from a localized perspective. According to the studies by Lee *et al.* [53], although based on a two-dimensional analysis of limited scattering plane data, the primary displacement in Layer 2 is of Pt(2) atoms, induced by the CDW. The direction of this displacement is mainly in the direction perpendicular to the CDW propagation direction ([100] or [010]), with an amplitude estimated at  $\sim 0.15$  Å. This results in a maximum change of about 3.0% in the U-Pt(2) bond length. However, assuming the valence of Pt ions remains unchanged, the displacement of Pt causes a disarray of at most  $2^\circ$  in the principal axis direction at the U site, which seems insufficient to explain the observed tilt of  $20^\circ$ . Therefore, to explain the experimental results with a CEF model based on effective point charges, a significant reconfiguration of charge among Pt ions adjacent to the  $\mathbf{q}_{\text{CDW}}$  in a perpendicular direction is anticipated. However, no such additional CDW induction in this direction has been observed. By contrast, in  $\text{TbTe}_3$ , although no quantitative discussion has been made regarding the relationship between the CEF modulation and the tilt angle, the emergence of CDW coexisting and orthogonal to the main CDW wave vector at low temperatures is noteworthy.

On the other hand, it is noteworthy that the observed tilt angle of the magnetic moment is roughly aligned with the angle  $\sim 40^\circ$  formed by the bond between Pt(2) and U with the crystallographic *c*-axis. As depicted in Fig. 10.1, the U ions in  $\text{UPt}_2\text{Si}_2$  are in close proximity to four Pt(2) ions located within the same *ac* and *bc* planes, and to four Pt(1) ions positioned at a 45-degree offset. The bond lengths for both are approximately 3.2 Å. Our observations indicate that the magnetic moment tilts from the *c*-axis towards the *b*-axis in response to the  $\mathbf{q}_{\text{CDW}}$  aligned along the *a*-axis. In the CDW state, the displacement of one of the two Pt(2) ions, aligned in the *b*-axis direc-

tion, towards U [53] suggests a selective bonding of the U 5f orbital with this particular Pt. This selective bonding, while competing with the primary AFM correlations, can naturally explain the substantial tilt of the principal axis. The experimental results imply that the d-f hybridization between the four Pt(2) ions and U deviates from the fourfold symmetry of the crystal, favoring a spontaneous bond formation with one specific U-Pt(2) pair.

The above discussion emphasizes the role of hybridization not just as a perturbation but as a crucial component of molecular orbitals, based on the nature of 5f electrons having spatially more extended wavefunctions than 4f electrons. As conceptually illustrated in Fig. 10.1, the d-f hybridization lowers the energy of 5d orbitals to form bonding orbitals, while raising the energy of 5f orbitals to form anti-bonding orbitals. Consequently, the 5f orbitals tend to spread in a direction orthogonal to the U-Pt(2) bond, contributing to stabilization and, as a result, inclining the magnetic moments towards the bond's direction. The actual tilt angle seems to be determined by the competition between this effect and the main antiferromagnetic correlations. Such behavior in solids, akin to molecular orbitals, is often observed in d-electron systems with more extensive wavefunctions, resembling what is known as nematic order. For example, in IrTe<sub>2</sub> [80], the CDW induced by Te 5p electrons modulates the 5d orbitals of Ir through the hybridized bonding orbitals with Te 5p, resulting in the modulation of 5d orbitals (stripe order), similar to the behavior observed in UPt<sub>2</sub>Si<sub>2</sub>.

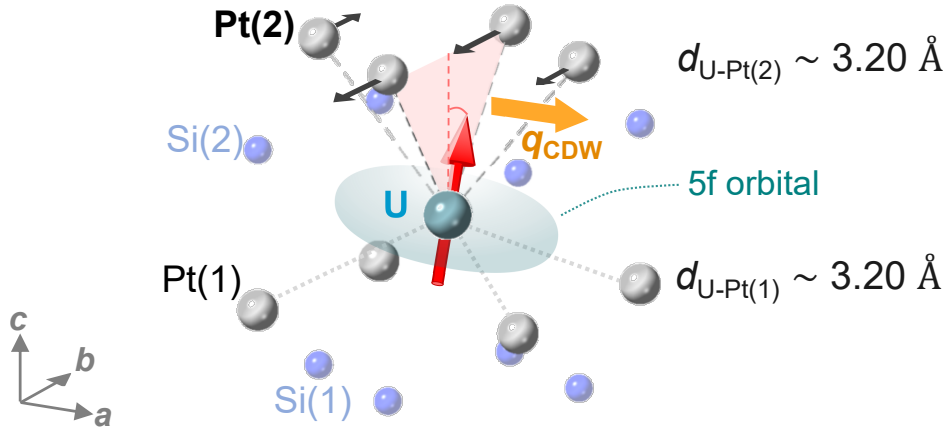


Figure 7.4: (Color online) The environment of U site. The Colored shaded area around the U ion schematically depicts the modulated 5f orbital.

Moreover, it raises a compelling question: does the selective bonding between U and Pt(2) enhance or conflict with the RKKY interaction derived from d-f hybridization? In a localized model, magnetic interactions that establish  $\mathbf{Q} = 0$  order are typically linked to RKKY interactions. However, the specific orbitals of conduction electrons mediating this process remains elusive, even in first-principles calculations [50]. Conversely, the presence of CDW order points to nesting instabilities in the Fermi surface of 5d electrons, thereby fostering favorable conditions for the formation of a spin density wave (SDW) at the same  $\mathbf{q}_{\text{CDW}}$  wave number. This phenomenon

is exemplified in the 4f electron system of  $\text{GdNiC}_2$  [81], where a phase shift in spin density under CDW order gives rise to SDW, possibly correlating with the 4f electron magnetism. Future research, particularly employing RXS of Pt 5d electrons (including under magnetic fields), to explore the existence of SDW associated with Pt 5d and their magnetic interplay with 5f electrons, will offer intriguing insights.

Finally, from the perspective of the itinerant model, the hybridization between U 5f and Pt 5d is interpreted as band hybridization. According to first-principles calculations [50], the 5f orbitals exhibit itinerant characteristics near the Fermi energy, while the 5d electrons of Pt form a valence band centered around  $-4.5\text{eV}$ , but also hybridize with the 5f electrons, contributing to the density of states at the Fermi level. The Fermi surface formed by these hybridized bands reflects the two-dimensional nature of the layered structure. These theoretical calculations were conducted before the discovery of CDW order and do not account for the nesting instabilities of the CDW wave number nor the spontaneous breaking of symmetry in the 5f-5d orbital hybridization. Future studies exploring whether more stable electronic and crystal structures exist near this crystal structure will be a fascinating direction of research.

### 7.3 Atomic displacements

We mention here the relationship between the information on atomic displacements reported in the past and the electron modulation observed in the present study. The atomic displacements in this system have also been discussed in recent pair potential density analyses by Petkov *et al* [54]. According to their study, consistent with the previous reports by Lee *et al.*[53], the primary atomic displacements are attributed to Pt(2), with the magnitude of displacement being approximately 0.15 Å. There are, however, new observations: Firstly, not only Pt(2) but also U undergoes an in-plane displacement of about 0.03 Å. The direction of displacement is not [100] but [110], and although small compared to the in-plane displacement, there is also displacement perpendicular to the plane. Most notably, the displacement, in which the sheets of Pt(2) and U alternately shift in the [110] direction, occurs uniformly at higher temperatures than the CDW, with the CDW further increasing the displacement of Pt ions. No displacements of other atoms have been detected, suggesting that the bond between U and Pt within this crystal structure partially breaks the fourfold symmetry, leading to a partial structural instability. While the details of atomic displacement require further elucidation through precise structural analysis, their analysis supports our inference that the selective bonding between U and Pt(2) brings about the local structural instability.

We also note that the polarized neutron scattering profile at  $\mathbf{q}_{\text{CDW}}$  shown in Fig. 6.14 reveals a significant difference in the peak widths between the SF and NSF scattering modes. This implies that while the NSF signal includes nuclear scattering from all atoms, the SF signal reflects contributions solely from the U atomic layer, indicating that the U layer is relatively undisturbed, whereas the Pt layer forms multiple domain structures, significantly disturbing periodicity. Thus, the experimental results also support the notion that partial structural changes are occurring in  $\text{UPt}_2\text{Si}_2$ . The FWHM of the NSF scattering peak suggests a coherence length perpendicular to  $\mathbf{q}_{\text{CDW}}$  (along the  $b$ -axis direction) of about 160 Å ( $\sim 40a$ ), while the coherence length corresponding to the U atomic layer inferred from SF scattering is estimated to be at least  $\sim 500$  Å ( $> 125a$ ).

### 7.4 Higher harmonics components in the magnetic modulation

In addition, we would like to mention one distinctive feature of  $\text{UPt}_2\text{Si}_2$ : the pattern of modulated charge/spin texture with  $\mathbf{q}_{\text{CDW}}$ ,  $2\mathbf{q}_{\text{CDW}}$  and  $3\mathbf{q}_{\text{CDW}}$ . As summarized at the end of Chapter 5, the transversal magnetic modulation occurs in the odd-harmonics ( $\mathbf{q}_{\text{CDW}}$ ,  $3\mathbf{q}_{\text{CDW}}$ ) while the longitudinal one occurs in the even-harmonics ( $2\mathbf{q}_{\text{CDW}}$ ). These components are not anticipated in typical nonparallel magnetic structures, such as a fan-type, conical-type or helical-type ordering. Such a complexed magnetic modulation with higher harmonics components may rather be described by an analogy of skyrmion crystals which shows CDW order within magnetic ordered states. For ex-

ample, in  $\text{GdRu}_2\text{Si}_2$ , the modulations of the charge density are observed with in their magnetic ordered phases including the skyrmion phase in the spectroscopic-imaging scanning tunneling microscopy measurements [82]. The observed modulation of charge density can be described with the second harmonics of the periodicity of its magnetic ordering. Hayami *et al.* have investigated that such a CDW can be induced by the SDW in itinerant systems from the exchange coupling term of charge and localized-spin in the Kondo lattice model [83]. It is possible that this phenomenon occurs universally in some skyrmion crystals such as  $\text{EuAl}_4$  [84]. Conversely, it is also suggested that SDWs can be induced by a CDWs through this coupling. The possibility of this scenario in the formation of complex spin structures under CDW ordering in  $\text{UPt}_2\text{Si}_2$  is an interesting point to be discussed further in the future.

# Chapter 8

## Low Temperature Physical Properties in UIr<sub>2</sub>Si<sub>2</sub>

### 8.1 Magnetization measurements

The temperature dependences of magnetizations measured in a magnetic fields (0.5 T) parallel to the  $a$ -axis and  $c$ -axis, converted to magnetic susceptibility  $\chi \equiv M/H$ , are shown in Fig 8.1. The magnetizations were measured during heating processes after zero-field-cooling (ZFC). Above 50 K, the magnetic susceptibilities along the  $a$ - and  $c$ -axes ( $\chi_a$ ,  $\chi_c$ ) exhibit comparable values. Both of them show cusp anomalies at 6 K ( $\equiv T_N$ ) and  $\chi_c$  greatly exceeds than  $\chi_a$  below 30 K. These results reproduce previous reports, and indicate that AFM ordering with the ordered moments parallel to the  $c$ -axis occurs below the Néel temperature of 6 K in this system.

Figure 8.2 (a) and (b) show the inverses of  $\chi_c$  and  $\chi_a$ , respectively. We performed the curve fittings on data in the PM phase using the modified Curie-Weiss law (MCW), with a temperature independent term, as in the following equation.

$$\chi = \frac{C}{T - \Theta_W} + \chi_0. \quad (8.1)$$

$\chi_0$  is a temperature independent term which is considered to include the contributions of Pauli paramagnetism of conduction electrons, diamagnetism of core electrons, and a Van-Vleck term of  $5f$  electrons. The effective moment can be calculated from the value of the Curie constant  $C$  in the equation from the following relation,

$$C = \frac{N_A}{3k_B} \mu_{\text{eff}}^2. \quad (8.2)$$

The solid curves in Fig8.2 represent the fitting results for the data within the remperature range of 100-300 K. It is evident that a single law cannot accurately describe the entire PM region. Whereas, the results of MCW fittings in a low-temperature region ( $< 150$  K), shown as the dashed curves, explain their behaviors well. The obtained parameters from MCW fittings are listed in Table 8.1, and it appears that each MCW



parameter varies with temperature, suggesting that the magnetic properties may cross over at around 150 K. The effective moments, estimated from the obtained Curie constants, to be only  $2.32 \mu_B$  (for  $H \parallel a$ ) and  $1.68 \mu_B$  (for  $H \parallel c$ ) are much smaller than the values for magnetic U ions:  $3.62 \mu_B$  ( $U^{3+}$ ) and  $3.58 \mu_B$  ( $U^{4+}$ ). It suggests a reduction on the total orbital magnetic moment due to a splitting in the 5f electronic states, such as CEF splittings for example. The negative  $\Theta_W$  values in the high temperature region mean the presence of AFM correlations in this system. In the low temperature region, its magnitude becomes smaller and even positive for  $H \parallel c$ . This implies the presence of the FM correlations and complexed competing of the magnetic correlations.

Table 8.1: The results of MCW-fitting on  $U\text{Ir}_2\text{Si}_2$  with the fitting range (a)  $100 \text{ K} < T < 300 \text{ K}$  and (b)  $8 \text{ K} < T < 150 \text{ K}$ .

		$H \parallel c$	$H \parallel a$
(a) $100 \text{ K} < T < 300 \text{ K}$	$\mu_{\text{eff}} (\mu_B)$	1.68(1)	2.32(2)
	$\Theta_W (\text{K})$	-42(2)	-93(2)
	$\chi_0 (10^{-4} \text{ m}^3/\text{mol})$	1.48(2)	1.03(2)
		$H \parallel c$	$H \parallel a$
(b) $8 \text{ K} < T < 150 \text{ K}$	$\mu_{\text{eff}} (\mu_B)$	1.200(3)	1.74(1)
	$\Theta_W (\text{K})$	3.34(8)	-41.2(5)
	$\chi_0 (10^{-4} \text{ m}^3/\text{mol})$	2.27(1)	2.04(3)

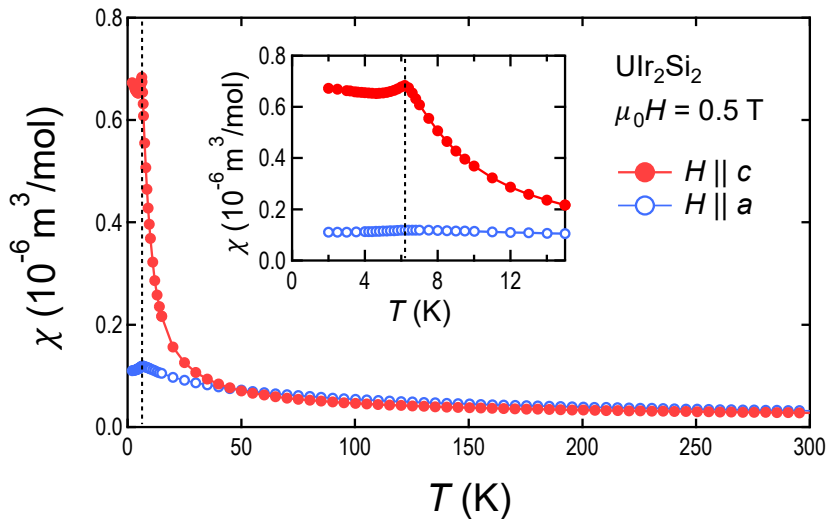


Figure 8.1: (Color online) Magnetic susceptibilities converted from the measured magnetizations under the magnetic field of 0.5 T parallel to the  $c$ - and  $a$ -axes. The inset shows an enlarged view of the magnetic susceptibilities around  $T_N$ .

The magnetic field variations in magnetic properties were investigated in the region of 0.4–7 T. Figure 8.3 (a) displays the temperature dependences of the magnetizations

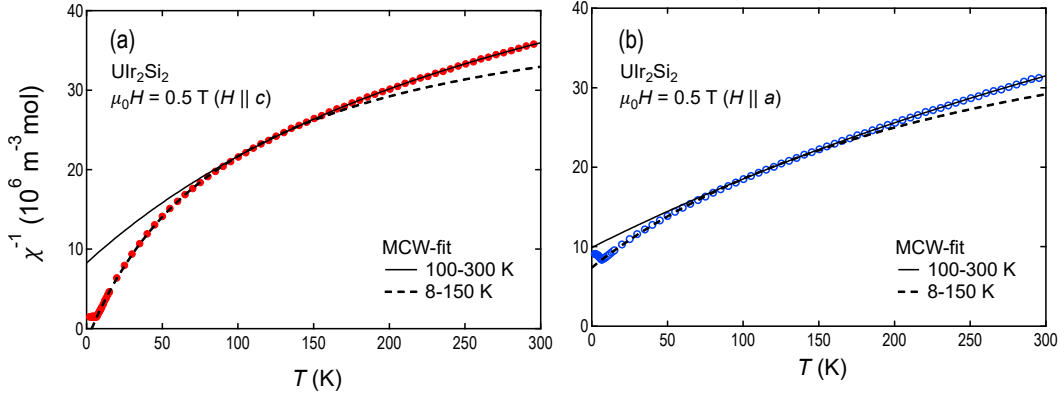


Figure 8.2: (Color online) Inverse magnetic susceptibilities along (a) the  $c$ -axis and (b) the  $a$ -axis. The solid and dashed curves in each panel are the fitting results for the fitting range of 100–300 K and 8–150 K, respectively.

under the magnetic field parallel to the  $c$ -axis ( $M_c(T)$ ), measured in heating processes after ZFC. The cusp anomalies associated with the magnetic phase transitions are suppressed to low temperatures by the magnetic field and completely disappear above 2 T. At 1.8 T, just below the critical field for the AFM order, a characteristic behavior with two local maxima at 2K and 5K was observed. In the region of 1.2–1.85 T, very slight but significant temperature hystereses were observed below  $T_N$  as shown in Fig. 8.3 (b). This suggests that this magnetic transition is characterized by a first-order transition in a part of its phase boundary. The temperature dependences of magnetization under the magnetic field along the  $a$ -axis are shown in Fig. 8.4 (a), and they are smaller than  $M_c(T)$  in all the regions of 0.5–7 T. As displayed in Fig. 8.4 (b),  $\chi_a$  under 0.5 T exhibits a cusp anomaly at 6.2 K and it hardly changes with increasing the magnetic field.

Figure 8.5 shows the magnetization processes measured in isothermal processes at 1.8–6.5 K. Metamagnetic anomalies are observed in the isothermal magnetization process at low temperatures at 1.68 T ( $\equiv \mu_0 H_c$ ) with the magnetization jump about  $0.1 \mu_B/U$ , as already reported in the previous studies. This value is similar to the estimated ordered moment from the previous neutron diffraction measurements. Magnetization shows no saturation even at 7 T and continues to increase gradually. Careful examination reveals that very narrow magnetic-field hysteresis are observed within the AFM phase (Fig. 8.5 (b)), and this hysteresis disappears at 3.5–4 K. This hysteresis region appears to correspond to the region where the temperature hysteresis was observed in  $M_c(T)$ .

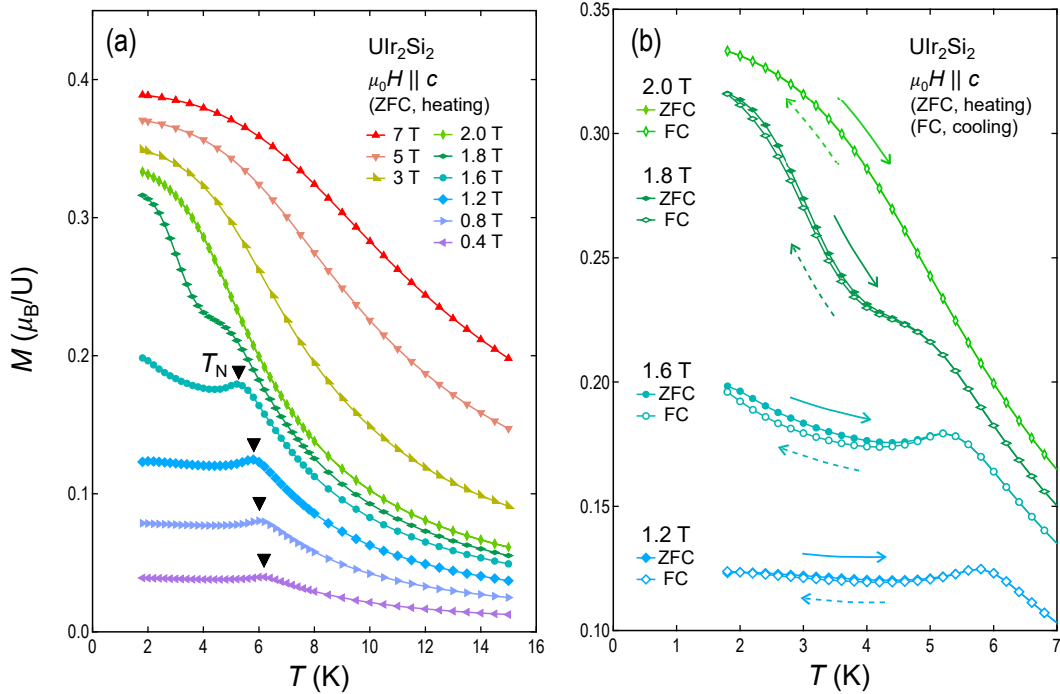


Figure 8.3: (Color online) (a) Temperature dependences of the magnetization under the magnetic field of 0.4–7 T along the  $c$ -axis, measured in a heating process after ZFC. The triangle marker indicates  $T_N$  under each magnetic field, which is evaluated as the temperature of the local maximum in the magnetization. (b) Enlarged magnetizations and the temperature hystereses in the magnetizations. The open symbols represent the data measured in the cooling processes after FC.

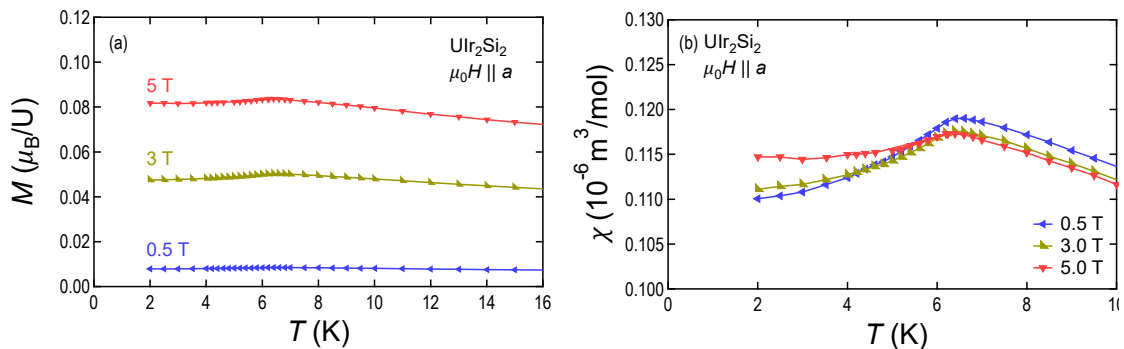


Figure 8.4: (Color online) (a) Temperature dependences of the magnetization under the magnetic field of 0.5–5 T along the  $a$ -axis. (b) The magnetic susceptibilities  $\chi$  converted from the measured magnetizations.

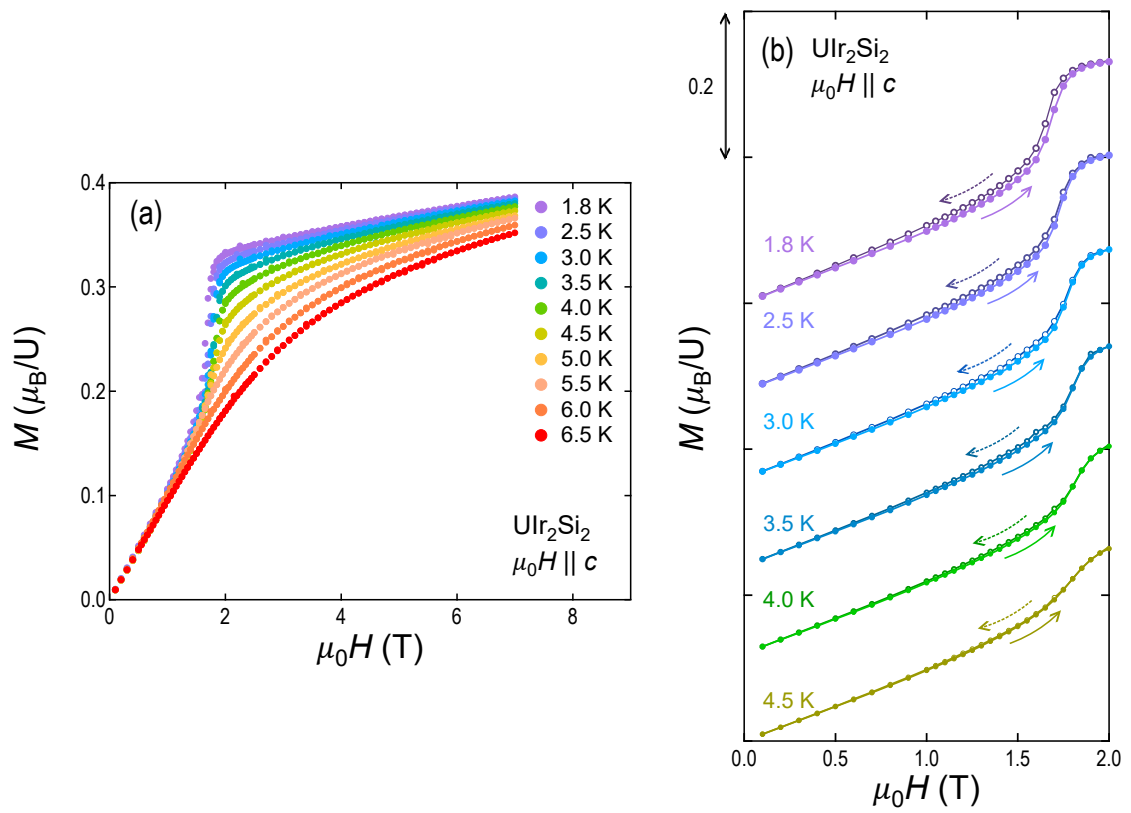


Figure 8.5: (Color online) (a) Isothermal magnetization processes measured under the magnetic field along the  $c$ -axis. (b) Enlarged magnetization processes below 2 T. The open symbols represent the data measured in the sequence of the decreasing magnetic field. The data are vertically shifted for clarity.

## 8.2 Specific heat measurement

The temperature dependence of specific heat of  $\text{UIr}_2\text{Si}_2$   $C(T)$  shown in Fig.8.6 exhibit a clear  $\lambda$ -anomaly at  $T_N$ . The specific heat of non-5f system  $\text{ThIr}_2\text{Si}_2$  reported in the previous study [85] is also shown together in the figure. In the PM phase, the obtained  $C(T)$  can be described by the sum of the  $T$ -linear and  $T^3$ -contributions below  $\sim 30$  K, as shown in the  $C/T$  vs  $T^2$  plot (Fig. 8.7(b)), and we obtained the Debye temperature of about 250 K and the electronic specific heat coefficient  $\gamma = 110(6)$  mJ/K<sup>2</sup>mol. The value of  $\gamma$  is enhanced to about 100 times larger than the value for typical free electrons, suggesting the formation of the HF state. This large specific heat remains even below  $T_N$  as shown in Fig. 8.7 (a). A linear extrapolation below 2 K gives  $\gamma \sim 250$  mJ/K<sup>2</sup>mol, implying the coexistence of the magnetic ordering and the HF state with a further enhanced effective mass.

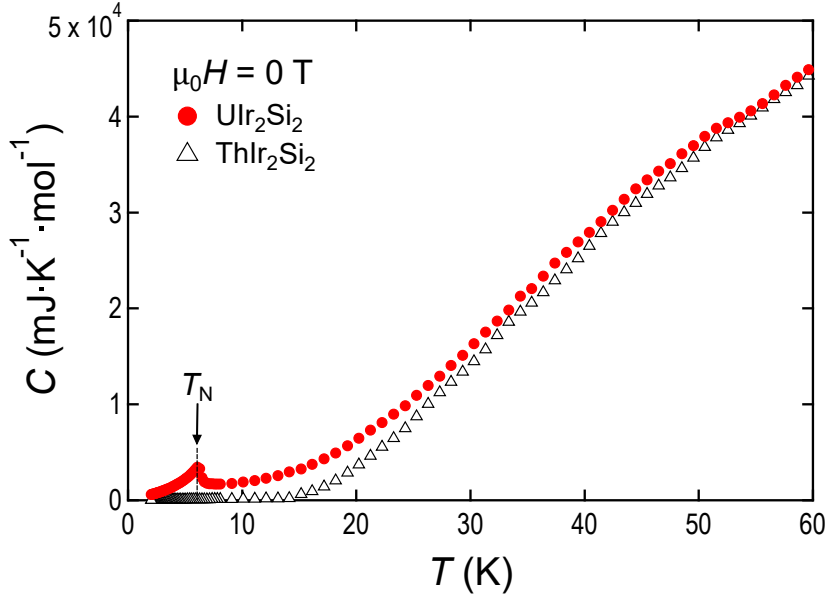


Figure 8.6: (Color online) Temperature dependences of the specific heat measured under zero magnetic field. The solid symbols represent the data of  $\text{UIr}_2\text{Si}_2$  that we measured and the open symbols are the data of  $\text{ThIr}_2\text{Si}_2$  from the previous report by K. Domieracki *et al.* [85]

The 5f electronic contribution in the specific heat of  $\text{UIr}_2\text{Si}_2$   $C_{5f}$  was estimated by subtracting the data of  $\text{ThIr}_2\text{Si}_2$ , and it is plotted in Fig. 8.8 as  $C_{5f}/T$  versus  $T$ . In addition to the  $\lambda$ -anomaly, we also found the broad hump-shaped residual specific heat on the high temperature side of  $T_N$ . This specific heat may be associated to the Schottky anomalies resulting from the splitting of the 5f electronic state and the enhancement in  $\gamma$  value. The integration of  $C_{5f}(T)/T$  gives the 5f electronic entropy  $S_{5f}(T_N) \sim 2.05$  J/Kmol ( $0.37R\ln 2$ ) (Fig. 8.8). This small entropy change associated with the AFM order is also reported in the similar U intermetallic systems, such as  $\text{UIr}_2\text{Ge}_2$  ( $\sim 0.16R\ln 2$ ) [86] and  $\text{UIrSi}_3$  ( $0.14R\ln 2$ ) [87]. The small values of magnetic

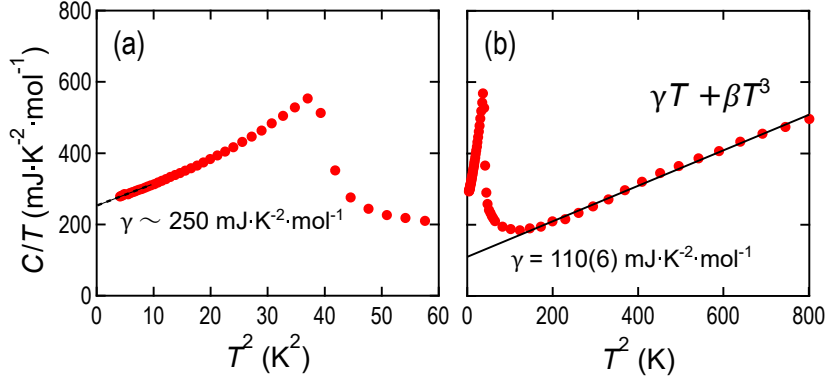


Figure 8.7: (Color online) Specific heat of  $\text{UR}_2\text{Si}_2$  divided by temperature shown in the temperature ranges of (a)  $< \sim 8$  K and (b)  $< \sim 28$  K.

entropy and the large  $\gamma$  value suggest itinerant aspect of the 5f electronic state, which is consistent with the reduced  $\mu_{\text{ord}}$ . Even at the highest temperature 60 K,  $S_{5f}$  is still about  $R\ln 2$ , which indicates the splitting in the 5f electronic states.

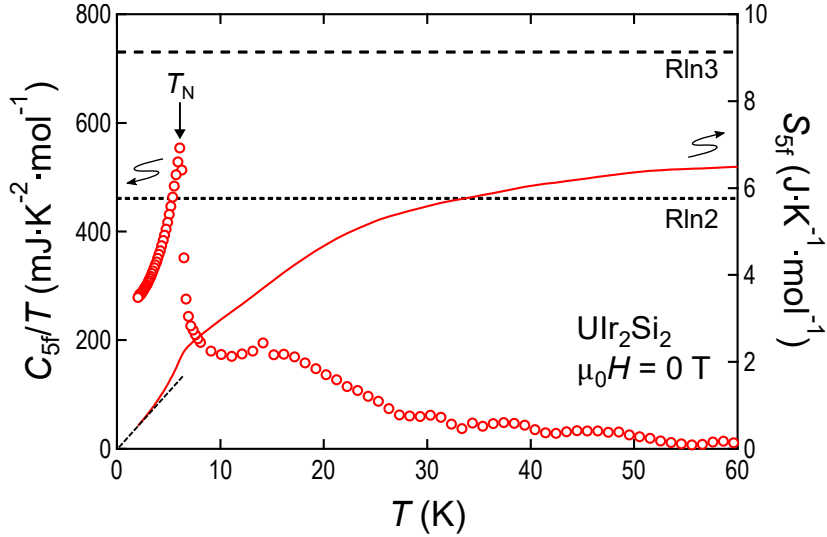


Figure 8.8: (Color online) Contributions of 5f electrons to the specific heat divided by temperature,  $C_{5f}/T$  (open symbols, left axis), and to the entropy,  $S_{5f}$  (bold line, right axis).

To investigate the magnetic field effect on the magnetic transition, we measured the specific heat under magnetic fields (0–12 T) parallel to the  $c$ -axis. Figures 8.9(a) and 8.9(b) display the values of  $C(T)/T$ . As shown in Fig. 8.9(a), the  $\lambda$ -anomaly shifts to lower temperature with increasing magnetic field up to 2 T. However, even at 2 T, which exceeds  $\mu_0 H_c$  estimated from magnetization, it remains as a symmetric and broad anomaly. It is moreover broadened and shifted to higher temperature with increasing magnetic field and remains even under 12 T (Fig. 8.9(a)).

The data  $C(H)$  converted from the data of  $C(T)$  under the magnetic field of 0–12

$T$  are shown in Fig. 8.9. The critical magnetic field of AFM order corresponds well with the field at the maximum value in  $C(H)$  ( $\blacktriangledown$  in the figure). In addition, another local maximum appears on the high field side of the anomaly at the critical field above 5.6 K ( $\nabla$  in the figure). These anomalies appear to correspond to the point of the local maximum in  $C(T)/T$ .

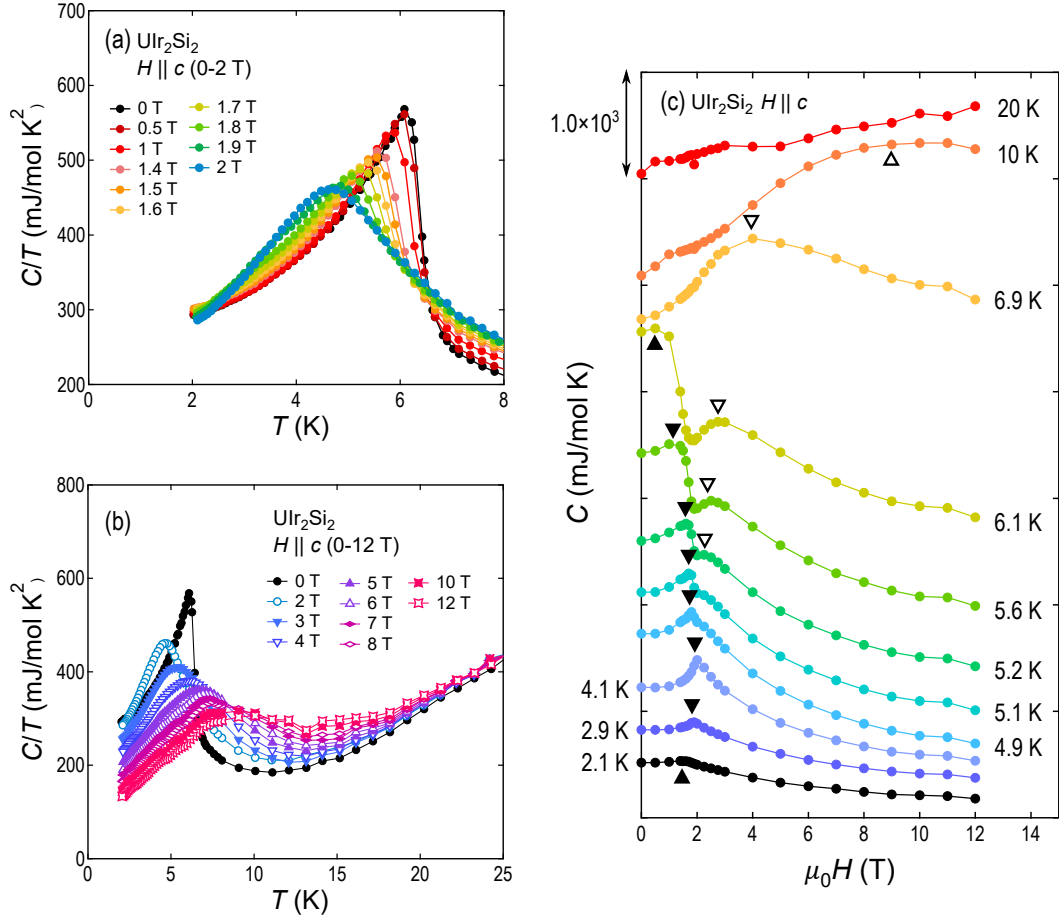


Figure 8.9: (Color online) Specific heats derived by temperature under the magnetic field of (a) 0–2 T and (b) 0–12 T. (c) Magnetic field dependences converted from the measured  $C(T)$  under the magnetic field of 0–12 T applied along the  $c$ -axis. The data are vertically shifted for clarity.

From the anomalies observed in the specific heat and the magnetization, we constructed a  $H$ - $T$  phase diagram for the magnetic field applied parallel to the  $c$ -axis as shown in Fig. 8.10. Both anomalies are well consistent in the region below 2 T, and the phase boundary of the AFM phase is estimated to be as shown in Fig. 8.10(a). Slight temperature and magnetic field hystereses are found in the magnetization at low temperatures and low magnetic field regions, suggesting a first-order magnetic transition. Based on the temperature range where the magnetic field hysteresis was observed in the magnetization process, its region is denoted by the yellow shaded area in Fig. 8.10(a). This suggests the existence of a tri-critical point (TCP) at the position

indicated by the yellow symbol in the figure, which separates the second-order phase transition and the first-order transition. Figure 8.10(b) also shows the temperatures of the anomalies observed as the broad peaks in specific heat under the magnetic field above 2 T. The origins of some of the features found in this phase diagram are discussed in the next chapter.



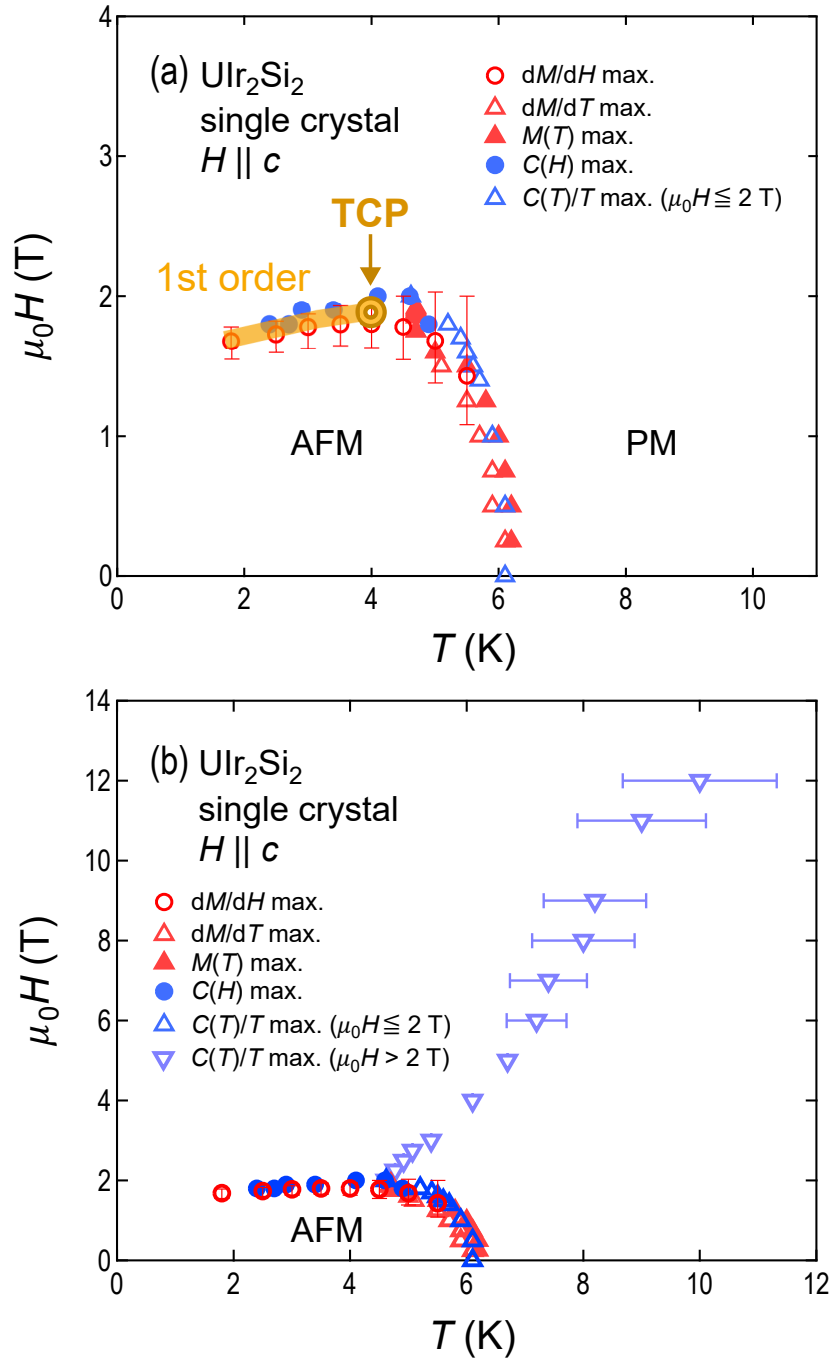


Figure 8.10: (Color online) Phase diagrams obtained from the anomalies observed in the magnetizations and specific heats. (a) is an enlarged view around the AFM phase and (b) is an overall plot including the anomalies observed in the specific heat above 2 T.

# Chapter 9

## Discussion – UIr<sub>2</sub>Si<sub>2</sub>

### 9.1 Tri-critical point on the AFM phase boundary

We have previously confirmed that UIr<sub>2</sub>Ge<sub>2</sub>, which has the same crystal structure as UIr<sub>2</sub>Si<sub>2</sub>, exhibits similar behavior with an AFM phase boundary having a triple critical point. Our measurements of the physical properties for a single crystal of UIr<sub>2</sub>Ge<sub>2</sub> have revealed that it shows an AFM order below  $T_N = 18$  K [86] and The  $H$ - $T$  phase diagram shown in Fig. 9.1. UIr<sub>2</sub>Ge<sub>2</sub> also shows a hysteresis phenomenon in physical quantities in the low-temperature and low-field region, similar to UIr<sub>2</sub>Si<sub>2</sub>, suggesting that the antiferromagnetic-paramagnetic phase transition is of first order in that region. Another point to note is that the magnetic field dependence of  $T_N$  in the presence of a magnetic field is better explained by the 2D Ising model rather than the 3D Ising model.

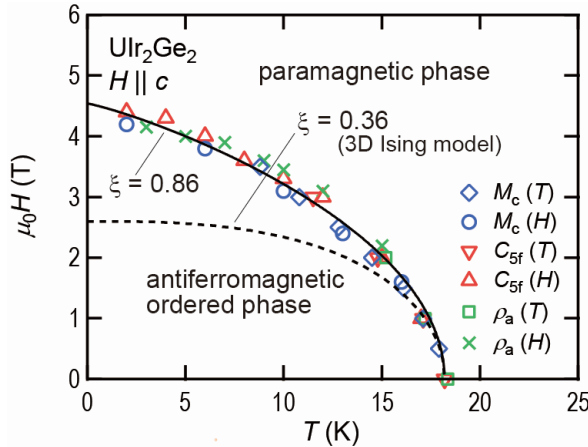


Figure 9.1: (Color online) The magnetic phase diagram of UIr<sub>2</sub>Ge<sub>2</sub> constructed from specific heat, magnetization, and electrical resistivity measurements on a single crystal by our group [86, 88].

On the basis of the observed properties, we propose that the presence of a 2D spin network reflecting the layer structure in CaBe<sub>2</sub>Ge<sub>2</sub>-type crystal structure is the origin

of the TCP in these systems. According to the studies of Ising spin systems by Slotte *et al.* [89] and Jäger *et al.* [90], it is known that a TCP can exist on the AFM phase boundary in a system with a spin-network system on a 2D square lattice as shown in Fig. 9.2(a). Although  $\text{UIr}_2\text{Si}_2$  and  $\text{UIr}_2\text{Ge}_2$  have different magnetic structures, we can find such a spin network in each system. As mentioned in Chapter 2,  $\text{UIr}_2\text{Si}_2$  has the magnetic structure with the propagation vector of  $\mathbf{Q} = 0$ , where ferromagnetic layers are alternately stacked along the  $c$ -axis direction. On the other hand, in  $\text{UIr}_2\text{Ge}_2$ , the propagation vector has been found to be  $\mathbf{Q} = (0, 0, 1/2)$ , where ferromagnetic layers are stacked along the  $c$ -axis in an up-up-down-down pattern [88]. In each magnetic structure, by extracting a bilayer structure consisting of two U layers and projecting it onto the  $c$ -plane, it can be regarded as the 2D spin network exactly as shown in Fig. 9.3. Although it is unclear whether the U bilayer structure includes a Layer1 or Layer2, it is believed that both have strong magnetic interactions ( $J_1$  and  $J_2$ ) within the bilayer structure. It is suggested that the difference in the magnetic structures of the two materials arises from the difference in the interaction ( $J_3$ ) between the bilayer structures, which can be either weak antiferromagnetic or ferromagnetic interactions. This suggests that Layer 1 and Layer 2 have significantly different properties, even though they are composed of the same elements.

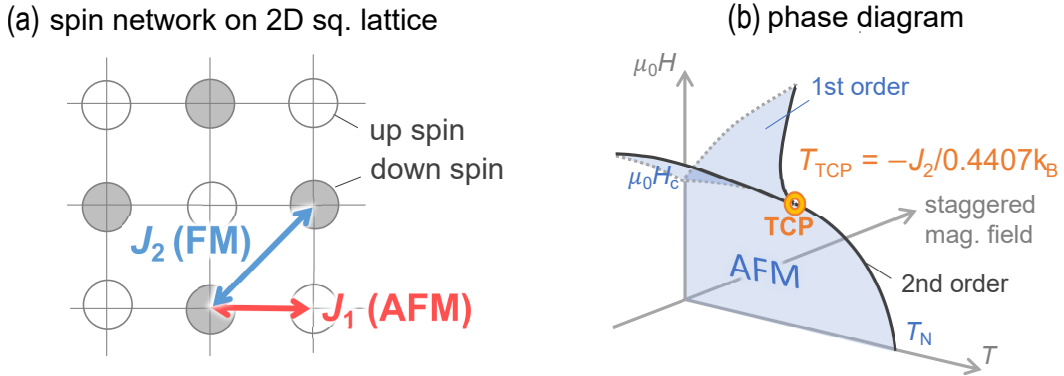


Figure 9.2: (Color online) (a) The spin network on a 2D square lattice discussed in the previous theoretical studies [89, 90]. (b) A schematic drawing of the expected phase diagram for the 2D spin network shown in (a).

## 9.2 5f electronic states in $\text{UIr}_2\text{Si}_2$

In this section, we discuss the interesting features found in the 5f electronic properties. The first is the HF state and its features under the magnetic field. As shown in the previous chapters, the increase in  $\gamma$  was observed, which suggests the formation of a HF state. It is notable that its value appears to increase from the PM phase to the AFM phase. To investigate the properties of the HF state in  $\text{UIr}_2\text{Si}_2$ , the data of  $C(T)/T$  at the lowest temperature plotted against the magnetic field are shown in Fig. 9.4. Above the critical field, it decreases with increasing magnetic field, as seen in

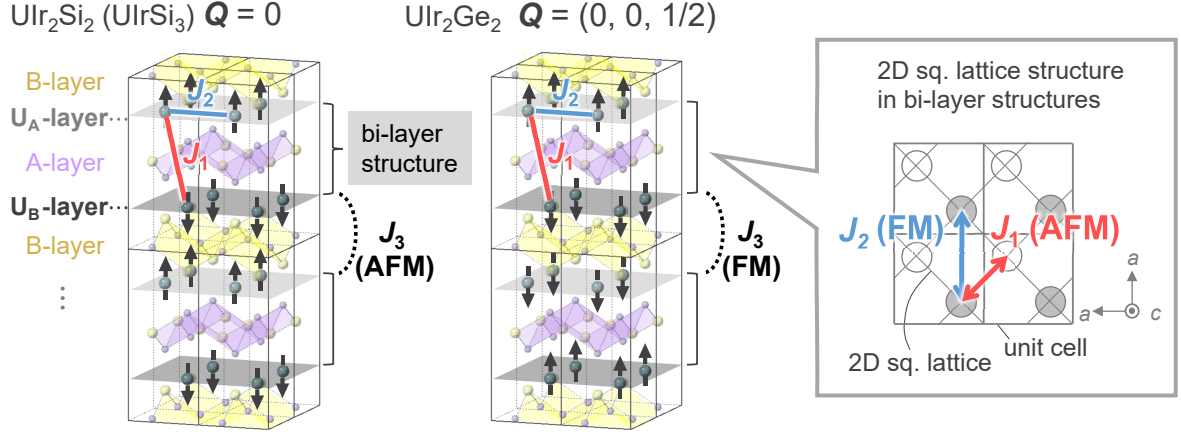


Figure 9.3: (Color online) Spin network in the bilayer structures in  $\text{UIr}_2\text{Si}_2$  and  $\text{UIr}_2\text{Ge}_2$ .

other typical HF systems. Such behavior can be qualitatively understood in terms of the Zeeman splitting of the Kondo resonance. Here, we assume a simple 2-level system with level spacing  $E$ , which can be roughly estimated to be  $\sim 2\mu_z B$  as a result of the Zeeman splitting. The  $\gamma$  value is then expected to show a Lorentz-functional magnetic field dependence as shown in Eq. (9.1) at low temperature limit on the basis of the phenomenological model [91, 92].

$$\gamma = \frac{\pi}{3} \frac{\Delta}{\Delta^2 + E^2} k_B^2 N_A, \quad (9.1)$$

where  $\Delta$  is the width of the Kondo resonance peak. The present experimental data can be qualitatively explained by the following equation with the additional term  $\gamma_0 = 110 \text{ mJ/K}^2\text{mol}$  (solid line in Fig. 9.4).

$$\gamma = A \frac{\Delta}{\Delta^2 + E^2} + \gamma_0, \quad (9.2)$$

where  $A$  is a scale factor and  $\gamma_0$  is a field-independent contribution. This result implies that the HF state with  $\gamma \sim 300 \text{ mJ/K}^2\text{mol}$  was suppressed by the magnetic field, leading to another HF state with  $\gamma \sim 110 \text{ mJ/K}^2\text{mol}$  in the higher magnetic field region. These two HF states appear to correspond to the values of  $\gamma$  in the AFM and paramagnetic phases estimated from  $C(T)/T$  under zero magnetic field.

This increase in effective mass at low temperature and low magnetic field region could be related to the characteristic temperature dependence of the critical magnetic field in the region of the first-order transition. For the first-order phase transition, the Clausius-Clapeyron relationship yields the following equation describing the temperature variation of the critical magnetic field.

$$\mu_0 \frac{dH_c}{dT} = -\frac{\Delta S}{\Delta M} = -\frac{S_{\text{PM}} - S_{\text{AFM}}}{M_{\text{PM}} - M_{\text{AFM}}}, \quad (9.3)$$

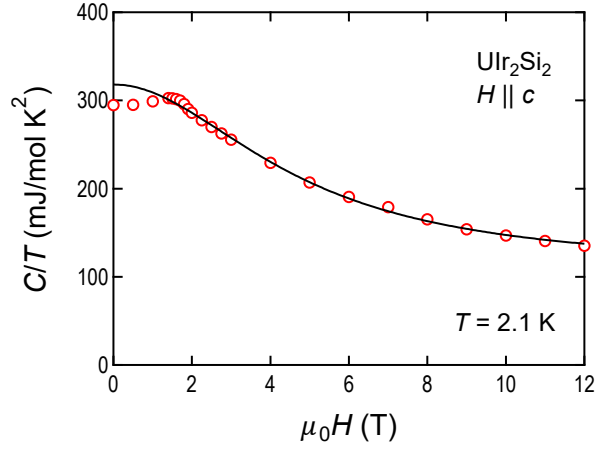


Figure 9.4: (Color online) Magnetic field dependence of specific heat at 2 K converted from the data of  $C(T)$  measured under magnetic fields of 0–12 T.

where  $S_{\text{PM}}$  ( $S_{\text{AFM}}$ ) means the entropy in the PM (AFM) phase and  $M_{\text{PM}}$  ( $M_{\text{AFM}}$ ) means the magnetization in the PM (AFM) phase. This means that the increase in  $\mu_0 dH_c$  with increasing temperature suggests that  $S_{\text{AFM}}$  is larger than  $S_{\text{PM}}$ . In a standard paramagnetic transition, the magnetic entropy should decrease in the phase transition from the AFM ordered state to the PM state. However, in the case of  $\text{UIr}_2\text{Si}_2$ , it is possible that  $S_{\text{AFM}} > S_{\text{PM}}$  reflecting an increase in the effective mass in the low-temperature and low-field region.

Another feature is the broad peak anomaly observed in  $C(T)/T$  above the critical magnetic field. The temperature which the peak occurs,  $T_{\text{max}}$ , increases almost linearly with the magnetic field, and the characteristics of the free-spin Schottky anomaly. Here again, we assume a simple 2-level system and discuss the Zeeman effects on the level splitting. The energy gap between these levels  $E_{\text{gap}}$  can be approximately estimated from  $T_{\text{max}}$ , using the relationship of  $E_{\text{gap}} \sim 3T_{\text{max}}$ . Assuming that  $E_{\text{gap}}$  is caused by the Zeeman effect, the magnetic field change in  $E_{\text{gap}}$  is estimated to be  $\Delta E_{\text{gap}} = 2\mu_z \Delta B$ . On the basis of the field dependence of  $T_{\text{max}}$  in the high field region above 8 T, the value of  $\mu_z$  is roughly estimated as

$$\mu_z \sim \frac{3}{2}(\Delta T_{\text{max}}/\Delta B) \sim 0.8\mu_B. \quad (9.4)$$

This value is comparable to the value of  $\mu_{\text{eff}}$  estimated from the MCW-fitting (1.2–1.7  $\mu_B$ ), but appears to be smaller. This deviation suggests a decrease in the observed value of  $T_{\text{max}}$  compared to that for the free spin model, which is an expected result for the Kondo model, as discussed in HF AFM systems such as  $\text{CeAl}_2$  [93]. The observed Schottky-like anomaly is considered to be associated with the crossover between the Kondo singlet state and the Zeeman split state under magnetic fields.

# Chapter 10

## Concluding remarks

In this work, using diffraction experiments for the decomposition and extraction of CDW effects, we investigated the 5f electronic states in  $\text{UPt}_2\text{Si}_2$  to obtain microscopic information of the environmental effects on the 5f electrons.

Firstly, we performed RXS experiments at the  $M_4$  absorption edge of U on  $\text{UPt}_2\text{Si}_2$  and observed two distinct types of resonance signals from 5f electrons, manifesting as superlattice reflections associated with  $\mathbf{q}_{\text{CDW}}$ . The first is a magnetic signal that develops below  $T_N$  around the fundamental lattice reflection. The second is a non-magnetic signal appearing below  $T_{\text{CDW}}$  around the forbidden positions for this crystal structure, which does not show any temperature variation around  $T_N$ . Detailed measurements of polarization-dependence and azimuth angle-dependence of these signals have revealed that the first signal arises from a transverse magnetic modulation, where the magnetic moments are canted to induce a  $c$ -plane component with the period of the CDW. The latter signal, on the other hand, is attributed to an orbital modulation of 5f electrons, corresponding to attributed to a modulated electric distribution of 5f electrons, including a component of quadrupole density wave.

Secondly, in the study of neutron diffraction experiments on  $\text{UPt}_2\text{Si}_2$ , we thoroughly investigate the magnetic structure of its AFM phase. We reconfirmed the previously reported  $\mathbf{Q} = 0$  AFM order with the ordered magnetic moment estimated to be  $1.93(5) \mu_B/\text{U}$ , aligned parallel to the  $c$ -axis within an experimental accuracy of  $\sim 0.01 \mu_B/\text{U}$ . Moreover, we observed nuclear scattering corresponding to atomic displacements induced by the CDW order and magnetic modulation waves occurring at the same periodicity as the CDW. These findings are in line with our previous RXS experiments. A significant new insight gained was the amplitude of the magnetic modulation, determined to be  $0.72(2) \mu_B/\text{U}$ , suggesting a tilting of U magnetic moments by about  $20^\circ$  due to the CDW influence. The CDW-induced average structural changes in the Pt(2) atoms are found to be small, suggesting that the tilting of 5f electron orbitals cannot be simply explained.

Based on these results, we propose that selective hybridization between U 5f electrons and adjacent Pt(2) 5d electrons spontaneously breaks the fourfold symmetry of 5f orbitals, significantly tilting their principal axis. In addition to such inter-site mixing effects, we also propose the possibility of intra-site hybridization effects. The observed

antiphase orbital modulation in the RXS experiments is expected as a result of this selective inter-site hybridization with only Layer 2 of the two layers sandwiching the U-layer. This means that, simultaneously, the 5f electrons ‘feel’ the polar environment at the U site lacking the local inversion symmetry. That is precisely the situation where parity mixed states on a single ion site, which have not been found in the f-electron systems, can appear through an intra-site hybridization.

The detailed and microscopic information obtained in this study is expected to contribute to the advancement of future research on hybridization effects. Specifically, the information on symmetry is important for group theory considerations, and the quantitative data is important for comparison with model calculations, including first-principles calculations.

In terms of future experimental work, precise structural analysis using hard X-ray is necessary. In addition, direct observation of Pt 5d and U 6d electron orbitals through RXS, including the high-temperature range above  $T_{\text{CDW}}$ , are anticipated to provide further insights. Particularly, direct observation of intra-site parity hybridization is unprecedented and challenging, but it is expected to provide important new information on 5f electronic states in solids.

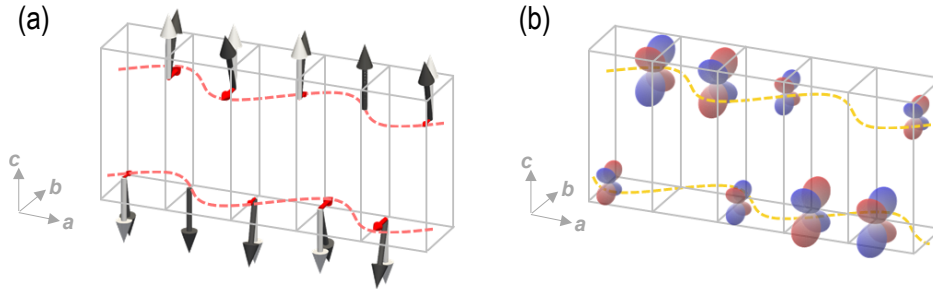


Figure 10.1: (Color online) The Schematic illustrations of (a) the magnetic modulation and (b) the orbital modulation.

In addition to  $\text{UPt}_2\text{Si}_2$ , the 5f electronic state in  $\text{UIr}_2\text{Si}_2$ , which has the same crystal structure, was investigated in detail by means of magnetization and specific heat measurements under magnetic fields, and the  $H$ - $T$  phase diagram of this system was obtained. The results reveals that the AFM phase boundary shows a characteristic feature with  $dH_c(T)/dT > 0$  as  $T \rightarrow 0$ , possessing a TCP at  $\sim 4$  K ( $\sim 2$  T). From comparison with a similar system,  $\text{UIr}_2\text{Ge}_2$ , we discussed the possibility of the formation of a 2D spin network reflecting the layer structure in the  $\text{CaBe}_2\text{Ge}_2$ -type structure.

One of the intriguing features of  $\text{UIr}_2\text{Si}_2$  is the formation of HF states with two distinct energy scales as the temperature decreases. The temperature dependence of the specific heat shows an increases in the effective mass of conduction electrons, from the corresponding  $\gamma$  value, of  $110$   $\text{mJ}/\text{K}^2\text{mol}$  in the paramagnetic phase to  $280$   $\text{mJ}/\text{K}^2\text{mol}$  in the AFM phase. The specific heat at the lowest temperature decreases with magnetic field, suggesting the suppression of the HF state by magnetic field. The observed broad peak anomalies in the specific heat above  $2$  T imply a competition

between the Kondo effect and the Zeeman effect under the magnetic field in this system. The origin of these characteristics in the HF states still remains unclear. It is necessary to discuss these issues in detail by investigating the 5f electronic states in this system using microscopic techniques similar to the studies conducted on  $\text{UPt}_2\text{Si}_2$ .



# REFERENCES

- [1] S. Doniach: *Physica B+ C* **91** (1977) 231.
- [2] S. Yotsuhashi, H. Kusunose, and K. Miyake: *J. Phys. Soc. Jpn.* **70** (2001) 186.
- [3] C. Geibel, C. Schank, S. Thies, H. Kitazawa, C. Bredl, A. Böhm, M. Rau, A. Grauel, R. Caspary, R. Helfrich, et al.: *Zeitschrift für Physik B Condensed Matter* **84** (1991) 1.
- [4] N. K. Sato, N. Aso, K. Miyake, R. Shiina, P. Thalmeier, G. Varelogiannis, C. Geibel, F. Steglich, P. Fulde, and T. Komatsubara: *Nature* **410** (2001) 340.
- [5] 糟谷忠雄: *日本物理学会誌* **42** (1987) 722.
- [6] H. Nakao, K.-i. Magishi, Y. Wakabayashi, Y. Murakami, K. Koyama, K. Hirota, Y. Endoh, and S. Kunii: *J. Phys. Soc. Jpn.* **70** (2001) 1857.
- [7] K. Kubo and Y. Kuramoto: *J. Phys. Soc. Jpn.* **73** (2004) 216.
- [8] H. Kusunose and S. Hayami: *J. Phys.: Condens. Matter* **34** (2022) 464002.
- [9] S. Hayami, M. Yatsushiro, Y. Yanagi, and H. Kusunose: *Phys. Rev. B* **98** (2018) 165110.
- [10] S. Hayami, H. Kusunose, and Y. Motome: *Phys. Rev. B* **90** (2014) 024432.
- [11] M.-T. Suzuki, T. Koretsune, M. Ochi, and R. Arita: *Phys. Rev. B* **95** (2017) 094406.
- [12] H. Watanabe and Y. Yanase: *Phys. Rev. B* **98** (2018) 245129.
- [13] S. A. M. Mentink, A. Drost, G. J. Nieuwenhuys, E. Frikkee, A. A. Menovsky, and J. A. Mydosh: *Phys. Rev. Lett.* **73** (1994) 1031.
- [14] H. Saito, K. Uenishi, N. Miura, C. Tabata, H. Hidaka, T. Yanagisawa, and H. Amitsuka: *J. Phys. Soc. Jpn.* **87** (2018) 033702.
- [15] S. Hayami, Y. Yanagi, and H. Kusunose: *Phys. Rev. B* **102** (2020) 144441.
- [16] J.-I. Yamaura and Z. Hiroi: *Journal of the Physical Society of Japan* **71** (2002) 2598.

- [17] S. Hayami, Y. Yanagi, H. Kusunose, and Y. Motome: Phys. Rev. Lett. **122** (2019) 147602.
- [18] S. Hayami and H. Kusunose: J. Phys. Soc. Jpn. **87** (2018) 033709.
- [19] H. Kusunose, R. Oiwa, and S. Hayami: J. Phys. Soc. Jpn. **89** (2020) 104704.
- [20] N. T. Huy, A. Gasparini, D. E. de Nijs, Y. Huang, J. C. P. Klaasse, T. Gortemulder, A. de Visser, A. Hamann, T. Görlach, and H. v. Löhneysen: Phys. Rev. Lett. **99** (2007) 067006.
- [21] D. Aoki, A. Huxley, E. Ressouche, D. Braithwaite, J. Flouquet, J.-P. Brison, E. Lhotel, and C. Paulsen: Nature **413** (2001) 613.
- [22] A. Huxley, I. Sheikin, E. Ressouche, N. Kernavanois, D. Braithwaite, R. Calemczuk, and J. Flouquet: Phys. Rev. B **63** (2001) 144519.
- [23] D. Aoki and J. Flouquet: J. Phys. Soc. Jpn. **83** (2014) 061011.
- [24] S. Ran, C. Eckberg, Q.-P. Ding, Y. Furukawa, T. Metz, S. R. Saha, I.-L. Liu, M. Zic, H. Kim, J. Paglione, and N. P. Butch: Science **365** (2019) 684.
- [25] G. R. Stewart, Z. Fisk, J. O. Willis, and J. L. Smith: Phys. Rev. Lett. **52** (1984) 679.
- [26] K. Hasselbach, L. Taillefer, and J. Flouquet: Phys. Rev. Lett. **63** (1989) 93.
- [27] H. R. Ott, H. Rudigier, Z. Fisk, and J. L. Smith: Phys. Rev. Lett. **50** (1983) 1595.
- [28] G. E. Volovik and L. P. Gorkov: JETP lett **39** (1984) 550.
- [29] H. R. Ott, H. Rudigier, Z. Fisk, and J. L. Smith: Phys. Rev. B **31** (1985) 1651.
- [30] R. H. Heffner, J. L. Smith, J. O. Willis, P. Birrer, C. Baines, F. N. Gygax, B. Hitti, E. Lippelt, H. R. Ott, A. Schenck, et al.: Phys. Rev. Lett. **65** (1990) 2816.
- [31] T. T. M. Palstra, A. A. Menovsky, J. van den Berg, A. J. Dirkmaat, P. H. Kes, G. J. Nieuwenhuys, and J. A. Mydosh: Phys. Rev. Lett. **55** (1985) 2727.
- [32] M. B. Maple, J. W. Chen, Y. Dalichaouch, T. Kohara, C. Rossel, M. S. Torikachvili, M. W. McElfresh, and J. D. Thompson: Phys. Rev. Lett. **56** (1986) 185.
- [33] W. Schlabitz, J. Baumann, B. Pollit, U. Rauchschwalbe, H. M. Mayer, U. Ahlheim, and C. D. Bredl: Z. Phys., B., Condens. matter (1993) 89.
- [34] J. A. Mydosh, P. M. Oppeneer, and P. S. Riseborough: J. Phys.: Condens. Matter **32** (2020) 143002.

- [35] S. Kambe, Y. Tokunaga, H. Sakai, T. Hattori, N. Higa, T. D. Matsuda, Y. Haga, R. E. Walstedt, and H. Harima: *Phys. Rev. B* **97** (2018) 235142.
- [36] H. Harima: *SciPost Physics Proceedings* (2023) 006.
- [37] S. Hayami and H. Kusunose: *J. Phys. Soc. Jpn.* **92** (2023) 113704.
- [38] D. Aoki, J.-P. Brison, J. Flouquet, K. Ishida, G. Knebel, Y. Tokunaga, and Y. Yanase: *J. Phys.: Condens. Matter* **34** (2022) 243002.
- [39] A. Amon, I. Zelenina, P. Simon, M. Bobnar, M. Naumann, E. Svanidze, F. Arnold, H. Borrmann, U. Burkhardt, W. Schnelle, et al.: *Scientific Reports* **8** (2018) 10654.
- [40] 田端千紘: Dr. Thesis, 北海道大学, 理学院 (物性物理学専攻) (2016).
- [41] T. Endstra, G. J. Nieuwenhuys, and J. A. Mydosh: *Phys. Rev. B* **48** (1993) 9595.
- [42] E. Parthé, B. Chabot, H. F. Braun, and N. Engel: *Acta Crystallographica Section B: Structural Science* **39** (1983) 588.
- [43] H. PtasiwiczBąk, J. Leciejewicz, and A. Zygmunt: *Solid State Commun.* **55** (1985) 601.
- [44] R. A. Steeman, E. Frikkee, S. A. M. Mentink, A. A. Menovsky, G. J. Nieuwenhuys, and J. A. Mydosh: *J. Phys.: Condens. Matter* **2** (1990) 4059.
- [45] H. Amitsuka, T. Sakakibara, K. Sugiyama, T. Ikeda, Y. Miyako, M. Date, and A. Yamagishi: *Physica B: Cond. Matter* **177** (1992) 173.
- [46] S. Süllow, A. Otop, A. Loose, J. Klenke, O. Prokhnenko, R. Feyerherm, R. W. A. Hendrikx, J. A. Mydosh, and H. Amitsuka: *J. Phys. Soc. Jpn.* **77** (2008) 024708.
- [47] A. J. Dirkmaat, T. Endstra, E. A. Knetsch, G. J. Nieuwenhuys, J. A. Mydosh, A. A. Menovsky, F. R. de Boer, and Z. Tarnawski: *Phys. Rev. B* **41** (1990) 2589.
- [48] R. A. Steeman, E. Frikkee, C. van Dijk, G. J. Nieuwenhuys, and A. A. Menovksy: *J. Magn. Magn. Mater.* **76-77** (1988) 435.
- [49] G. J. Nieuwenhuys: *Phys. Rev. B* **35** (1987) 5260.
- [50] S. Elgazzar, J. Rusz, P. M. Oppeneer, and J. A. Mydosh: *Phys. Rev. B* **86** (2012) 075104.
- [51] J. Lee, M. Matsuda, J. A. Mydosh, I. Zaliznyak, A. I. Kolesnikov, S. Süllow, J. P. Ruff, and G. E. Granroth: *Phys. Rev. Lett.* **121** (2018) 057201.
- [52] M. Bleckmann, A. Otop, S. Süllow, R. Feyerherm, J. Klenke, A. Loose, R. W. A. Hendrikx, J. A. Mydosh, and H. Amitsuka: *J. Magn. Magn. Mater.* **322** (2010) 2447.

- [53] J. Lee, K. Prokeš, S. Park, I. Zaliznyak, S. Dissanayake, M. Matsuda, M. Frontzek, S. Stoupin, G. L. Chappell, R. E. Baumbach, C. Park, J. A. Mydosh, G. E. Granroth, and J. P. C. Ruff: *Phys. Rev. B* **102** (2020) 041112(R).
- [54] V. Petkov, R. Baumbach, A. M. M. Abeykoon, and J. A. Mydosh: *Phys. Rev. B* **107** (2023) 245101.
- [55] T. Aoyama, T. Kubo, H. Matsuno, H. Kotegawa, H. Tou, A. Mitsuda, Y. Nagano, N. Araoka, H. Wada, and Y. Yamada: *J. Phys.–Conf. Ser.* **807** (2017) 062002.
- [56] S. Kim, K. Kim, and B. I. Min: *Sci. Rep.* **5** (2015) 15052.
- [57] L. Wang, Z. Wang, H.-L. Shi, Z. Chen, F.-K. Chiang, H.-F. Tian, H.-X. Yang, A.-F. Fang, N.-L. Wang, and J.-Q. Li: *Chinese Physics B* **23** (2014) 086103.
- [58] E. Nocerino, U. Stuhr, I. San Lorenzo, F. Mazza, D. Mazzone, J. Hellsvik, S. Hasegawa, S. Asai, T. Masuda, S. Itoh, A. Minelli, Z. Hossain, A. Thamizhavel, K. Lefmann, Y. Sassa, and M. Månsson: *J. Sci.: Adv. Mater. Devices* **8** (2023) 100621.
- [59] Y. Nagano, N. Araoka, A. Mitsuda, H. Yayama, H. Wada, M. Ichihara, M. Isobe, and Y. Ueda: *J. Phys. Soc. Jpn.* **82** (2013) 064715.
- [60] A. V. A. E. D.-N. M. Falkowski, P. Doležal and L. Havela: *Phys. Rev. B* **100** (2019) 064103.
- [61] M. Falkowski, P. Doležal, E. Duverger-Nédellec, L.-M. Chamoreau, J. Forté, A. V. Andreev, and L. Havela: *Phys. Rev. B* **101** (2020) 174110.
- [62] V. K. Anand, Z. Hossain, and C. Geibel: *J. of Phys.: Condens. Matter* **19** (2007) 486207.
- [63] M. Kumar, V. K. Anand, C. Geibel, M. Nicklas, and Z. Hossain: *Phys. Rev. B* **81** (2010) 125107.
- [64] K. Kudo, Y. Nishikubo, and M. Nohara: *J. Phys. Soc. Jpn.* **79** (2010) 123710.
- [65] A. Imre, A. Hellmann, and A. Mewis: *Z. Anorg. Allg. Chem* **633** (2007) 2037.
- [66] S. Maeda, K. Matano, R. Yatagai, T. Oguchi, and G.-q. Zheng: *Phys. Rev. B* **91** (2015) 174516.
- [67] A. Verniere, P. Lejay, J. Boucherle, J. Muller, S. Raymond, J. Flouquet, and A. Sulpice: *Physica B: Cond. Matter* **206** (1995) 509.
- [68] M. Szlawska, M. Majewicz, D. A. Kowalska, and D. Kaczorowski: *Scientific Reports* **13** (2023) 14772.

- [69] A. Verniere, S. Raymond, J. Boucherle, P. Lejay, B. Fåk, J. Flouquet, and J. Mignot: *J. Magn. Magn. Mater.* **153** (1996) 55.
- [70] 松村武: <http://home.hiroshima-u.ac.jp/tmatsu/Matsumura/Research.html> .
- [71] E. Beaurepaire, H. Bulou, F. Scheurer, and J.-P. Kappler: *Magnetism and synchrotron radiation. New trends* (2010).
- [72] A. C. Thompson, D. Vaughan, et al.: *X-ray data booklet* (Lawrence Berkeley National Laboratory, University of California Berkeley, CA, 2001), Vol. 8.
- [73] T. Nagao and J. Igarashi: *Phys. Rev. B* **72** (2005) 174421.
- [74] V. F. Sears: *Neutron news* **3** (1992) 26.
- [75] H. Nakao, Y. Yamasaki, J. Okamoto, T. Sudayama, Y. Takahashi, K. Kobayashi, R. Kumai, and Y. Murakami: *J. Phys.–Conf. Ser.* **502** (2014) 012015.
- [76] G. L. Squires: *Introduction to the Theory of Thermal Neutron Scattering* (Cambridge University Press, 2012) 3 ed.
- [77] J. P. Desclaux and A. J. Freeman: *J. Magn. Magn. Mater.* **8** (1978) 119.
- [78] W. S. Lee, A. P. Sorini, M. Yi, Y. D. Chuang, B. Moritz, W. L. Yang, J.-H. Chu, H. H. Kuo, A. G. C. Gonzalez, I. R. Fisher, Z. Hussain, T. P. Devereaux, and Z. X. Shen: *Phys. Rev. B* **85** (2012) 155142.
- [79] S. Chillal, E. Schierle, E. Weschke, F. Yokaichiya, J.-U. Hoffmann, O. S. Volkova, A. N. Vasiliev, A. A. Sinchenko, P. Lejay, A. Hadj-Azzem, P. Monceau, and B. Lake: *Phys. Rev. B* **102** (2020) 241110(R).
- [80] K. Takubo, R. Comin, D. Ootsuki, T. Mizokawa, H. Wadati, Y. Takahashi, G. Shibata, A. Fujimori, R. Sutarto, F. He, S. Pyon, K. Kudo, M. Nohara, G. Levy, I. S. Elfimov, G. A. Sawatzky, and A. Damascelli: *Phys. Rev. B* **90** (2014) 081104.
- [81] N. Hanasaki, S. Shimomura, K. Mikami, Y. Nogami, H. Nakao, and H. Onodera: *Phys. Rev. B* **95** (2017) 085103.
- [82] Y. Yasui, C. J. Butler, N. D. Khanh, S. Hayami, T. Nomoto, T. Hanaguri, Y. Motome, R. Arita, T.-h. Arima, Y. Tokura, and S. Seki: *Nat. commun.* **11** (2020) 5925.
- [83] S. Hayami and Y. Motome: *Phys. Rev. B* **104** (2021) 144404.
- [84] K. Kaneko, T. Kawasaki, A. Nakamura, K. Munakata, A. Nakao, T. Hanashima, R. Kiyonagi, T. Ohhara, M. Hedo, T. Nakama, and Y. Ōnuki: *J. Phys. Soc. Jpn.* **90** (2021) 064704.
- [85] K. Domieracki and D. Kaczorowski: *Acta Physica Polonica A* **130** (2016) 593.

- [86] 鈴木悠介: Master's Thesis, 北海道大学理学院物性物理学専攻 (2019).
- [87] F. Honda, J. Valenta, J. Prokleška, J. Pospíšil, P. Proschek, J. Prchal, and V. Sechovský: *Phys. Rev. B* **100** (2019) 014401.
- [88] 今布咲子: Master's Thesis, 北海道大学理学院物性物理学専攻 (2021).
- [89] P. A. Slotte: *Journal of Physics C: Solid State Physics* **16** (1983) 2935.
- [90] I. Jäger: *Phys. stat. sol. (b)* **162** (1990) 575.
- [91] K. Schotte and U. Schotte: *Physics Letters A* **55** (1975) 38.
- [92] C. Bredl, F. Steglich, and K. Schotte: *Zeitschrift für Physik B Condensed Matter* **29** (1978) 327.
- [93] V. Rajan, J. Lowenstein, and N. Andrei: *Phys. Rev. Lett.* **49** (1982) 497.